CLASSICAL AND QUANTUM MAGNETIZATION REVERSAL STUDIED IN NANOMETER-SIZED PARTICLES AND CLUSTERS

WOLFGANG WERNSDORFER

Laboratoire Louis Néel, Grenoble, France

CONTENTS

Advances in Chemical Physics, Volume 118, Edited by I. Prigogine and Stuart A. Rice.
ISBN 0-471-43816-2

I. INTRODUCTION

Since the late 1940s, nanometer-sized magnetic particles have generated continuous interest because the study of their properties has proved to be scientifically and technologically very challenging. In particular, it was recognized that the ferromagnetic state, with a given orientation of the particle moment, has a remanent magnetization if the particle is small enough. This was the starting point of huge permanent magnets and magnetic recording industries. However, despite intense activity during the last few decades, the difficulties in making nanoparticles of good enough quality has slowed the advancement of this field. As a consequence, for 50 years, these applications concentrated above and then near the micrometer scale. In the last decade, this has no longer been the case because of the emergence of new fabrication techniques that have led to the possibility of making small objects with the required structural and chemical qualities. In order to study these objects, new techniques were developed such as magnetic force microscopy, magnetometry based on micro-Hall probes, or micro-SQUIDs. This led to a new understanding of the magnetic behavior of nanoparticles, which is now very important for the development of new fundamental theories of magnetism and in modeling new magnetic materials for permanent magnets or high density recording.

In order to put this review into perspective, let us consider Fig. 1, which presents a scale of size ranging from macroscopic down to nanoscopic sizes. The unit of this scale is the number of magnetic moments in a magnetic system. At macroscopic sizes, a magnetic system is described by magnetic domains (Weiss 1907) [1] that are separated by domain walls. Magnetization reversal occurs via nucleation, propagation and annihilation of domain walls (see the hysteresis loop on the left in Fig. 1 which was measured on an individual elliptic CoZr particle of 1 μm × 0.8 μm and a thickness of 50 nm). Shape and width of domain walls depend on the material of the magnetic system, on its size, shape and surface, and on its temperature [2]. The material dependence of the domain walls has motivated the definition of two length scales: (i) the domain wall width δ defined by $\delta = \sqrt{A/K}$ and (ii) the exchange length λ defined by $\lambda = \sqrt{A}/M_S$ where A is the exchange energy, K is the crystalline anisotropy constant, and M_S is the spontaneous magnetization. Qualitatively, the first definition shows that anisotropy energy favors a thin wall, while the exchange energy favors a thick wall. For very small crystalline anisotropy, the first definition suggests an infinite domain wall width which has a large total energy. This is due to the magnetostatic energy term that can be reduced by subdividing the ferromagnetic crystal into domains. Therefore, for very small crystalline anisotropy, the domain wall width is of the order of magnitude of the exchange length λ. Both length scales can range from submicrometer scales in alloys to atomic scales in rare earth systems. When the system size is of the order of magnitude of δ or λ, the formation of domain walls requires too much energy. Therefore, the magnetization remains in the so-called single-domain state.* Hence, the magnetization might reverse by uniform rotation, curling, or other nonuniform modes (see hysteresis loop in the middle of Fig. 1). In this review we discuss mainly this size range where the physics is rather simple (Sections II and III).

For system sizes well below δ and λ, one must take into account explicitly the magnetic moments (spins) and their couplings. The theoretical description is complicated by the particle's boundaries [3–5].

At the smallest size (below which one must consider individual atoms and spins) there are either free clusters made of several atoms [6, 7] or molecular clusters which are macromolecules with a central complex containing magnetic atoms. In the last case, measurements on the Mn_{12} acetate and Fe_8 molecular clusters showed that the physics can be described by a collective moment of spin $S = 10$ (Section V.A). By means of simple hysteresis loop measurements, the quantum character of these molecules showed up in well-defined steps which are due to resonance quantum tunneling between energy levels (see hysteresis loop on the right in Fig. 1).

*In the theory of micromagnetism the single-domain state describes the state where the magnetization is perfectly aligned [2], whereas experimentalists mean often a state without domain wall.

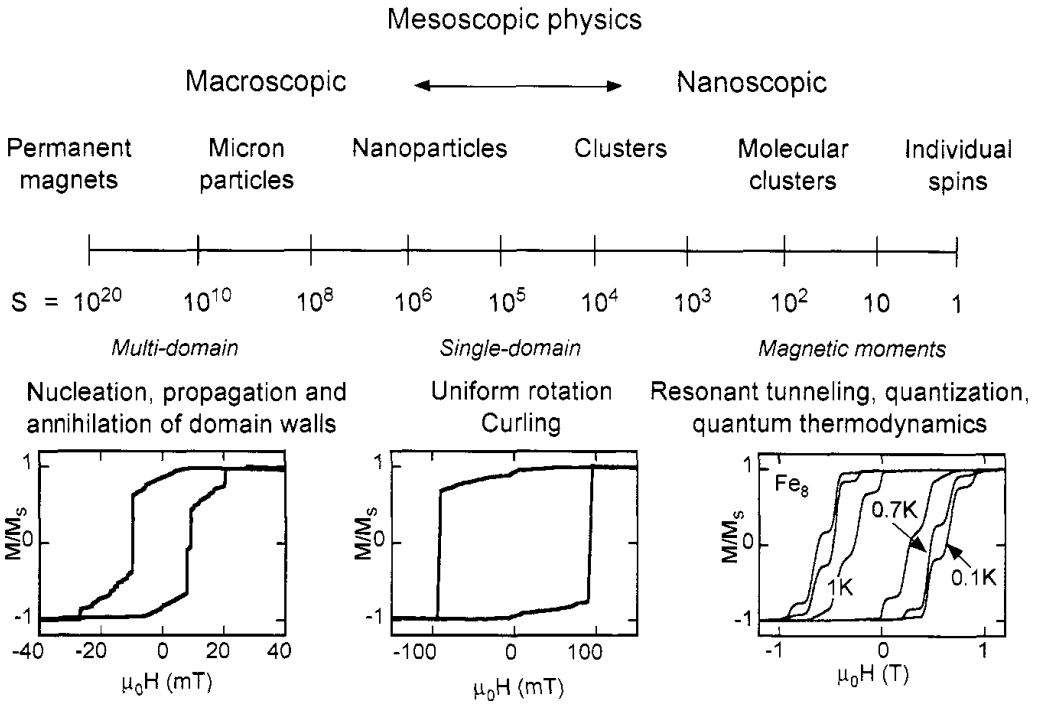

Figure 1. Scale of size that goes from macroscopic down to nanoscopic sizes. The unit of this scale is the number of magnetic moments in a magnetic system (roughly corresponding to the number of atoms). The hysteresis loops are typical examples of magnetization reversal via nucleation, propagation, and annihilation of domain walls (*left*), via uniform rotation (*middle*), and via quantum tunneling (*right*).

In the following sections, we review the most important theories and experimental results concerning the magnetization reversal of single-domain particles and clusters. Special emphasis is laid on single-particle measurements avoiding complications due to distributions of particle size, shape, and so on. Measurements on particle assemblies has been reviewed in Ref. 8. We mainly discuss the low-temperature regime in order to avoid spin excitations.

In Section II, we briefly review the commonly used measuring techniques. Among them, electrical transport measurements, Hall probes, and micro-SQUID techniques seem to be the most convenient techniques for low-temperature measurements. Section III discusses the mechanisms of magnetization reversal in single domain particles at zero kelvin. The influence of temperature on the magnetization reversal is reported in Section IV. Finally, Section V shows that for very small systems or very low temperature, magnetization can reverse via tunneling.

II. SINGLE-PARTICLE MEASUREMENT TECHNIQUES

The following sections review commonly used single-particle measuring techniques avoiding complications due to distributions of particle size, shape, and so

on, which are always present in particle assemblies [8]. Special emphasis is laid on the micro-SQUID technique and the developed methods which allowed the most detailed studies at low temperatures.

A. Overview of Single-Particle Measurement Techniques

The dream of measuring the magnetization reversal of an individual magnetic particle goes back to the pioneering work of Néel [9, 10]. The first realization was published by Morrish and Yu in 1956 [11]. These authors employed a quartz-fiber torsion balance to perform magnetic measurements on individual micrometer-sized γ-Fe_2O_3 particles. With their technique, they wanted to avoid the complication of particle assemblies which are due to different orientations of the particle's easy axis of magnetization and particle–particle dipolar interaction. They aimed to show the existence of a single-domain state in a magnetic particle. Later on, other groups tried to study single particles, but the experimental precision did not allow a detailed study. A first breakthrough came via the work of Knowles [12] who developed a simple optical method for measuring the switching field, defined as the minimum applied field required to reverse the magnetization of a particle. However, the work of Knowles failed to provide quantitative information on well defined particles. More recently, insights into the magnetic properties of individual and isolated particles were obtained with the help of electron holography [13], vibrating reed magnetometry [14], Lorentz microscopy [15, 16], magneto-optical Kerr effect [17], and magnetic force microscopy [18, 19]. Recently, magnetic nanostructures have been studied by the technique of magnetic linear dichroism in the angular distribution of photoelectrons or by photoemission electron microscopy [20, 21]. In addition to magnetic domain observations, element-specific information is available via the characteristic absorption levels or threshold photoemission.* Among all mentioned techniques, most of the studies have been carried out using magnetic force microscopy at room temperature. This technique has an excellent spatial resolution, but time-dependent measurements are difficult due to the sample–tip interaction.

Only a few groups were able to study the magnetization reversal of individual nanoparticles or nanowires at low temperatures. The first magnetization measurements of individual single-domain nanoparticles and nanowires at very low temperatures were presented by Wernsdorfer et al. [22]. The detector (an Nb micro-bridge-DC-SQUID) and the studied particles were fabricated using electron-beam lithography. Coppinger et al. [23] investigated the magnetic properties of nanoparticles by resistance measurements. They observed the two-level fluctuations in the conductance of a sample containing self-organizing ErAs

*We refer to the literature concerning other domain observation techniques [1].

quantum wires and dots in a semi-insulating GaAs matrix. By measuring the electrical resistance of isolated Ni wires with diameters between 20 and 40 nm, Giordano and Hong studied the motion of magnetic domain walls [24, 25]. Other low-temperature techniques that may be adapted to single-particle measurements are Hall probe magnetometry [26–28], magnetometry based on magnetoresistance [29–31], or spin-dependent tunneling with Coulomb blockade [32, 33]. At the time of writing, the micro-SQUID technique allows the most detailed study of the magnetization reversal of nanometer-sized particles [34–39]. The following section reviews the basic ideas of the micro-SQUID technique.

B. Micro-SQUID Magnetometry

The superconducting quantum interference device (SQUID) has been used very successfully for magnetometry and voltage or current measurements in the fields of medicine, metrology, and science [40, 41]. SQUIDs are mostly fabricated from an Nb–AlO_x–Nb trilayer, several hundreds of nanometers thick. The two Josephson junctions are planar tunnel junctions with an area of at least 0.5 μm^2. In order to avoid flux pinning in the superconducting film the SQUID is placed in a magnetically shielded environment. The sample's flux is transferred via a superconducting pickup coil to the input coil of the SQUID. Such a device is widely used because the signal can be measured by simple lock-in techniques. However, this kind of SQUID is not well-suited for measuring the magnetization of single submicron-sized samples because the separation of SQUID and pickup coil leads to a relatively small coupling factor. A much better coupling factor can be achieved by coupling the sample directly with the SQUID loop. In this arrangement, the main difficulty arises from the fact that the magnetic field applied to the sample is also applied to the SQUID. The lack of sensitivity to a high field applied in the SQUID plane led us to the development of the microbridge-DC-SQUID technique [22] which allows us to apply several Tesla in the plane of the SQUID without dramatically reducing the SQUID's sensitivity.

1. Choice of SQUID Configuration

The main criteria for the choice of the micro-SQUID configuration were an easy coupling to a mesoscopic sample, a simple fabrication, a simple mode of operation, robustness and stability, the desired temperature range, and operation in high magnetic fields (in particular for fields applied in the SQUID plane). These criteria led to the use of microbridge junctions instead of the commonly used tunnel junctions.

The Josephson effect in microbridge junctions has first been suggested in 1964 by Anderson and Dayem [42]. These superconducting weak links seemed to be very promising in order to design planar DC-SQUIDs with a one-step thin-film technology. However, Dayem bridges exhibit a Josephson current-phase

relation only when their dimensions are small compared to the coherence length ξ. Such dimensions were difficult to reach at those days. Nowadays, electron beam lithography allows one to directly fabricate reliable microbridge Josephson junctions made of materials like Al, Nb, and Pb.

2. *Fabrication of Micro-SQUIDs*

By using electron beam lithography, planar Al or Nb microbridge-DC-SQUIDs (of 0.5 to 4 μm in diameter) can be constructed (Fig. 2) [43–45]. Al SQUIDs can be obtained by evaporating a 20- to 50-nm thin film onto a PMMA mask, followed by standard lift-off techniques. The fabrication of Nb SQUIDs revealed to be more difficult. The direct evaporation of Nb onto a PMMA mask led to Nb SQUIDs of poor quality which manifested themselves in a very low critical temperature of the superconductivity. Better Nb qualities were achieved by using UHV facilities and substrate temperatures of about 800 K, or higher, in order to grow 20-nm thin Nb films on Si substrates.* The Nb films were covered by 5 nm of Si. The Nb SQUIDs were then patterned with reactive ion etching (RIE) using an AlO mask made by an electron beam lithography via a standard PMMA technique.

An alternative method to fabricate microbridge-DC-SQUIDs has recently been proposed by Bouchiat et al. [46]. The new method is based on local anodization of 3- to 6.5-nm-thick Nb strip lines under the voltage-biased tip of an atomic force microscope (AFM). Microbridge junctions and SQUID loops were obtained by either partial or total oxidation of the Nb layer. The first fabricated devices had about the same performance as micro-SQUIDs fabricated by electron beam lithography. The AFM-made SQUIDs should offer new features such as the fabrication at a chosen position allowing an optimized coupling to magnetic signals. In addition, we expect an increased intrinsic sensitivity: In the case of small magnetic clusters which are placed very close to the microbridge junctions, an improvement of the sensitivity of one to two orders of magnitude might be achieved due to the reduction of the microbridge size. It might allow us to detect the spin flips of about 100 magnetic moments.

3. *Magnetization Measurements Via Critical Current Measurements*

The microbridge-DC-SQUID have a hysteretic $V-I$ curve (Fig. 3): Ramping the current up from zero, the SQUID transits from the superconducting to the normal state at the critical current I_c. Due to Joule heating in the normal state, the SQUID stays resistive down to currents much smaller than I_c. This hysteretic

*In order to have a SQUID that can be exposed to a high field applied in the SQUID plane, the SQUID was made out of a very thin layer preventing flux trapping. In most cases, we used 20-nm-thick Nb layers allowing measurements of hysteresis loops in magnetic fields of up to 2 T. Such SQUIDs might work at fields higher than 10 T when using very thin (<10 nm) Nb layers of high quality.

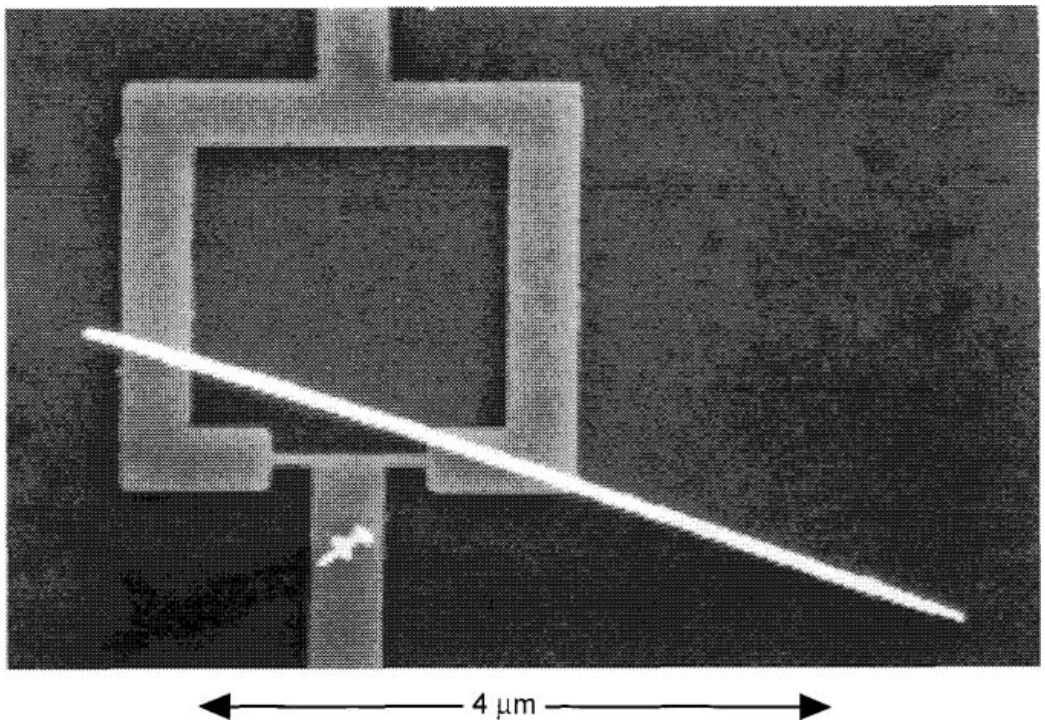

Figure 2. Scanning electron micrograph of an Nb microbridge-DC-SQUID fabricated by electron beam lithography. An Ni wire of diameter of about 90 nm was deposited on the SQUID (Section III.B.2).

$V-I$ curve made it impossible to use standard SQUID electronics or lock-in amplifier to read out the SQUID. Therefore, Benoit et al. developed a method consisting in measuring the critical current of the micro-SQUID [43, 44]. A computer-controlled circuit triggers simultaneously a current ramp (Fig. 4) and a 100-MHz quartz clock. As soon as a dV/dt pulse is detected at the SQUID due to the transition from the superconducting to the normal state,* the clock stops and the current is set to zero. The clock reading is transferred to the computer, and the cycle begins again. The critical current is proportional to the duration of the current ramp. The repetition rate is about 10 kHz, limited by the time needed to settle the current. Because the critical current I_c is a periodic function of the flux going through the SQUID loop (Fig. 5), one can easily deduce the flux change in the SQUID loop by measuring the critical current. The sensitivity achieved by the critical current measurement technique was about $10^{-5}\Phi_0/\sqrt{\text{Hz}}$ for Al SQUIDs and $10^{-4}\Phi_0/\sqrt{\text{Hz}}$ for Nb SQUIDs ($\Phi_0 = h/2e = 2 \times 10^{-15}$ Wb).

*It is important to mention that the dV/dt pulse can be detected directly on the current biasing lead of the SQUID; that is, for most cases it is sufficient to connect the SQUID with a single wire and the mass of the cryostat.

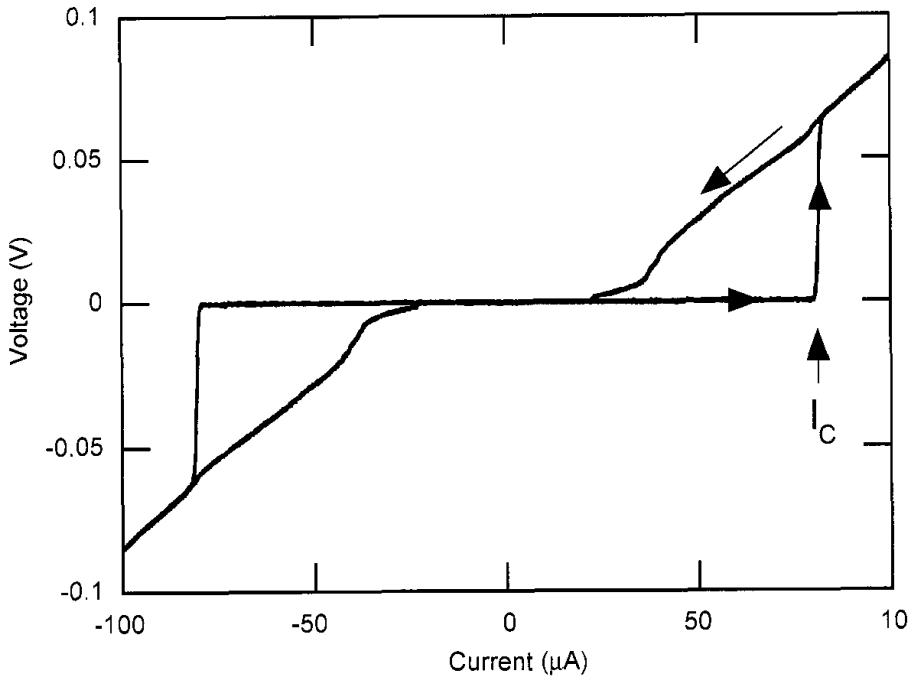

Figure 3. Oscilloscope reading of a voltage versus current curve of an Nb microbridge-DC-SQUID. The SQUID transits from the superconducting to the normal state at the critical current I_c.

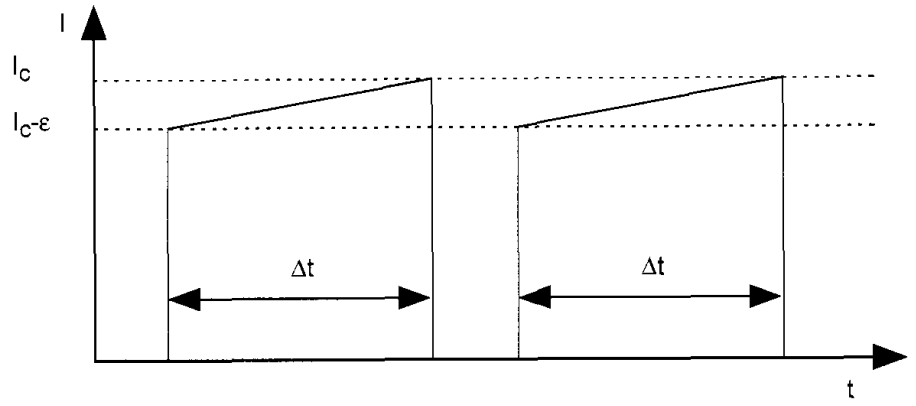

Figure 4. Current injected into a SQUID loop. First, the current is increased quickly up to a current $I_c-\varepsilon$ which is close to the critical current I_c. Then, the current is ramped up to I_c. As soon as a dV/dt pulse is detected at the SQUID due to the transition from the superconducting to the normal state, the current is set to zero. I_c is proportional to the duration of the current ramp Δt. The repetition rate of the cycle is up to 10 kHz.

In order to have good magnetic flux coupling, the mesoscopic systems, for instance the magnetic particles, is directly placed on the SQUID loop (Fig. 6) [45]. The SQUID detects the flux through its loop produced by the sample's

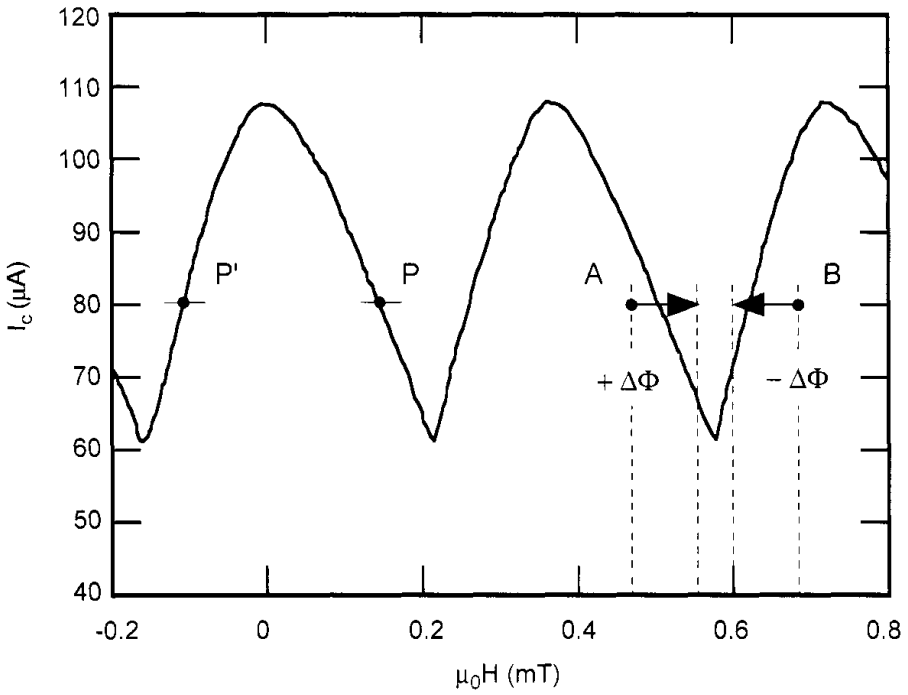

Figure 5. Critical current I_c of an Al micro-SQUID as a function of a magnetic field applied perpendicular to the SQUID plane. For the feedback mode an external field perpendicular to the SQUID loop is applied which keeps the critical current constant at a working point—for example, point **P** or **P′**. For the cold mode method the SQUID is biased close to the critical current so that it is in state **A** or **B**, respectively, for positive or negative flux jumps induced by the magnetization reversal.

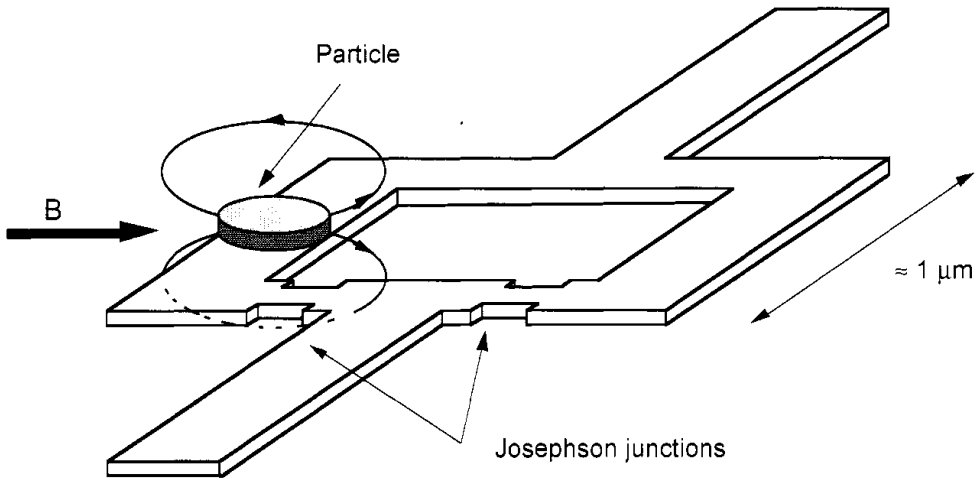

Figure 6. Schematic drawing of a planar microbridge-DC-SQUID on which a ferromagnetic particle is placed. The SQUID detects the flux through its loop produced by the sample magnetization. Due to the close proximity between sample and SQUID, a very efficient and direct flux coupling is achieved.

magnetization. For hysteresis loop measurements, the external field is applied in the plane of the SQUID (Fig. 6); thus the SQUID is only sensitive to the flux induced by the stray field of the sample's magnetization. The flux sensitivity of the critical current mode allowed us to detect the magnetization reversals corresponding to $10^4\mu_B/\sqrt{\text{Hz}}$ ($10^{-16}\text{emu}/\sqrt{\text{Hz}}$)—that is, the magnetic moment of a Co nanoparticle with a diameter of 5 nm. The time resolution was given by the time between two measurements of the critical current. In this case, the achieved time resolution was 100 μs.

4. *Feedback Mode for Hysteresis Loop Measurements*

For the detection of flux variations larger than $\Phi_0/2$, the direct critical current method (Section II.B.3) is complicated by the fact that I_c is a nonmonotonous function of the flux (Fig. 5) which goes through the SQUID loop. In this cases, we used a feedback mode consisting in applying an external field perpendicular to the SQUID loop which compensates the stray field variations keeping the critical current constant at a working point as shown in Fig. 5. After each I_c measurement, the computer calculates the difference between a working point and I_c, multiplies it with a feedback factor, and adds it to the feedback (or compensation) field. The feedback field gives then the stray field variation of the sample's magnetization. It can easily be given in units of Φ_0. Knowing the coupling factor between particle and SQUID loop, absolute magnetic moment measurements are possible.

The time resolution of the feedback mode depends on the rate of the I_c measurements. For rates of about 10 kHz, we are able to follow flux variations in the millisecond range.

5. *Cold Mode Method for Magnetization Switching Measurements*

For studying the magnetization switching of nanoparticles, we developed a special mode, called the *cold mode method* [36–39], which are much faster and more sensitive than the previously presented modes. The achieved flux sensitivity allowed us to detect the magnetization switching corresponding to $10^3\,\mu_B$ (10^{-17} emu)—that is, the switching of a Co nanoparticle with a diameter of 2 to 3 nm. The time resolution of the switching detection reached the nanosecond range.

The cold mode method is also specially adapted for studying the temperature dependence of the magnetization reversal and macroscopic quantum tunneling of magnetization. Indeed, the main difficulty associated with the SQUID detection technique lies in the Joule heating when the critical current is reached. After the normal state transition at the critical current, the SQUID dissipates for about 100 ns which slightly heats the magnetic particle coupled to the SQUID. This problem can be solved by the cold mode method which uses the SQUID only as a trigger [36–39].

The cold mode consists in biasing the SQUID close to the critical current while a field is applied perpendicular to the SQUID plane so that the SQUID is in state **A** (**B**) for a positive (negative) flux jump (Fig. 5) that can be induced by the magnetization reversal of a particle coupled to the SQUID loop. The magnetization reversal then triggers a transition of the SQUID from the superconducting to the normal state; that is, a dV/dt pulse can be detected on the current lead biasing the SQUID. Our SQUID electronics allows us to detect the dV/dt pulse some nanoseconds after the magnetization reversal, allowing very precise switching field measurements. Because this method only heats the sample after the magnetization reversal, we called it the *cold mode method.*

Another advantage of this mode is that the sample does not interfere with the rf-noise which is induced in oxide layer Josephson junctions of conventional SQUIDs because the hysteretic micro-SQUID is in the superconducting state before the magnetization reversal.

Finally, the cold mode method is very important for studying macroscopic quantum tunneling of magnetization. Quantum theory predicts that the escape rate from a metastable potential well by quantum tunneling is strongly reduced by the coupling of the magnetic system with its environment. Therefore, the measuring device must be weakly coupled to the magnetic particle. However, in order to measure the magnetization reversal, the SQUID must be strongly coupled to the magnetic particle that hinders the possibility of quantum tunneling. This problem can be solved by using the cold mode method. In order to show this schematically, Fig. 7 represents two energy potentials: One is the double well potential of the particle, and the other is the periodic potential of the SQUID. Before the magnetization reversal, both systems are in a metastable state: the particle because of an applied field which is close to the switching field and the SQUID because of a current through the SQUID loop which is close to the critical current. When the particle overcomes the saddle point or tunnels through the energy barrier, its magnetization rotates by only few degrees. For this starting process of the magnetization reversal, the coupling between particle and SQUID can be arranged to be very small.* Afterwards, the particle falls into

*In order to illustrate the dipolar couplings, let us consider the energy scales involved. For most of the particles measured so far below 1 K, the energy barrier height from the metastable state up to the saddle point is of the order of a few Kelvins whereas that from the lower state up to the saddle point is between 10^3 and 10^6 K. These energy scales should be compared with the energy necessary to drive the SQUID out of its metastable superconducting state which is of the order of a few Kelvin. Therefore, only a small energy transfer is necessary to measure the magnetization reversal. In addition, a proper orientation of the easy axis of magnetization with respect to the SQUID loop can further reduce the coupling during the first stage of the magnetization reversal. In the case of an easy axis of magnetization perpendicular to the current direction in the SQUID wire (Fig. 6), the coupling factor between SQUID loop and particle is proportional to $(1-\cos\varphi)$, where φ is the angle between the direction of magnetization and its easy axis. Therefore, the coupling is very weak at the first stage of magnetization reversal where φ is small.

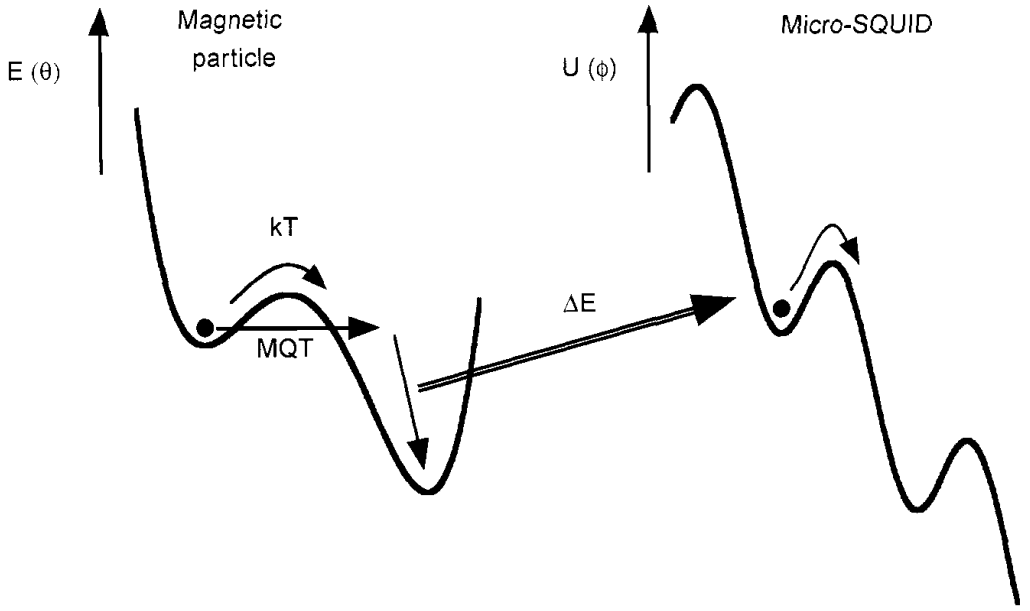

Figure 7. Energy scheme of the cold mode method. After the particle overcomes the saddle point or tunnels through the energy barrier, it falls into the lower potential well releasing energy. A very small fraction ΔE of this energy is transferred to the SQUID and drives the SQUID out of its metastable superconducting state.

the lower well which implies a rotation of magnetization of up to 180°. During this process, the coupling between particle and SQUID should be strong enough to drive the SQUID out of its metastable state. The corresponding transition from the superconducting into the normal state is easily measurable for a hysteretic SQUID. The main disadvantage of the cold mode is that only the switching field of magnetization reversal can be measured and not the magnetization before and during the magnetization reversal.

6. *Blind Mode Method for Three-Dimensional Switching Field Measurements*

A disadvantage of the micro-SQUID technique is that it does not function properly when a significant field is applied perpendicular to the SQUID loop. It works also only below the superconducting critical temperature of Nb ($T_c \approx 7$ K for our SQUIDs). These facts limited us to 2D measurements and to $T<T_c$ in the first experiments [35–37]. However, we showed recently that full-three-dimensional measurements can be done by using an indirect method [38]. In addition, this technique allows us to study the magnetization reversal for $T>T_c$.

Let us consider Fig. 8 showing switching field measurements (Section III) for in-the-SQUID-plane applied fields, detected using the *cold mode* (Section II.B.5). The three-dimensional switching field measurements and the studies

as a function of temperature can be done using a three-step method which we call the *blind mode* (Fig. 8):

1. **Saturation.** The magnetization of the particles is saturated in a given direction (at $T = 35$ mK).
2. **Testing.** A test field is applied at a temperature between 35 mK and 30 K* which may or may not cause a magnetization switching.
3. **Probing.** After cooling to $T = 35$ mK, the SQUID is switched on and a field is swept in the plane of the SQUID to probe the resulting magnetization state using direct critical current measurements, the feedback mode, or the cold mode.

If the SQUID detects a magnetization jump in step 3, this means that the previously applied test field was weaker than the switching field for the direction being probed in step 2. The next interaction will then be done with a stronger test

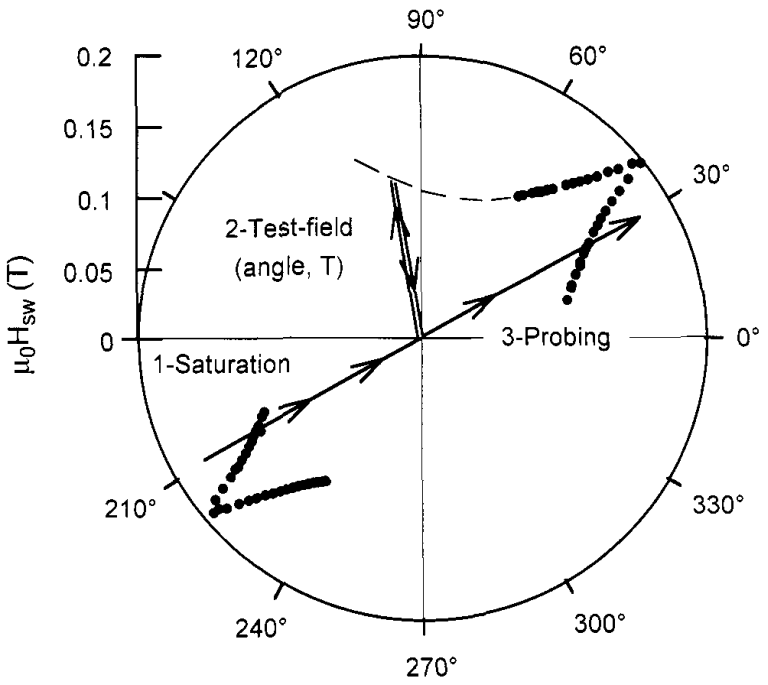

Figure 8. Schematics for the *blind mode* method presenting the angular dependence of the switching field near the easy axis of a 3-nm Co cluster (full circles) (Section III.A.2). First, the magnetization of the particle is saturated in a given direction (at $T = 35$ mK). Then, a test field is applied, at a temperature between 35 mK and 30 K, which may or may not cause a magnetization switching. Finally, the SQUID is switched on (at $T = 35$ mK) and a field is applied in the plane of the SQUID to probe the resulting magnetization state.

*Our highest temperatures of 30 K was only limited by the cooling time. Below 30 K, we achieved cooling rates of few Kelvins per second.

field. On the other hand, if the SQUID does not detect any magnetization jump in step 3, this means that the reversal occurred during step 2. The next interaction will then be done with a weaker field. When choosing the new test field with the help of a bisection algorithm, we needed about 8 repetitions of the three steps in order to get the switching field with good precision. This method allows us to scan the entire field space.*

7. *Micro-SQUID Arrays*

We also use arrays of micro-SQUIDs as a magnetometer for macroscopic samples. There are three applications that were particularly interesting: crystals of magnetic molecular clusters [47] (Section V.A), nucleation and depinning of magnetic domain walls in thin films [48], and arrays of magnetic dots [49]. The procedure consists in placing a sample on top of an array of micro-SQUIDs so that some SQUIDs are directly under the sample, some SQUIDs are at the border of the sample, and some SQUIDs are beside the sample (Fig. 9). When a SQUID is very close to the sample, it is sensing locally the magnetization reversal whereas when the SQUID is far away, it integrates over a bigger sample volume. Therefore, depending on the sample, one can obtain more insight in the magnetization reversal than with conventional techniques that measure only the total magnetization.

Our magnetometer works in the temperature range between 0.035 and 6 K and in fields up to 5 T with sweeping rates as high as 30 T/s, along with a field stability better than a microtesla. The time resolution is about 1 ms (Section II.B.4) allowing short-time measurements. The field can be applied in any direction of the micro-SQUID plane with a precision much better than 0.1° by separately driving three orthogonal coils [45].

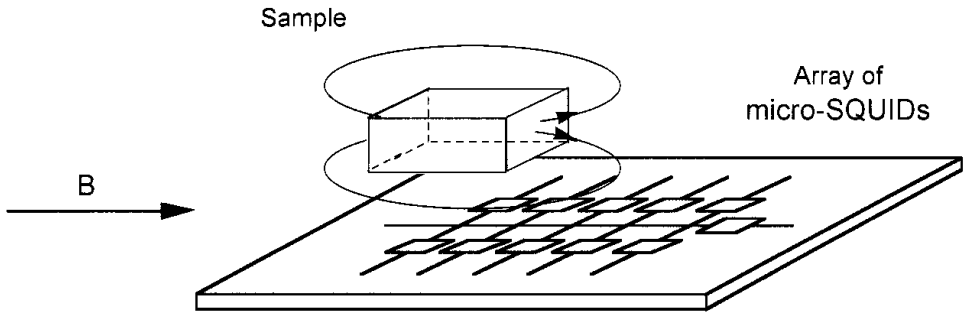

Figure 9. Schematic representation of our magnetometer which is an array of micro-SQUIDs. Its high sensitivity allows us to study single crystals of the order of 10 to 500 μm which are placed directly on the array.

*It is worth mentioning that special precautions are necessary for anisotropies that are more complex than uniaxial (Section III).

8. *Scanning SQUID Microscope*

The micro-SQUID technique has recently been used to build a scanning SQUID microscope [50]. The SQUID is designed by electron beam lithography at the apex of a silicon cantilever. The lever is attached to a force sensor, allowing to image magnetically, as well as topographically with a spatial resolution of 50 nm and a flux resolution of about $10^{-4}\,\phi_0$. The first application of this technique concerned the imaging of vortices in artificial networks.

9. *Outlook*

After the development of micro-SQUID technique in the early 1990s [43, 44], the study of magnetization reversal in magnetic nanostructures began in 1993 [45]. The first studied systems were micrometer-sized particles containing about 10^{10} magnetic moments. During the following years, the micro-SQUID technique has been improved to study smaller and smaller systems. In 2000, clusters containing about 10^3 magnetic moments could be studied. This achievement raises the question whether further improvements might be possible. The fundamental limit of a SQUID is the quantum limit which corresponds to a sensitivity of one magnetic moment for a SQUID with 1 μm^2. One might come close to this limit by using shunted SQUIDs [51]. Another possibility could be a reduction of the section of the microbridges [46]. Finally, the micro-SQUID technique could be improved by using superconducting materials with higher critical temperatures allowing measurements at higher temperatures.

III. MECHANISMS OF MAGNETIZATION REVERSAL AT ZERO KELVIN

As already briefly discussed in the introduction, for a sufficiently small magnetic sample it is energetically unfavorable to form a stable magnetic domain wall. The specimen then behaves as a single magnetic domain. For the smallest single-domain particles,* the magnetization is expected to reverse by uniform rotation of magnetization (Section III.A). For somewhat larger ones, nonuniform reversal modes are more likely—for example, the curling reversal mode (Section III.B.1). For larger particles, magnetization reversal occurs via a domain wall nucleation process starting in a rather small volume of the particle. For even larger particles, the nucleated domain wall can be stable for certain fields. The magnetization reversal happens then via nucleation and annihilation processes (Section III.B.3). In these sections we neglect temperature and quantum effects.

*In the theory of micromagnetism, the single-domain state describes the state where the magnetization is perfectly aligned [2], whereas experimentalists often mean a state without a domain wall.

The following section discusses in detail the uniform rotation mode that is used in many theories, in particular in Néel, Brown, and Coffey's theory of magnetization reversal by thermal activation (Section IV) and in the theory of macroscopic quantum tunneling of magnetization (Section V).

A. Magnetization Reversal by Uniform Rotation (Stoner–Wohlfarth Model)

The model of uniform rotation of magnetization, developed by Stoner and Wohlfarth [52], and Néel [53], is the simplest classical model describing magnetization reversal. One considers a particle of an ideal magnetic material where exchange energy holds all spins tightly parallel to each other, and the magnetization magnitude does not depend on space. In this case the exchange energy is constant, and it plays no role in the energy minimization. Consequently, there is competition only between the anisotropy energy of the particle and the effect of the applied field. The original study by Stoner and Wohlfarth assumed only uniaxial shape anisotropy, which is the anisotropy of the magnetostatic energy of the sample induced by its nonspherical shape. Thiaville has generalized this model for an arbitrary effective anisotropy which includes any magnetocrystalline anisotropy and even surface anisotropy [54]. In the simplest case of uniaxial anisotropy, the energy of a Stoner–Wohlfarth particle is given by

$$E = KV \sin^2\phi - \mu_0 M_S VH \cos(\theta - \phi) \tag{3.1}$$

where KV is the uniaxial anisotropy energy which depends on the shape of the particle, V is the volume of the particle, M_S is the spontaneous magnetization, H the magnitude of the applied field, and ϕ and θ are the angles of magnetization and applied field, respectively, with respect to the easy axis of magnetization. The potential energy of Eq. (3.1) has two minima separated by an energy barrier. For given values of θ and H, the magnetization lies at an angle ϕ which locally minimizes the energy. This position can by found by equating to zero the first derivative with respect to ϕ of Eq. (3.1): $\partial E/\partial\phi = 0$. The second derivative provides the criteria for maxima and minima. The magnetization reversal is defined by the minimal field value at which the energy barrier between the metastable minimum and the stable one vanishes—that is, at $\partial E/\partial\phi = \partial^2 E/\partial\phi^2 = 0$. A short analysis yields the angular dependence of this field, called the switching field H_{sw}^0 or in dimensionless units:

$$h_{sw}^0 = \frac{H_{sw}^0}{H_a} = \frac{1}{(\sin^{2/3}\theta + \cos^{2/3}\theta)^{3/2}} \tag{3.2}$$

where $H_a = 2K/(\mu_0 M_S)$ is the anisotropy field. The angular dependence of h^0_{sw} is plotted in Fig. 10.

Contrary to h^0_{sw}, the hysteresis loops cannot be expressed analytically and have to be calculated numerically. The result is seen in Fig. 11 showing the component of magnetization projected along the direction of the applied field; that is, $M_H = M_S \cos(\theta - \phi)$. Such loops are often called Stoner–Wohlfarth hysteresis loops.*

The main advantage of this classical theory is that it is sufficiently simple to add some extra features to it, as presented in the following.

1. *Generalization of the Stoner–Wohlfarth Model*

The original model of Stoner and Wohlfarth assumed only uniaxial shape anisotropy with one anisotropy constant [one second-order term, see Eq. (3.1)].

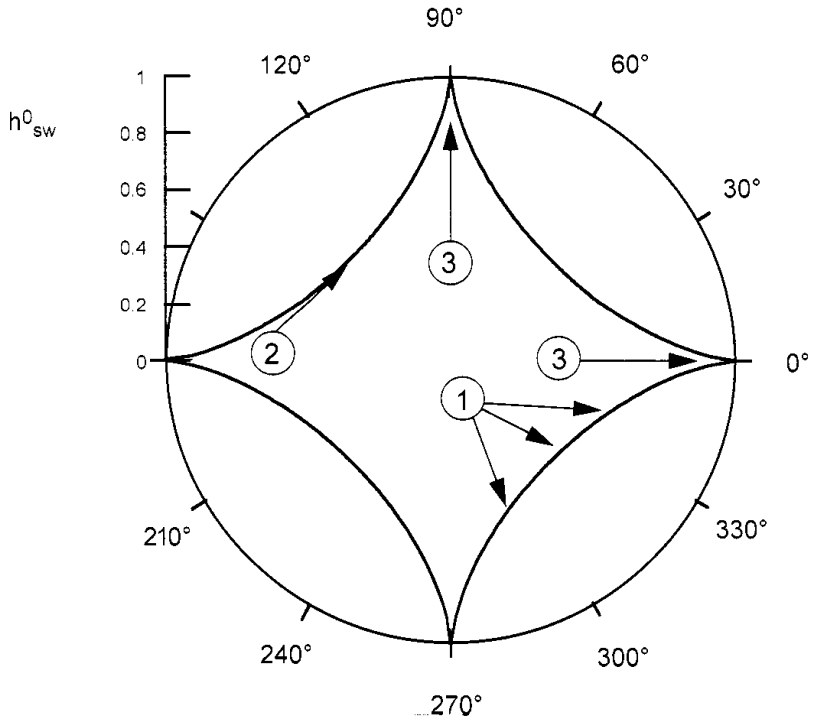

Figure 10. Angular dependence of the Stoner–Wohlfarth switching field $h^0_{sw} = H^0_{sw}/H_a$ [Eq. (3.2)]. This curve is often called the "Stoner–Wohlfarth astroid." Cases 1 to 3 correspond to Eqs. (3.5) to (3.9) concerning the field dependence of the anisotrophy barrier height.

*It is important to note that single-particle measurement techniques do not measure this component M_H. For example, for the micro-SQUID technique, with the easy axis of magnetization in the plane of the SQUID and perpendicular to the current direction in the SQUID wire (Fig. 6), one measures a magnetic flux that is proportional to $M_S \cos \phi$ (Fig. 12).

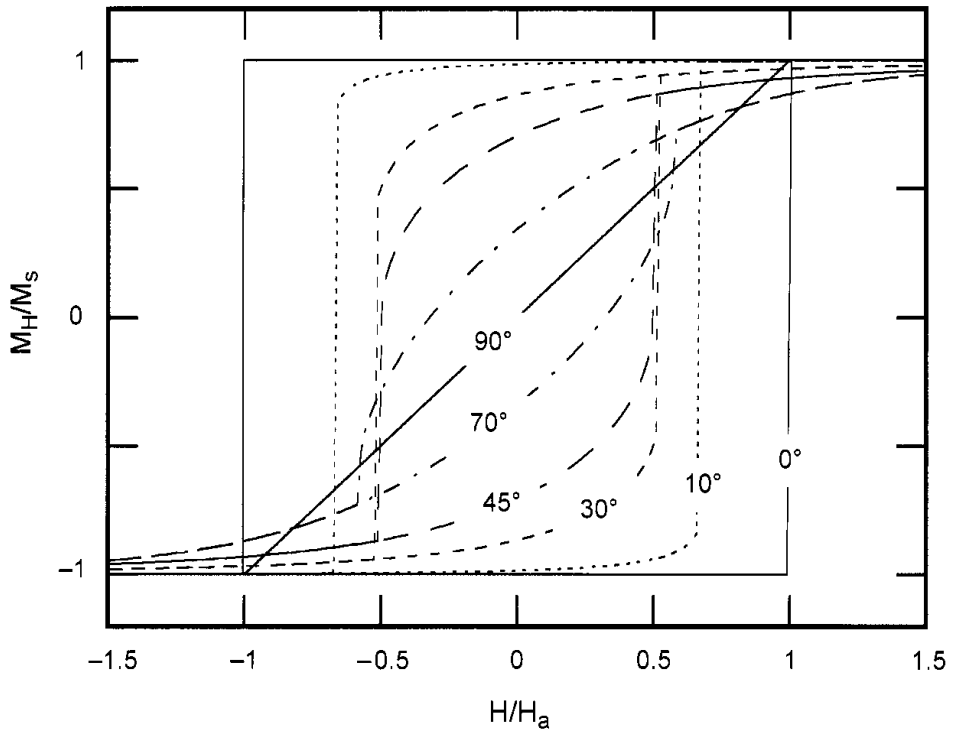

Figure 11. Hysteresis loops of a Stoner–Wohlfarth particle for different field angles θ. The component of magnetization along the direction of the applied field is plotted; that is, $M_H = M_S \cos(\phi - \theta)$.

This is sufficient to describe highly symmetric cases like a prolate spheroid of revolution or an infinite cylinder. However, real systems are often quite complex, and the anisotropy is a sum of mainly shape (magnetostatic), magnetocrystalline, magnetoelastic, and surface anisotropy. One additional complication arises because the different contributions of anisotropies are often aligned in an arbitrary way one with respect to each other. All these facts motivated a generalization of the Stoner–Wohlfarth model for an arbitrary effective anisotropy which was done by Thiaville [54, 55].

Similar to the Stoner–Wohlfarth model, one supposes that the exchange interaction in the cluster couples all the spins strongly together to form a giant spin whose direction is described by the unit vector $\vec{m}$. The only degrees of freedom of the particle's magnetization are the two angles of orientation of $\vec{m}$. The reversal of the magnetization is described by the potential energy:

$$E(\vec{m}, \vec{H}) = E_0(\vec{m}) - \mu_0 V M_s \vec{m}.\vec{H} \tag{3.3}$$

where V and M_s are the magnetic volume and the saturation magnetization of the particle respectively, $\vec{H}$ is the external magnetic field, and $E_0(\vec{m})$ is the magnetic

anisotropy energy which is given by

$$E_0(\vec{m}) = E_{\text{shape}}(\vec{m}) + E_{\text{MC}}(\vec{m}) + E_{\text{surface}}(\vec{m}) + E_{\text{ME}}(\vec{m}) \tag{3.4}$$

E_{shape} is the magnetostatic energy related to the cluster shape. E_{MC} is the magnetocrystalline anisotropy (MC) arising from the coupling of the magnetization with the crystalline lattice, similar as in bulk. E_{surface} is due to the symmetry breaking and surface strains. In addition, if the particle experiences an external stress, the volumic relaxation inside the particle induces a magnetoelastic (ME) anisotropy energy E_{ME}. All these anisotropy energies can be developed in a power series of $m_x^a m_y^b m_z^c$ with $p = a + b + c = 2, 4, 6, \ldots$ giving the order of the anisotropy term. Shape anisotropy can be written as a biaxial anisotropy with two second-order terms. Magnetocrystalline anisotropy is in most cases either uniaxial (hexagonal systems) or cubic, yielding mainly second- and fourth-order terms. Finally, in the simplest case, surface and magnetoelastic anisotropies are of second-order.

Thiaville proposed a geometrical method to calculate the particle's energy and to determine the switching field for all angles of the applied magnetic field yielding the critical surface of switching fields which is analogous to the Stoner–Wohlfarth astroid (Fig. 10).

The main interest of Thiaville's calculation is that measuring the critical surface of the switching field allows one to find the effective anisotropy of the nanoparticle. The knowledge of the latter is important for temperature-dependent studies (Section IV) and quantum tunneling investigations (Section V). Knowing precisely the particle's shape and the crystallographic axis allows one to determine the different contributions to the effective anisotropy.

Thiaville's calculation predicts also the field dependence of the energy barrier height ΔE close to switching ($\varepsilon = (1 - H/H_{\text{sw}}^0) \ll 1$) which is important to know for temperature-dependent studies (Sections IV and V). Three cases have to be distinguished:

1. In the majority of cases except the two following cases (see case 1 in Fig. 10):

$$\Delta E = 4KV \frac{\sqrt{2}}{3} \frac{\cos\gamma}{\sqrt{\rho}} \varepsilon^{3/2} = E_0 \varepsilon^{3/2} \tag{3.5}$$

where KV is the anisotropy energy constant, γ is the angle of incidence between the local normal to the critical surface and the field sweeping direction, and ρ is the radius of curvature of the focal curve [55] at H_{sw}^0. It is important to emphasize that all these variables can be found experimentally by measuring the critical surface of the switching field. For

uniaxial anisotropy (i.e., the 2D Stoner–Wohlfarth case), Eq. (3.5) becomes

$$\Delta E = 4KV\left(\frac{2}{3}\right)^{3/2} \frac{|\cos\theta|^{1/3}}{1+|\cos\theta|^{2/3}} \varepsilon^{3/2} \tag{3.6}$$

where θ is the angle of the applied field with respect to the easy axis of magnetization [Eq. (3.1)].

2. At glancing incidence (see case 2 in Fig. 10) with respect to the critical surface ($\gamma = \pi/2$), the power of ε is different, yielding

$$\Delta E = E_0' \varepsilon^3 \tag{3.7}$$

where E_0' has been calculated only in the two-dimensional case [54].

3. At a cusp point where $\gamma = \pi/2$ (see case 3 in Fig. 10),

$$\Delta E = E_0'' \varepsilon^2 \tag{3.8}$$

where E_0'' has been calculated only in the two-dimensional case [54]. In the case of uniaxial anisotropy i.e., the 2D Stoner–Wohlfarth case), Eq. (3.8) becomes

$$\Delta E = KV\varepsilon^2 = KV\left(1 - \frac{H}{H_a}\right)^2 \tag{3.9}$$

where $H_a = (2K/\mu_0 M_s)$ [Eq. (3.1)]. This equation is only valid for $\theta = 0$ and $\pi/2$, and it is valid for $0 \leq H \leq H_a$. This famous result of Néel [9, 10] has often been wrongly used for assemblies of nanoparticles where it is very difficult to achieve the conditions $\theta = 0$ and $\pi/2$ [56]. Up to now, only the power 3/2 and 2 (cases 1 and 3) has been found by single-particle measurements [36, 37] (see also Figs. 28 and 29).

Another simple analytical approximation for the field dependence of the energy barrier $\Delta E(H)$ was derived numerically by Pfeiffer [57, 58]

$$\Delta E = KV(1 - H/H_{sw}^0)^a = E_0 \varepsilon^a \tag{3.10}$$

where $a = 0.86 + 1.14h_{sw}^0$, and h_{sw}^0 is given by Eq. (3.2). This approximation is good for the intermediate field regime—that is, for fields H not too close to H_a and not too small.

2. *Experimental Evidence for Magnetization Reversal by Uniform Rotation*

In order to demonstrate experimentally the uniform rotation mode, the angular dependence of the magnetization reversal has often been studied (see references in Ref. 2). However, a comparison of theory with experiment is difficult because magnetic particles often have a nonuniform magnetization state that is due to rather complicated shapes and surfaces, crystalline defects, and surface anisotropy. In general, for many particle shapes the demagnetization fields inside the particles are nonuniform leading to nonuniform magnetization states [2]. An example is presented in Fig. 12 which compares typical hysteresis loop measurements of an elliptical Co particle, fabricated by electron beam lithography, with the prediction of the Stoner–Wohlfarth model (Fig. 12). Before magnetization reversal, the magnetization decreases more strongly than predicted because the magnetic configuration is not collinear as in the Stoner–Wohlfarth model, but instead presents deviations mainly near the particle surface. The angular dependence of the switching field agrees with the Stoner–Wohlfarth model only for angles $\theta \geq 30°$ where nonlinearities and defects play a less important role [22, 59].

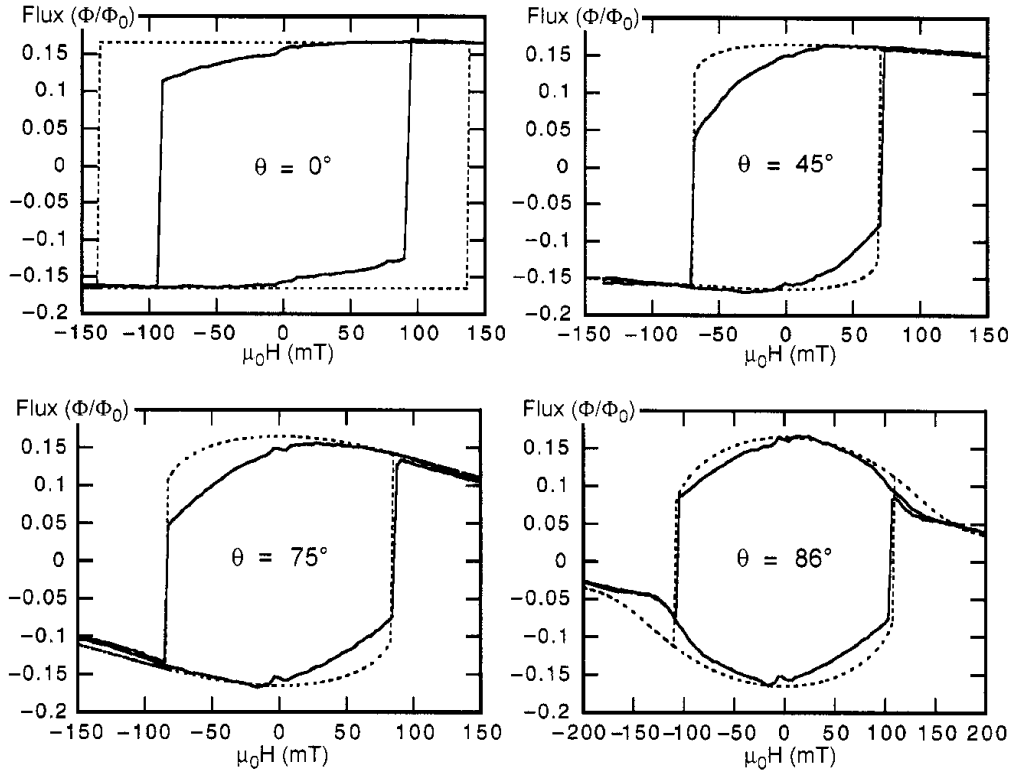

Figure 12. Hysteresis loops of a nanocrystalline elliptic Co particle of $70 \times 50 \times 25\,\text{nm}^3$. The *dashed line* is the prediction of the Stoner–Wohlfarth model of uniform rotation of magnetization. The deviations are due to nonuniform magnetization states.

Studies of magnetization reversal processes in ultrathin magnetic dots with in-plane uniaxial anisotropy showed also switching fields that are very close to the Stoner–Wohlfarth model, although magnetic relaxation experiments clearly showed that nucleation volumes are by far smaller than an individual dot volume [49]. These studies show clearly that switching field measurements as a function of the angles of the applied field cannot be taken unambiguously as a proof of a Stoner–Wohlfarth reversal.

The first clear demonstration of the uniform reversal mode has been found with Co nanoparticles [36], and BaFeO nanoparticles [37], the latter having a dominant uniaxial magnetocrystalline anisotropy. The three-dimensional angular dependence of the switching field measured on BaFeO particles of about 20 nm could be explained with the Stoner–Wohlfarth model taking into account the shape anisotropy and hexagonal crystalline anisotropy of BaFeO [38]. This explication is supported by temperature- and time-dependent measurements yielding activation volumes which are very close to the particle volume (Section IV).

We present here the first measurements on individual cobalt clusters of 3 nm in diameter containing about a thousand atoms (Figs. 13 and 14) [39]. In order to achieve the needed sensitivity, Co clusters preformed in the gas phase are directly embedded in a co-deposited thin Nb film that is subsequently used to pattern micro-SQUIDs. A laser vaporization and inert gas condensation source is used to produce an intense supersonic beam of nanosized Co clusters which can be deposited in various matrices under ultra-high-vacuum (UHV) conditions. Due to the low-energy deposition regime, clusters do not fragment upon impact on the substrate [60]. The niobium matrix is simultaneously deposited from a UHV electron gun evaporator leading to continuous films with a low concentration of embedded Co clusters [61]. These films are used to pattern planar microbridge-DC-SQUIDs by electron beam lithography. The later ones allow us to detect the magnetization reversal of a single Co cluster for an applied magnetic field in any direction and in the temperature range between 0.03 and 30 K (Section II. B). However, the desired sensitivity is only achieved for Co clusters embedded into the microbridges where the magnetic flux coupling is high enough. Due to the low concentration of embedded Co clusters, we have a maximum of 5 noninteracting particles in a microbridge which is 300 nm long and 50 nm wide. We can separately detect the magnetization switching for each cluster. Indeed they are clearly different in intensity and orientation because of the random distribution of the easy magnetization directions. The *cold mode* method (Section II.B.5) in combination with the *blind* method (Section II.B.6) allows us to detect separately the magnetic signal for each cluster.

High-resolution transmission electron microscopy observations showed that the Co clusters are well-crystallized in a *f.c.c.* structure (Fig. 13) with a sharp size distribution [61]. They mainly form truncated octahedrons (Fig. 14) [39].

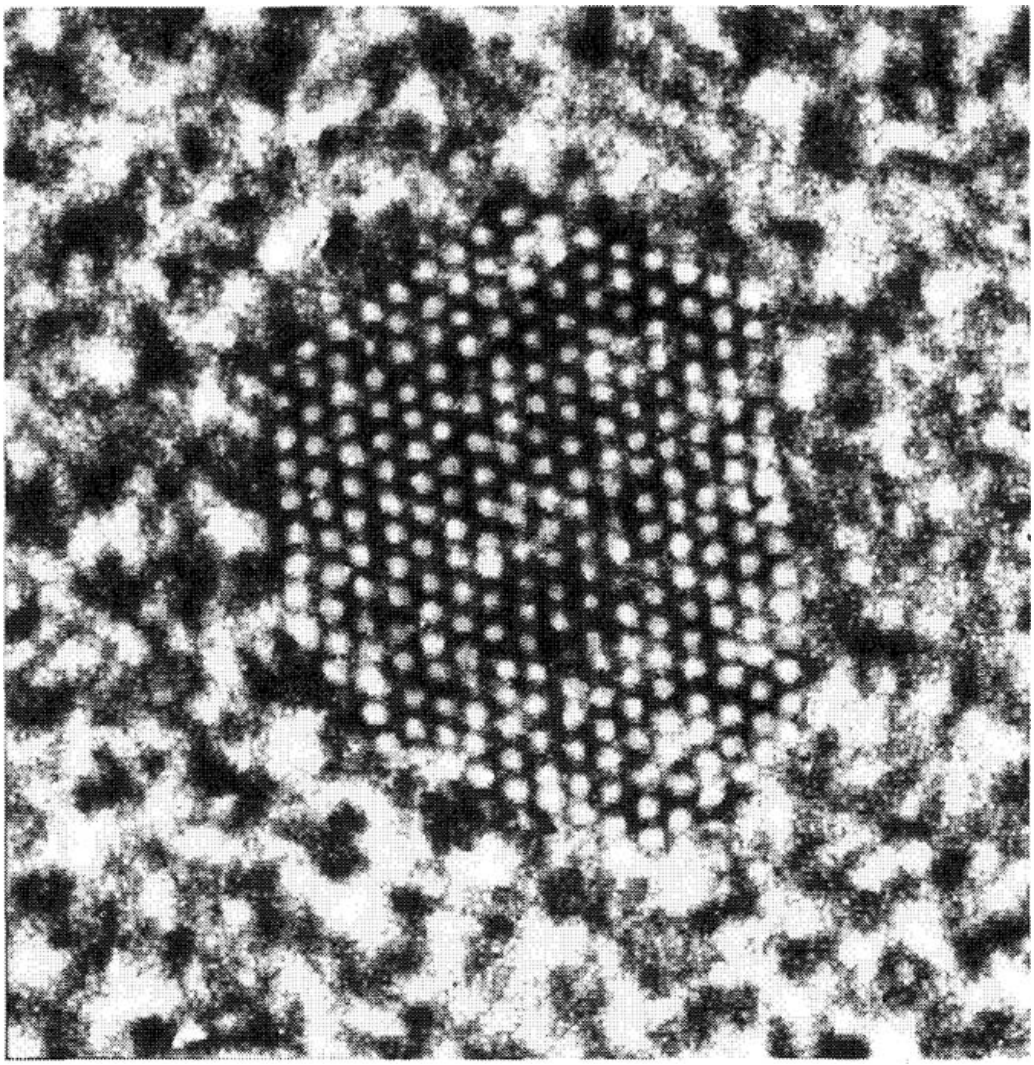

Figure 13. High-resolution transmission electron microscopy observation along a [110] direction of 3-nm cobalt cluster exhibiting an *f.c.c.* structure.

Figure 15 displays a typical measurement of switching fields in three dimensions of a 3-nm Co cluster at $T = 35$ mK. This surface is a three-dimensional picture directly related to the anisotropy involved in the magnetization reversal of the particle (Section III. A). It can be reasonably fitted with the generalized Stoner and Wohlfarth model [54] (Section III.A.1). We obtain the following anisotropy energy:

$$E_0(\vec{m})/v = -K_1 m_z^2 + K_2 m_x^2 - K_4(m_{x'}^2 m_{y'}^2 + m_{x'}^2 m_{z'}^2 + m_{y'}^2 m_{z'}^2) \qquad (3.11)$$

where K_1 and K_2 are the anisotropy constants along z and x, the easy and hard magnetization axis, respectively. K_4 is the forth order anisotropy constant and

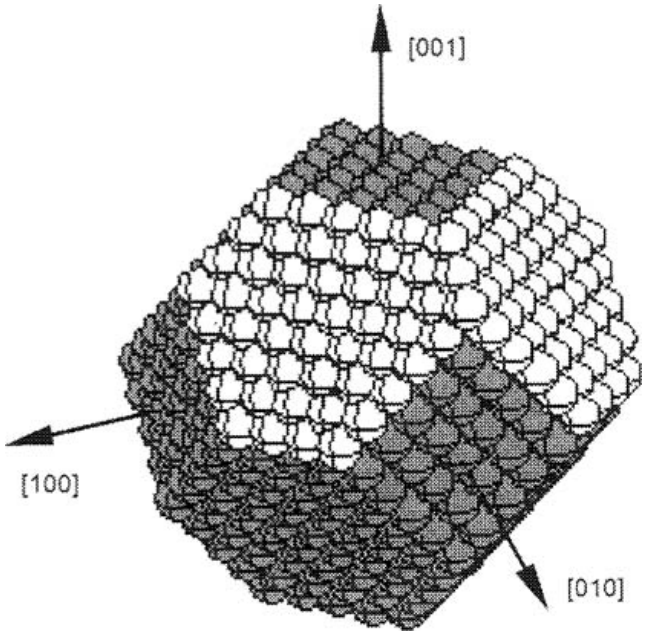

Figure 14. Scheme of a typical cluster shape with light-gray atoms belonging to the 1289 atoms truncated octahedron basis and dark-gray atoms belonging to the (111) and (001) added facets.

the $(x'y'z')$ coordinate system is deduced from (xyz) by a 45° rotation around the z axis. We obtained $K_1 = 2.2 \times 10^5 \text{J/m}^3$, $K_2 = 0.9 \times 10^5 \text{J/m}^3$, and $K_4 = 0.1 \times 10^5 \text{J/m}^3$. The corresponding theoretical surface is showed in Fig. 16. Furthermore, we measured the temperature dependence of the switching field distribution (Section IV.C.2). We deduced the blocking temperature of the particle $T_B \approx 14\,\text{K}$, and the number of magnetic atoms in this particle: $N \approx 1500$ atoms (Section IV.C.2). Detailed measurements on about 20 different particles showed similar three-dimensional switching field distributions with comparable anisotropy $(K_1 = (2.0 \pm 0.3) \times 10^5 \text{J/m}^3$, $(K_2 = (0.8 \pm 0.3) \times 10^5$ J/m^3, and $(K_4 = (0.1 \pm 0.05) \times 10^5 \text{J/m}^3)$ and size $(N = 1500 \pm 200$ atoms).

In the following, we analyze various contributions to the anisotropy energy of the Co clusters. Fine structural studies using EXAFS measurements [61] were performed on 500-nm-thick niobium films containing a very low concentration of cobalt clusters. They showed that niobium atoms penetrate the cluster surface to almost two atomic monolayers because cobalt and niobium are miscible elements. Further magnetic measurements [61] on the same samples showed that these two atomic monolayers are magnetically dead. For this reason, we estimated the shape anisotropy of the typical nearly spherical deposited cluster in Fig. 14 after removing two atomic monolayers from the surface. By calculating all the dipolar interactions inside the particle assuming a bulk magnetic moment of $\mu_a = 1.7\mu_B$, we estimated the shape anisotropy constants: $K_1 \approx 0.3 \times 10^5 \text{J/m}^3$ along the easy magnetization axis and $K_2 \approx 0.1 \times 10^5 \text{J/m}^3$

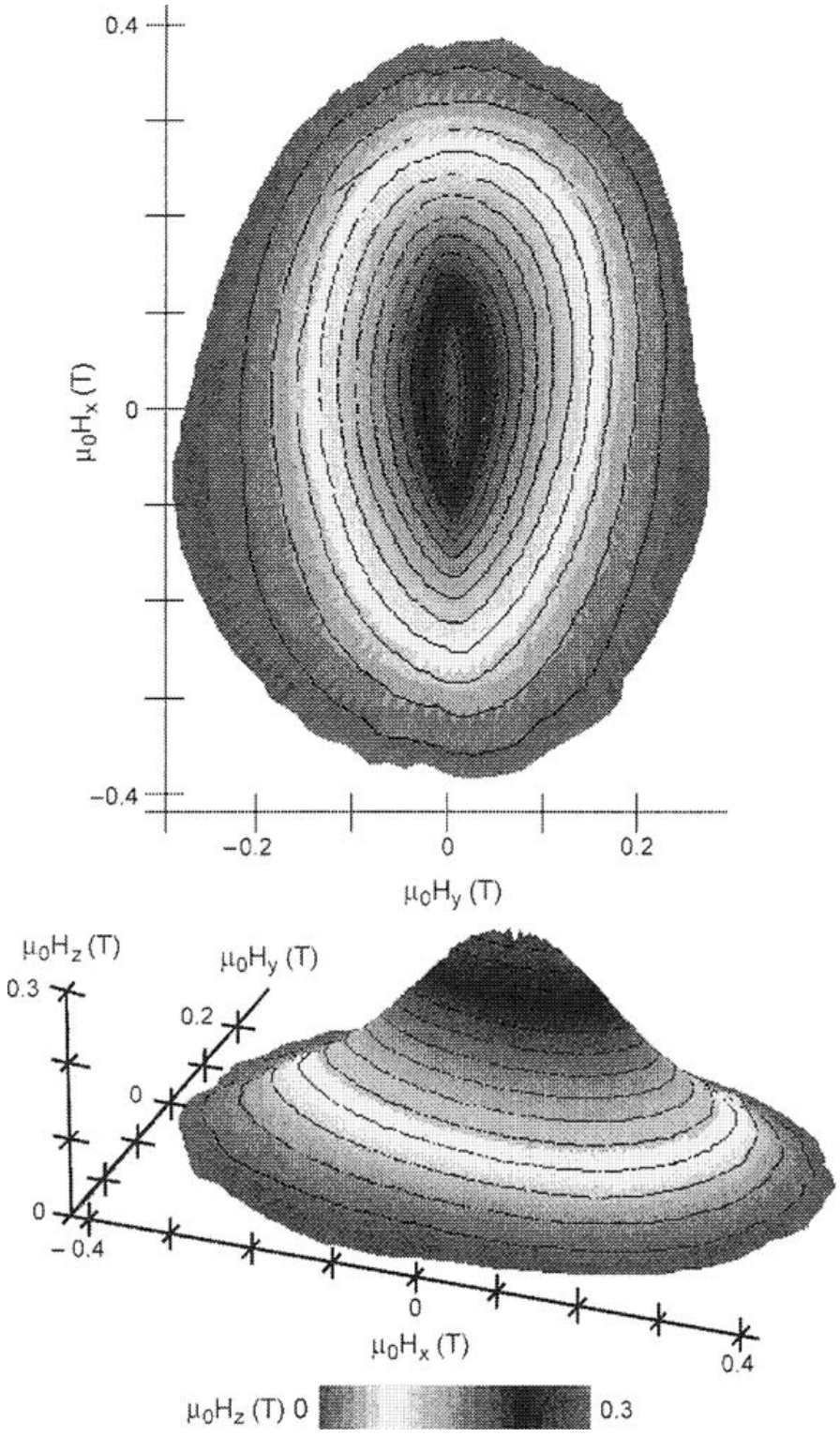

Figure 15. Top view and side view of the experimental three-dimensional angular dependence of the switching field of a 3-nm Co cluster at 35 mK. This surface is symmetrical with respect to the H_x–H_y plane, and only the upper part ($\mu_0 H_z > 0$ T) is shown. Continuous lines on the surface are contour lines on which $\mu_0 H_z$ is constant.

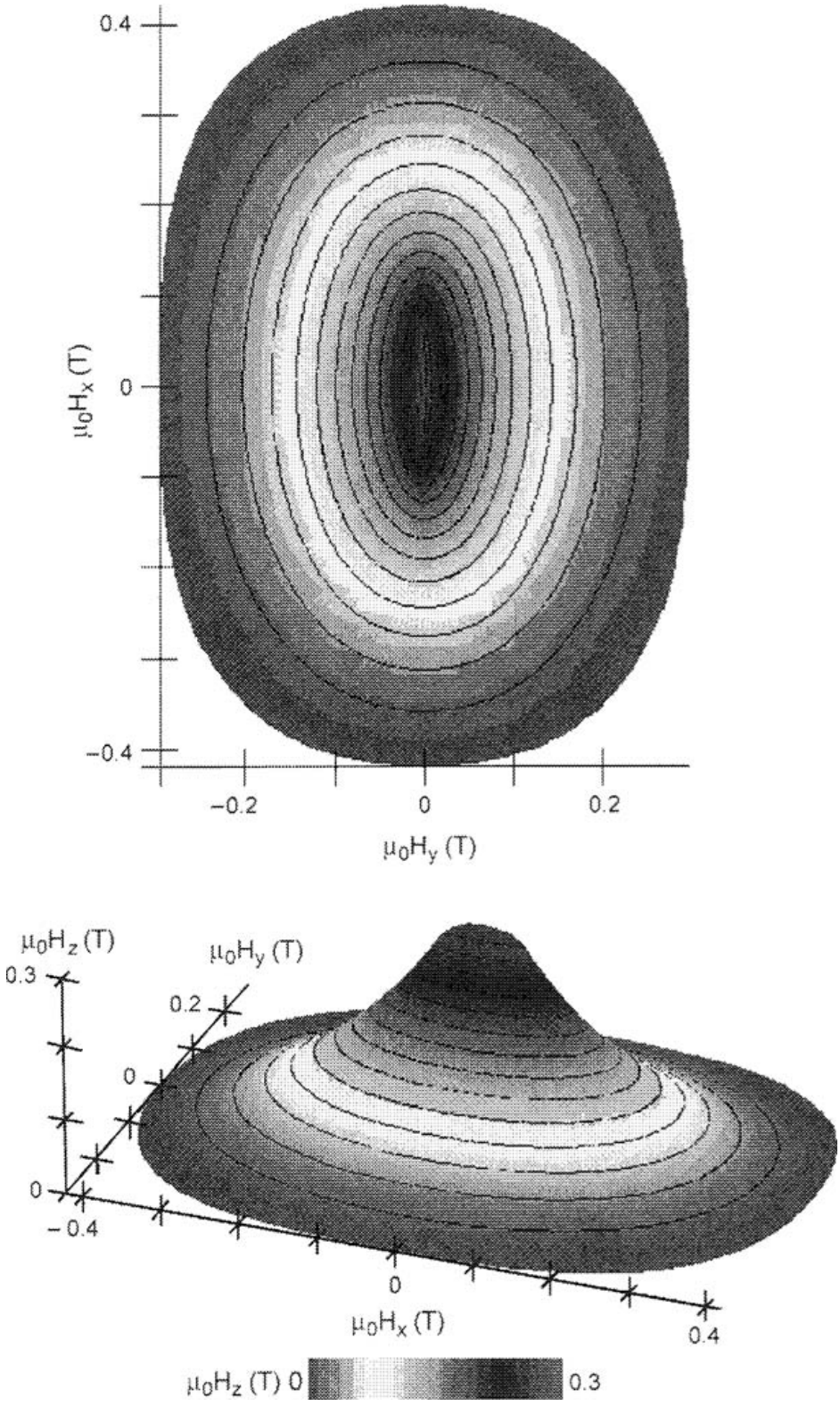

Figure 16. Top view and side view of the theoretical switching field surface considering second- and fourth-order terms in the anisotropy energy.

along the hard magnetization axis. These values are much smaller than the measured ones which means that E_{shape} is not the main cause of the second-order anisotropy in the cluster.

The fourth-order term $K_4 = 0.1 \times 10^5$ J/m^3 should arise from the cubic magnetocrystalline anisotropy in the *f.c.c.* cobalt clusters. However, this value is smaller than the values reported in previous works [62, 63]. This might by due to the different atomic environment of the surface atoms with respect to that of bulk *f.c.c.* Co. Taking the value of the bulk [62, 63], ($K_{bulk} = 1.2 \times 10^5$ J/m^3 only for the core atoms in the cluster, we find $K_{MC} \approx 0.2 \times 10^5$ J/m^3, which is in reasonable agreement with our measurements.

We expect that the contribution of the magnetoelastic anisotropy energy K_{MC} coming from the matrix-induced stress on the particle is also small. Indeed, using the co-deposition technique, niobium atoms cover uniformly the cobalt cluster creating an isotropic distribution of stresses. In addition, they can relax preferably inside the matrix and not in the particle volume because niobium is less rigid than cobalt. We believe therefore that only interface anisotropy $K_{surface}$ can account for the experimentally observed second-order anisotropy terms. Niobium atoms at the cluster surface might enhance this interface anisotropy through surface strains and magnetoelastic coupling. This emphasizes the dominant role of the surface in nanosized systems.

In conclusion, the three-dimensional switching field measurements of individual clusters give access to their magnetic anisotropy energy. A quantitative understanding of the latter is still difficult, but it seems that the cluster–matrix interface provides the main contribution to the magnetic anisotropy. Such interfacial effects could be promising to control the magnetic anisotropy in small particles in order to increase their blocking temperature up to the required range for applications.

3. *Uniform Rotation With Cubic Anisotropy*

We have seen in the previous section that the magnetic anisotropy is often dominated by second-order anisotropy terms. However, for nearly symmetric shapes, fourth-order terms* can be comparable or even dominant with respect to the second-order terms. Therefore, it is interesting to discuss further the features of fourth-order terms. We restrict the discussion to the 2D problem [54, 64] (see Ref. 55 for 3D).

The reversal of the magnetization is described by Eq. (3.3) which can be rewritten in 2D:

$$E(\theta) = E_0(\theta) - \mu_0 v M_s (H_x \cos(\theta) + H_y \sin(\theta)) \tag{3.12}$$

*For example, the fourth-order terms of *f.c.c.* magnetocrystalline anisotropy.

where v and M_s are the magnetic volume and the saturation magnetization of the particle, respectively, θ is the angle between the magnetization direction and x, H_x and H_y are the components of the external magnetic field along x and y, and $E_0(\theta)$ is the magnetic anisotropy energy. The conditions of critical fields ($\partial E/\partial\theta = 0$ and $\partial E^2/\partial\theta^2 = 0$) yield a parametric form of the locus of switching fields:

$$H_x = -\frac{1}{2\mu_0 v M_s}\left(\sin(\theta)\frac{dE}{d\theta} + \cos(\theta)\frac{d^2E}{d\theta^2}\right) \tag{3.13}$$

$$H_y = +\frac{1}{2\mu_0 v M_s}\left(\cos(\theta)\frac{dE}{d\theta} - \sin(\theta)\frac{d^2E}{d\theta^2}\right) \tag{3.14}$$

As an example we study a system with uniaxial shape anisotropy and cubic anisotropy. The total magnetic anisotropy energy can be described by

$$E_0(\theta) = vK_1 \sin^2(\theta + \theta_0) + vK_2 \sin^2(\theta)\cos^2(\theta) \tag{3.15}$$

where K_1 and K_2 are anisotropy constants (K_1 could be a shape anisotropy and K_2 the cubic crystalline anisotropy of a *f.c.c.* crystal.) θ_0 is a constant which allows to turn one anisotropy contribution with respect to the other one. Figure 17 displays an example of a critical curve which can easily be calculated from Eqs. (3.13) to (3.15). When comparing the standard Stoner–Wohlfarth astroid (Fig. 10) with Fig. 17, we can realize that the critical curve can cross itself several times. In this case, the switching field of magnetization depends on the path followed by the applied field. In order to understand this point, let us follow the energy potential [Eq. (3.15)], when sweeping the applied field as indicated in Fig. 18. When the field is in **A**, the energy E has two minima and the magnetization is in the metastable potential well. As the field increases, the metastable well becomes less and less stable. Let us compare two paths, one going along $\mathbf{A} \rightarrow \mathbf{B}_1 \rightarrow \mathbf{C} \rightarrow \mathbf{D} \rightarrow \mathbf{E}$, the other over $\mathbf{B}_2$ instead of $\mathbf{B}_1$. Figure 19 shows E in the vicinity of the metastable well for different field values along the considered paths (the stable potential well is not presented). One can realize that the state of the magnetization in **C** depends on the path followed by the field: Going over $\mathbf{B}_1$ leads to the magnetization state in the left metastable well (1), whereas going over $\mathbf{B}_2$ leads to the right metastable well (2). The latter path leads to magnetization switching in **D**, and the former one leads to a switching in **E**. Note that a small magnetization switch happens when reaching $\mathbf{B}_1$ or $\mathbf{B}_2$. Point **I** is a supercritical bifurcation.

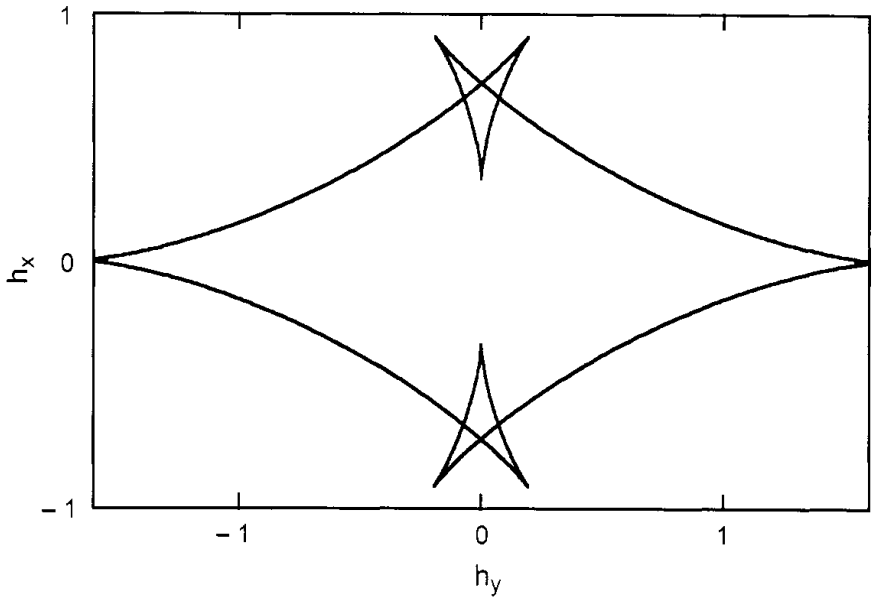

Figure 17. Angular dependence of the switching field obtained from Eqs. (3.13) to (3.15) with $K_1>0$ and $K_2=-2/3K_1$. The field is normalized by the factor $2K_1/(\mu_0 M_s)$.

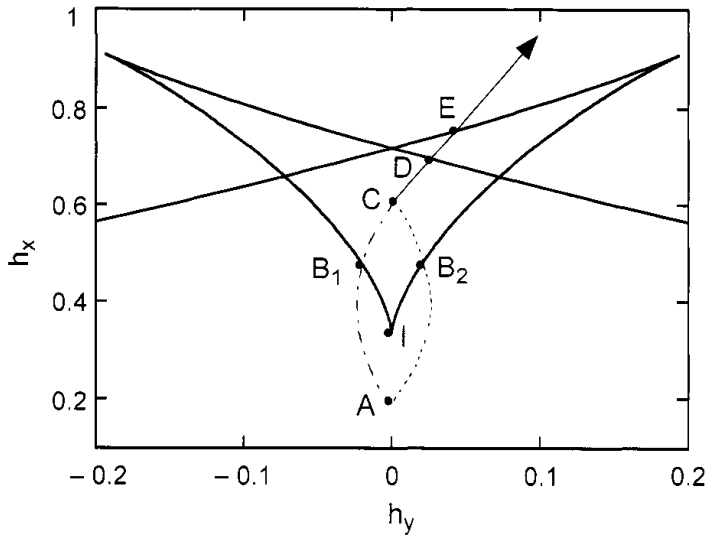

Figure 18. Enlargement of angular dependence of the switching field of Fig. 17. Two possible paths of the applied field are indicated: Starting from point **A** and going over the point $\mathbf{B}_1$ leads to magnetization reversal in **E**, whereas going over the point $\mathbf{B}_2$ leads to reversal in **D**.

The first measurement of such a field path dependence of the switching field were performed on single-domain FeCu nanoparticles of about 15 nm with a cubic crystalline anisotropy and a small arbitrarily oriented shape anisotropy [65]. Figure 20 presents switching field measurements of a 15-nm cobalt nano-

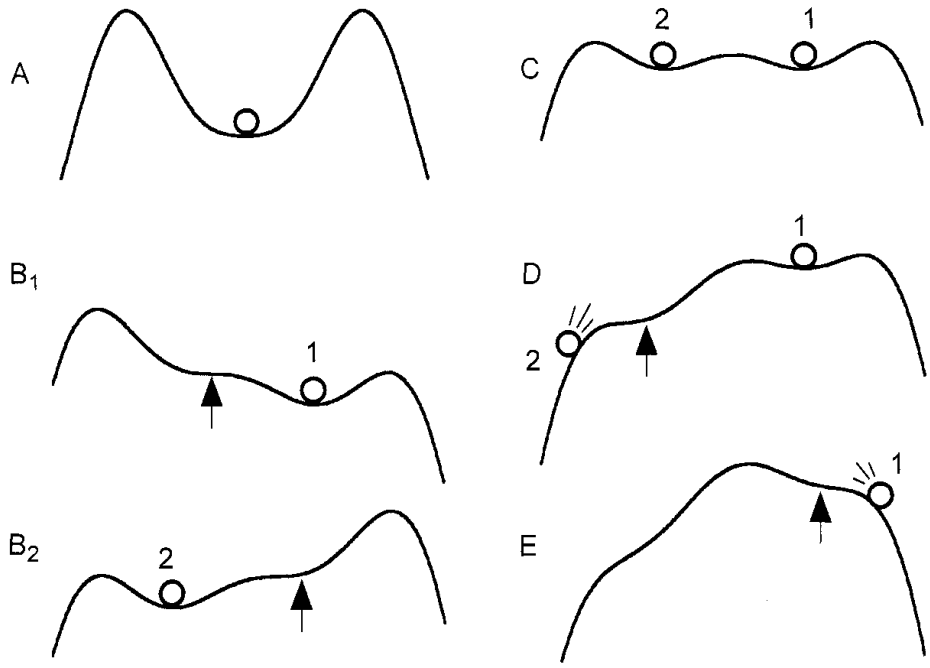

Figure 19. Scheme of the potential energy near the metastable state for different applied fields as indicated in Fig. 18. The balls represent the state of the magnetization, and the arrows locate the appearing or disappearing well.

particle showing clearly a contribution of cubic crystalline anisotropy and the field path dependence of the switching field.

B. Nonuniform Magnetization Reversal

We have seen in the previous sections that for extremely small particles, magnetization should reverse by uniform rotation. For somewhat larger single-domain particles, nonuniform reversal modes are more likely. The simplest one is the curling mode that is discussed in the following section.

1. Magnetization Reversal by Curling

The simplest nonuniform reversal mode is the curling reversal mode [2, 66]. The critical parameter is the exchange length $\lambda = \sqrt{A}/M_s$, delimiting the region of uniform rotation and curling (A is the exchange constant). Therefore in the case of the size $R > \lambda$ (R is, for example, the radius of a cylinder), magnetization reversal via curling is more favorable. In the following, we review the analytical result of an ellipsoid of rotation, which can be applied approximately to most of the shapes of nanoparticles or nanowires [67].

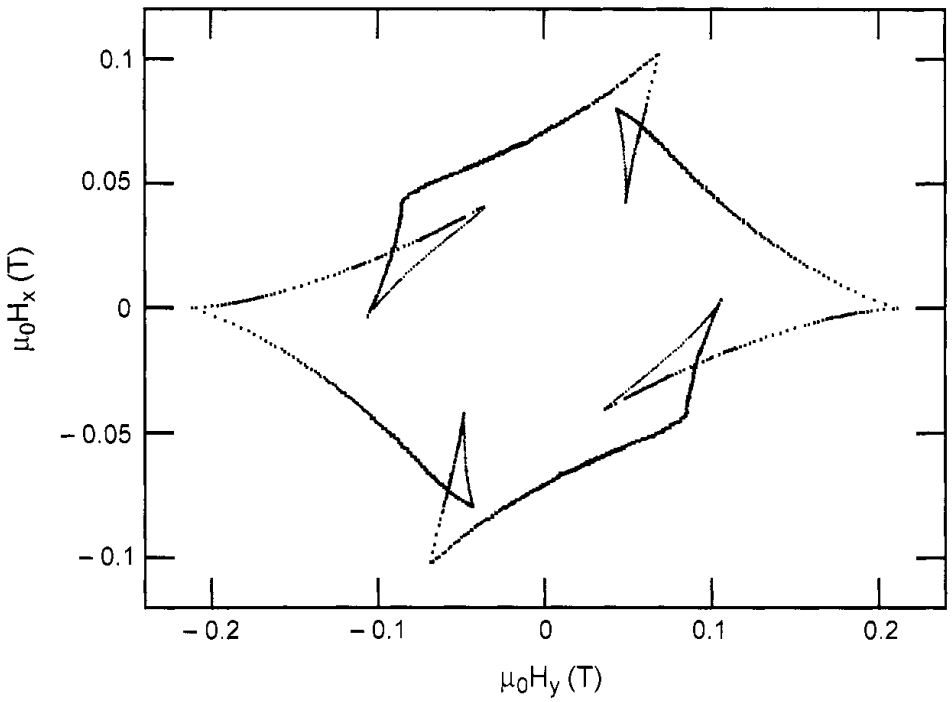

Figure 20. Angular dependence of the switching field of a 15-nm Co nanoparticle showing a strong influence of cubic crystalline anisotropy.

The variation of the switching field with the angle θ (defined between the applied field and the long axis of the ellipsoid) is given by [68]

$$H_{sw}^{0} = \frac{M_s}{2} \frac{a_x a_z}{\sqrt{a_z^2 \sin^2\theta + a_x^2 \cos^2\theta}} \tag{3.16}$$

where $a_{x,z} = 2\,N_{x,z} - k/S^2$, $N_{x,z}$ are the demagnetization factors, $S = R/\lambda$, and R is the minor semiaxis of the ellipsoid. The parameter k is a monotonically decreasing function of the aspect ratio of the ellipsoid. This function is plotted in Fig. 1 of Ref. 69. The smallest and highest value of k is that for an infinite cylinder ($k = 1.079$) and a sphere ($k = 1.379$), respectively.

For a long ellipsoid of rotation, the demagnetization factors are given by

$$N_z = \frac{1}{n^2 - 1} \frac{n}{\sqrt{n^2 - 1}} \ln\left(n - 1 + \sqrt{n^2 - 1}\right), \qquad N_x = \frac{1 - N_z}{2} \tag{3.17}$$

where n is the ratio of the length to the diameter.

For an infinite cylinder, Eq. (3.16) becomes [66, 70]

$$H_{sw}^{0} = \frac{M_s}{2} \frac{h_t(1+h_t)}{\sqrt{h_t^2 + (1+2h_t)\cos^2\theta}} \tag{3.18}$$

where $h_t = -1.079/S^2$. Equation (3.18) is a good approximation for a very long ellipsoid of rotation. It is plotted in Fig. 21 for several radii of an infinite cylinder.

The case of uniform rotation of magnetization was generalized by Thiaville to an arbitrary anisotropy energy function and to three dimensions (Section III.A.1). For the curling mode, this generalization is not possible. However, approximated calculations were proposed [67, 71, 72] and micromagnetic simulations were performed [73].

2. *Experimental Evidence for Magnetization Reversal by Curling*

We report here the first studies of isolated nanoscale wires with diameters smaller than 100 nm, for which single-domain states could be expected [35, 74]. The cylindrical geometry, with its large shape anisotropy, is well-suited

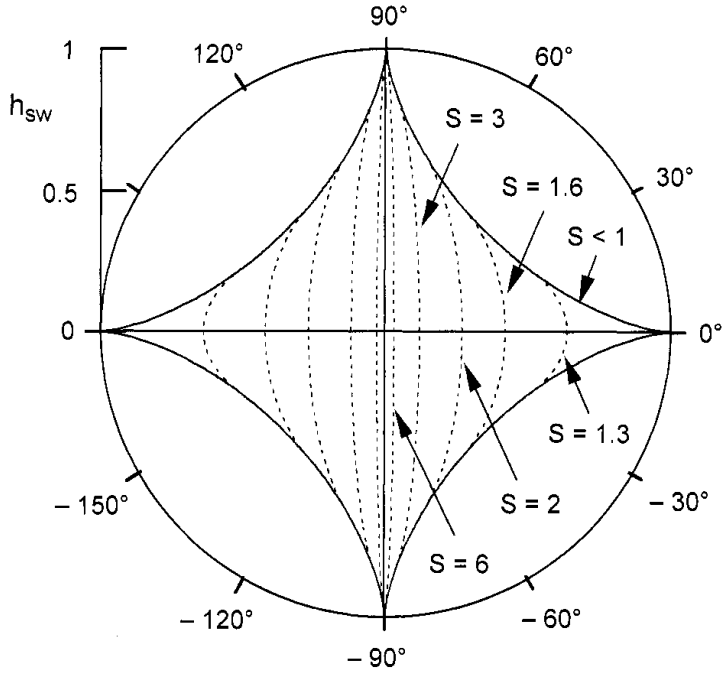

Figure 21. Angular dependence of the switching field of an infinite cylinder for several reduced cylinder radii S. For $S<1$, the switching field is given by the uniform rotation mode (Section III.A).

for comparison with theory. Ni wires were produced by filling electrochemically the pores of commercially available nanoporous track-etched polycarbonate membranes of thicknesses of 10 μm. The pore size was chosen in the range of 30 to 100 nm [75, 76]. In order to place one wire on the SQUID detector, we dissolved the membrane in chloroform and put a drop on a chip of some hundreds of SQUIDs. Magnetization measurements were performed on SQUIDs with a single isolated wire (Fig. 1).

The angular dependence of the switching field of wires with 45- and 92-nm diameter are shown in Fig. 22. These measurements are in quantitative agreement with the curling mode [Eq. (3.16)]. Nevertheless, dynamical measurements showed a nucleation volume that is much smaller than the wire volume [35, 74] (Section IV.C.3). Therefore, we believe that the magnetization reversal starts close to curling instability, but the nucleation happens in a small fraction of the wire only, then rapidly propagating along the whole sample. This picture is also in good agreement with micromagnetic simulations [73] and the micromagnetic model of Braun [77].*

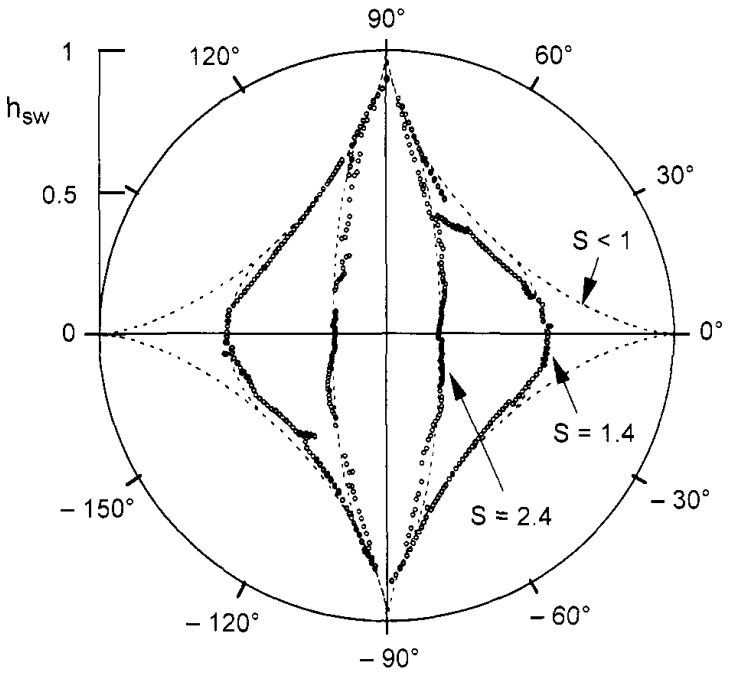

Figure 22. Angular dependence of the switching field of two Ni wires with a diameter of 45 nm and 92 nm, that is, $S = 1.4$ and 2.4. The switching fields are normalized by 125 mT and 280 mT, respectively.

*Note that the curling model only predicts an instability. There has never been a claim to describe what happens afterwards [2].

The angular dependence of the switching field of Ni wires with larger diameters (270–450 nm) were measured at room temperature by Lederman et al. [78]. Their results could roughly be explained by the curling mode.

3. *Magnetization Reversal by Nucleation and Annihilation of Domain Walls*

For magnetic particles that have at least two dimensions much larger than the domain wall width, the magnetization reversal may occur via nucleation/propagation and annihilation of one or several domain walls happening at two or more applied fields. We focus here on a 30-nm-thick elliptic Co particle defined by electron beam lithography and lift-off techniques out of sputtered thin films (inset of Fig. 23) [79]. The Co film has a nanocrystalline structure leading to a magnetically soft material with a coercive field value of 3 mT at 4 K. Therefore we neglected the magnetocrystalline anisotropy. The nanofabricated particles have an elliptic contour with in-plane dimensions of 300 nm $\times$ 200 nm and a thickness of 30 nm.

In order to study the domain structure of our particles, we measure the angular dependence of hysteresis loops. Figure 23 shows a typical hysteresis loop of an individual Co particle. The magnetic field is applied in the plane of the particle. The hysteresis loop is mainly characterized by two magnetization jumps. Starting from a saturated state, the first jump can be associated with domain wall nucleation and the second jump can be associated with domain wall annihilation. During these jumps, the magnetization switches in less than 100 μs (our time resolution, see Section II.B.4). The reversible central region of the hysteresis loops is evidence for the motion of the domain wall through the particle.

The simplest domain structure, showing such a hysteresis loop, has been proposed by van den Berg [80] in zero field and calculated for fields smaller than the saturation field by Bryant and Suhl [81].* This domain structure has been observed experimentally on low anisotropy circular thin film disks (100 μm in diameter) using high-resolution Kerr techniques [82]. In zero field, the particle has a vortex-like domain wall as shown in Fig. 23. When a magnetic field is applied, this domain wall is pushed to the border of the particle. For higher fields the domain wall is annihilated and the particle becomes single domain. The main conditions of the van den Berg model are (i) that the magnetic material is very soft and (ii) that the system is two-dimensional. The first condition is satisfied by our particles because they are made of a randomly oriented nanocrystallized Co, being very soft. The second condition is not quite well satisfied however, MFM measurements confirmed this domain structure [83]. Furthermore, we obtained

*Note that these models are 2D and neglect the domain wall width. Therefore, they can give only a qualitative description.

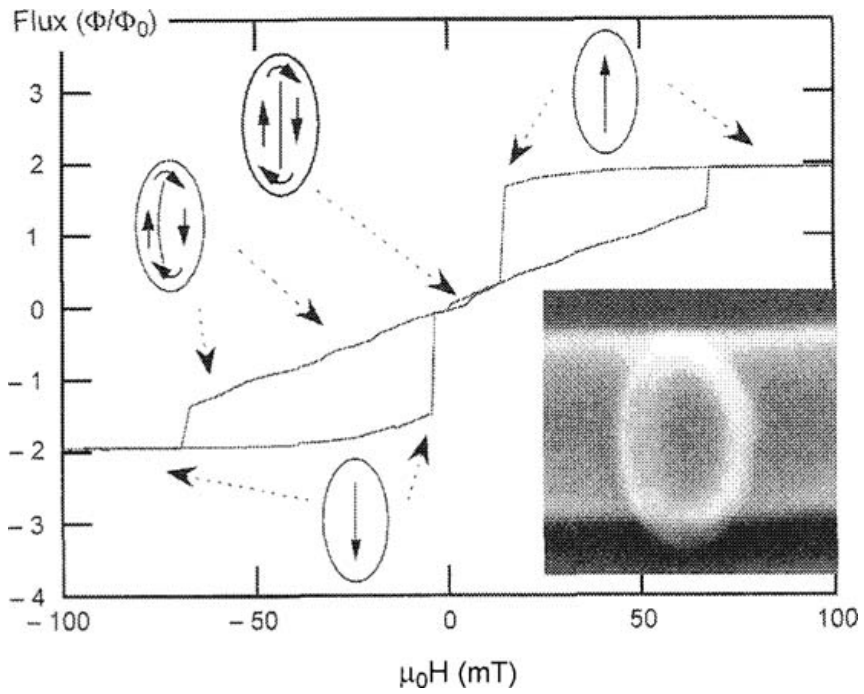

Figure 23. Hysteresis loops at 0.1 K of the elliptic Co particle seen in the inset which shows the electron micrograph of the wire of the SQUID loop with a Co particle (300 nm × 200 nm × 30 nm). The in-plane field is applied along the long axis of the particles. The domain wall structure in an elliptical particle is also presented schematically as proposed by van den Berg. Arrows indicate the spin direction. The two small magnetization jumps near $\approx \pm 5$ mT might be due to the reversal of the center vortex of the domain structure.

similar results for thinner particles (10 and 20 nm). More complicated domain structures as proposed by van den Berg [79, 80] may be excluded by the fact that similar Co particles of length smaller than 200 nm are single domain [22, 59].

After studying the magnetization reversal of individual particles, the question arises as to how the properties of a macroscopic sample are based on one-particle properties. In order to answer this question, we fabricated a sample consisting of 1.8×10^7 nearly identical elliptic Co particles of about the same dimensions and material as the individual particle studied above. These particles are placed on an Si substrate with a spacing of 2 μm. Because of this large spacing, dipole interactions between particles are negligible. Figure 24 shows the hysteresis loop of the array of Co particles when the field is applied parallel to the long axis of the particle. This hysteresis loop shows the same characteristics as the hysteresis loop of one particle (Fig. 23) that is, nucleation and annihilation of domain walls. Because of switching field distributions mainly due to surface defects and a slight distribution of particle sizes, shapes, and so on, the domain wall nucleation and annihilation are no longer discontinuous

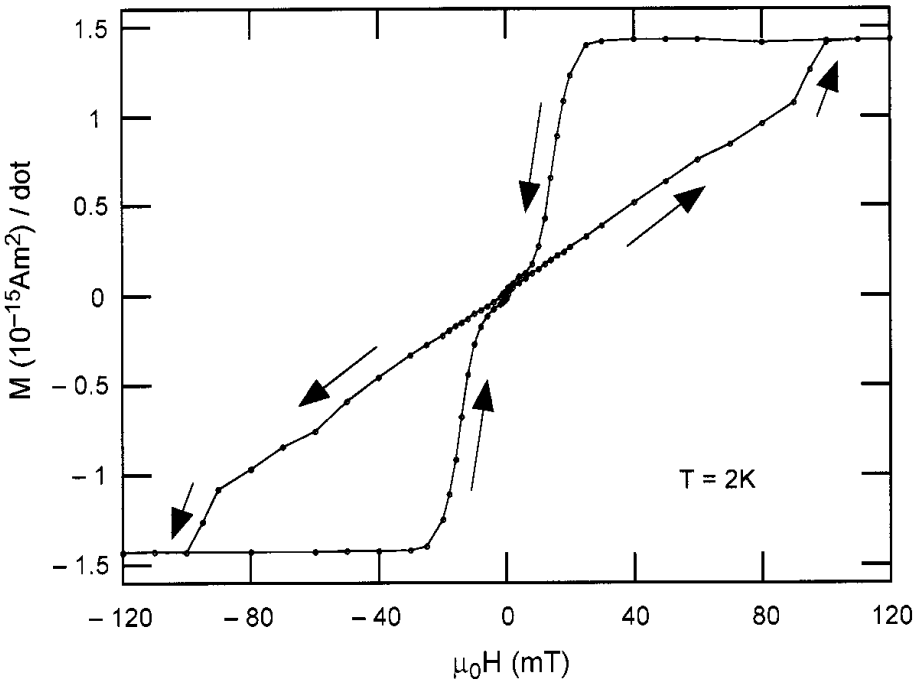

Figure 24. Hysteresis loops of the magnetic moment of the array of 1.8×10^7 Co particles (300 nm × 200 nm × 30 nm). The in-plane field is applied along the long axis of the particles.

although still irreversible. They take place along continuous curves with a width of about 10 mT.

IV. INFLUENCE OF TEMPERATURE ON THE MAGNETIZATION REVERSAL

The thermal fluctuations of the magnetic moment of a single-domain ferromagnetic particle and its decay towards thermal equilibrium were introduced by Néel [9, 10] and further developed by Bean and Livingston [84, 85] and Brown [86–88]. The simplest case is an assembly of independent particles having no magnetic anisotropy. In the absence of an applied magnetic field, the magnetic moments are randomly oriented. The situation is similar to paramagnetic atoms where the temperature dependence of the magnetic susceptibility follows a Curie behavior, and the field dependence of magnetization is described by a Brillouin function. The only difference is that the magnetic moments of the particles are much larger than those of the paramagnetic atoms. Therefore, the quantum mechanical Brillouin function can be replaced by the classical limit for larger magnetic moments, namely the Langevin function. This theory is called

superparamagnetism. The situation changes, however, as soon as magnetic anisotropy is present which establishes one or more preferred orientations of the particle's magnetization (Section III). In the following, we present an overview over the simplest model describing thermally activated magnetization reversal of single isolated nanoparticles which is called the Néel–Brown model. After a brief review of the model (Section IV. A), we present experimental methods to study the thermally activated magnetization reversal (Section IV. B). Finally, we discuss some applications of the Néel–Brown model (Section IV.C).

A. Néel–Brown Model of Thermally Activated Magnetization Reversal

In Néel and Brown's model of thermally activated magnetization reversal, a single-domain magnetic particle has two equivalent ground states of opposite magnetization separated by an energy barrier which is due to shape and crystalline anisotropy. The system can escape from one state to the other by thermal activation over the barrier. Just as in the Stoner–Wohlfarth model, they assumed uniform magnetization and uniaxial anisotropy in order to derive a single relaxation time. Néel supposed further that the energy barrier between the two equilibrium states is large in comparison to the thermal energy $k_B T$ which justified a discrete orientation approximation [9, 10]. Brown criticized Néel's model because the system is not explicitly treated as a gyromagnetic one [86–88]. Brown considered the magnetization vector in a particle to wiggle around an energy minimum, then jump to the vicinity of the other minimum, then wiggle around there before jumping again. He supposed that the orientation of the magnetic moment may be described by a Gilbert equation with a random field term that is assumed to be white noise. On the basis of these assumptions, Brown was able to derive a Fokker–Planck equation for the distribution of magnetization orientations. Brown did not solve his differential equation. Instead he tried some analytic approximations and an asymptotic expansion for the case of the field parallel or perpendicular to the easy axis of magnetization. More recently, Coffey et al. [89, 90] found by numerical methods an exact solution of Brown's differential equation for uniaxial anisotropy and an arbitrary applied field direction. They also derived an asymptotic general solution for the case of large energy barriers in comparison to the thermal energy $k_B T$. This asymptotic solution is of particular interest for single-particle measurements and is reviewed in the following.

For a general asymmetric bistable energy potential $E = E(\vec{m}, \vec{H})$ [Eq. (3.3)] with the orientation of magnetization $\vec{m} = \vec{M}/M_S$ (M_S is the spontaneous magnetization), $\vec{H}$ is the applied field, and with minima at $\vec{n}_1$ and $\vec{n}_2$ separated by a potential barrier containing a saddle point at $\vec{n}_0$ (with the $\vec{n}_i$ coplanar), and in the case of $\beta(E_0 - E_i) \gg 1$ where $\beta = 1/k_B T$, and $E_i = E(\vec{n}_i, \vec{H})$, Coffey et al. showed

that the longest relaxation time* is given by the following equation which is valid in the intermediate to high damping limit (IHD) defined by $\alpha\,\beta\,(E_0-E_i)>1$ [91]:

$$\tau^{-1}=\frac{\Omega_0}{2\pi\omega_0}\left[\omega_1 e^{-\beta(E_0-E_1)}+\omega_2 e^{-\beta(E_0-E_2)}\right] \tag{4.1}$$

where ω_0 and Ω_0 are the saddle and damped saddle angular frequencies:

$$\omega_0=\frac{\gamma}{M_s}\sqrt{-c_1^{(0)}c_2^{(0)}} \tag{4.2}$$

$$\Omega_0=\frac{\gamma}{M_s}\frac{\alpha}{1+\alpha^2}\left[-c_1^{(0)}-c_2^{(0)}+\sqrt{(c_2^{(0)}-c_1^{(0)})^2-4\alpha^{-2}c_1^{(0)}c_2^{(0)}}\right] \tag{4.3}$$

ω_1 and ω_2 are the well angular frequencies:

$$\omega_i=\frac{\gamma}{M_s}\sqrt{c_1^{(i)}c_2^{(i)}} \tag{4.4}$$

with $i=1$ and 2. $c_1^{(j)}$ and $c_2^{(j)}$ $(j=0,\ 1,\ 2)$ are the coefficients in the truncated Taylor series of the potential at well and saddle points—that is, the curvatures of the potential at well and saddle points. γ is the gyromagnetic ratio, $\alpha=\nu\,\gamma M_s$ is the dimensionless damping factor and ν is the friction in Gilbert's equation (ohmic damping).

Whereas in the low damping limit (LD), defined by $\alpha\,\beta(E_0-E_i)<1$, the longest relaxation time is given by [92, 93]

$$\tau^{-1}=\frac{\alpha}{2\pi}\left[\omega_1\beta(E_0-E_1)e^{-\beta(E_0-E_1)}+\omega_2\beta(E_0-E_2)e^{-\beta(E_0-E_2)}\right] \tag{4.5}$$

In this case, the energy dissipated in one cycle of motion in the well is very small in comparison to the thermal energy k_BT.

Experimentally, relaxation is observed only if τ is of the order of magnitude of the measuring time of the experiment. This implies for all known single-particle measurement techniques that $\beta(E_0-E_i)\gg 1$; that is, the asymptotic solutions (4.1) and (4.5) are always a very good approximation to the exact

*The inverse of the longest relaxation time is determined by the smallest nonvanishing eigenvalue of the appropriate Fokker–Planck equation [89, 90]. All other eigenvalues can be neglected in the considered asymptotic limit of $\beta(E_0-E_i)\gg 1$.

solution of Brown's Fokker–Planck equation [94]. Due to an applied field, $\beta(E_0-E_1) \gg \beta(E_0-E_2)$ (taking E_2 as the metastable minimum) might be true. Then the first exponential in Eq. (4.1) and (4.5) can be neglected.

Concerning the possible values of α, we remark that little information is available. Typical values should be between 0.01 and 5 [8], meaning that in practice $\alpha\beta(E_0-E_i)$ can be $\gg 1$, $\ll 1$, or ≈ 1. Thus the distinction between Eqs. (4.1) and (4.5) becomes important.

Finally, we note that $c_1^{(j)}$ and $c_2^{(j)}$ ($j=0, 1, 2$) can be found experimentally by measuring the critical surface of the switching field and applying the calculation of Thiaville (Section III.A.1) [55].

B. Experimental Methods for the Study of the Néel–Brown Model

As discussed in the previous section, in the Néel–Brown model of thermally activated magnetization reversal a single-domain magnetic particle has two equivalent ground states of opposite magnetization separated by an energy barrier due to, for instance, shape and crystalline anisotropy. The system can escape from one state to the other either by thermal activation over the barrier at high temperatures or by quantum tunneling at low temperatures (Section V). At sufficiently low temperatures and at zero field, the energy barrier between the two states of opposite magnetization is much too high to observe an escape process. However, the barrier can be lowered by applying a magnetic field in the opposite direction to that of the particle's magnetization. When the applied field is close enough to the switching field at zero temperature H_{sw}^0, thermal fluctuations are sufficient to allow the system to overcome the barrier, and the magnetization is reversed.

In the following, we discuss three different experimental methods for studying this stochastic escape process which are called waiting time, switching field, and telegraph noise measurements.

1. Waiting Time Measurements

The waiting time method consists in measuring the probability that the magnetization has not switched after a certain time. In the case of an assembly of identical and isolated particles, it corresponds to measurements of the relaxation of magnetization. However, in most particle assemblies, broad distributions of switching fields lead to logarithmic decay of magnetization, and the switching probability is hidden behind the unknown distributions functions [8]. For individual particle studies, waiting time measurements give direct access to the switching probability (Fig. 25). At a given temperature, the magnetic field H is increased to a waiting field H_w near the switching field H_{sw}^0. Next, the elapsed time until the magnetization switches is measured. This process is repeated several hundred times, yielding a waiting time histogram. The integral of this histogram and proper normalization yields the probability that the magnetization

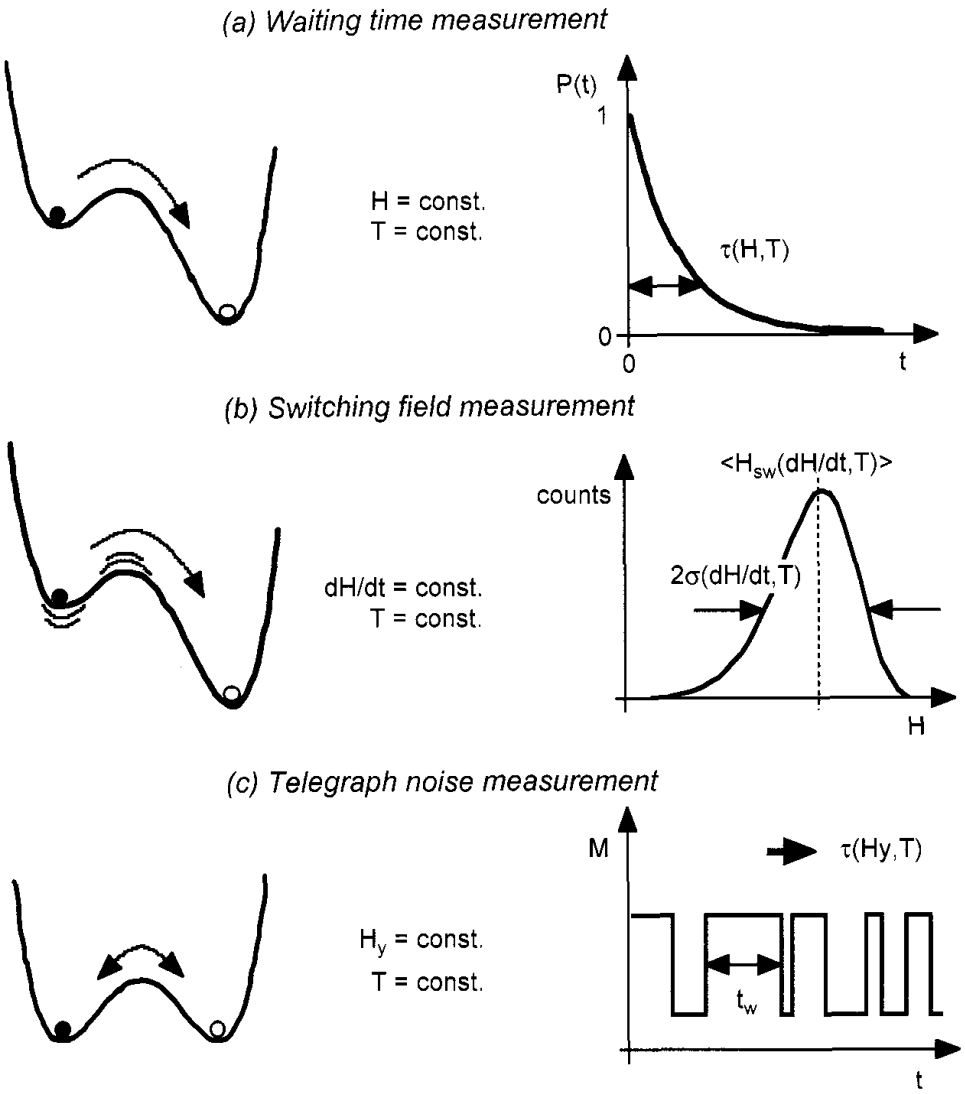

Figure 25. Schema of three methods for studying the escape from a potential well: waiting time and telegraph noise measurements give direct access to the switching time probability $P(t)$, whereas switching field measurements yield histograms of switching fields.

has not switched after a time t. This probability is measured at different waiting fields H_w and temperatures in order to explore several barrier heights and thermal activation energies.

According to the Néel–Brown model, the probability that the magnetization has not switched after a time t is given by

$$P(t) = e^{-t/\tau} \tag{4.6}$$

and τ (inverse of the switching rate) can be expressed by an Arrhenius law of the form

$$\tau^{-1}(\varepsilon) = B\varepsilon^{a-b-1}e^{-A\varepsilon^a} \tag{4.7}$$

where $\varepsilon = (1 - H/H_{sw}^0)$ and A, B, a, and b depend on damping, temperature, energy barrier height [Eqs. (3.5)–(3.10) and (4.1)–(4.5)], curvatures at well and saddle points, and reversal mechanism (thermal or quantum) (cf. Table 1 of Ref. 95). For simplicity, experimentalists have often supposed a constant pre-exponential factor τ_0^{-1} instead of $B\varepsilon^{a-b-1}$.

The adjustment of Eq. (4.6) to the measured switching probabilities yields a set of mean waiting times $\tau^{-1}(H_w, T)$. In order to adjust the Néel–Brown model to this set of data, we propose the following relation that can be found by inserting $\varepsilon = (1 - H_w/H_{sw}^0)$ into Eq. (4.7):

$$H_w = H_{sw}^0\left(1 - \left[\frac{1}{A}\ln(\tau B\varepsilon^{a-b-1})\right]^{1/a}\right) \tag{4.8}$$

When plotting the H_w values as a function of $[T \ln (\tau\ B\ \varepsilon^{a+b-1})]^{1/a}$, all points should gather on a straight line (master curve) by choosing the proper value for the constants B, a, and b [a and b should be given by Eqs. (3.5)–(3.10) and (4.1)–(4.5)]. A can be obtained from the slope of the master.

The number of exploitable decades for τ values is limited for waiting time measurements: Short-time (milliseconds) experiments are limited by the inductance of the field coils* and long-time (minutes) studies by the stability of the experimental setup. Furthermore, the total acquisition time for a set of $\tau^{-1}(H_w, T)$ is rather long (weeks). Thus a more convenient method is needed for single-particle measurements—namely, the switching field method.

2. *Switching Field Measurements*

For single-particle studies, it is often more convenient to study magnetization reversal by ramping the applied field at a given rate and measuring the field value as soon as the particle magnetization switches. Next, the field ramp is reversed and the process repeated. After several hundred cycles, switching field histograms are established, yielding the mean switching field $\langle H_{sw}\rangle$ and the width σ_{sw} (rms deviation). Both mean values are measured as a function of the field sweeping rate and temperature (Fig. 25).

From the point of view of thermally activated magnetization reversal, switching field measurements are equivalent to waiting time measurements because the

*A solution to this problem might be a superposition of a constant applied field and a small pulse field.

time scale for the sweeping rate is typically more than 8 orders of magnitude greater than the time scale of the exponential prefactor, which is in general around 10^{-10} s. We can therefore apply the Néel–Brown model described above. The mathematical transformation from a switching time probability [Eqs.(4.6)–(4.7)] to a switching field probability was first given by Kurkijärvi [96] for the critical current in SQUIDs. A more general calculation was evaluated by Garg [95]. In many cases, the mean switching field $\langle H_{sw} \rangle$ can be approximated by the first two terms of the development of Garg [95]:

$$\langle H_{sw}(T, v) \rangle \approx H_{sw}^0 \left(1 - \left[\frac{1}{A} \ln \left(\frac{H_{sw}^0 B}{vaA^{1-b/a}} \right) \right]^{1/a} \right) \tag{4.9}$$

where the field sweeping rate is given by $v = dH/dt$. The width of the switching field distribution σ_{sw} can be approximated by the first term of Garg's development:

$$\sigma_{sw} \approx H_{sw}^0 \frac{\pi}{\sqrt{6}a} \left(\frac{1}{A} \right)^{1/a} \left[\ln \left(\frac{H_{sw}^0 B}{vaA^{1-b/a}} \right) \right]^{(1-a)/a} \tag{4.10}$$

In the case of a constant preexponential factor τ_0^{-1}, the calculation of $\langle H_{sw} \rangle$ and σ_{sw} is more simple and is given by Eqs. (4) and (5) in Ref. 36, respectively.

Similar to the waiting time measurements, a scaling of the model to a set of $\langle H_{sw}(T, v) \rangle$ values can be done by plotting the $\langle H_{sw}(T, v) \rangle$ values as a function of $[T \ln((H_{sw}^0 B)/(vaA^{1-b/a}))]^{1/a}$. All points should gather on a straight line by choosing the proper value for the constants [a and b should be given by Eqs. (3.5)–(3.10) and (4.1)–(4.5)].

The entire switching field distribution $P(H)$ can be calculated iteratively by the following equation [96]:

$$P(H) = \tau^{-1}(H) v^{-1} \left[1 - \int_0^H P(H') dH' \right] \tag{4.11}$$

3. *Telegraph Noise Measurements*

In order to study the superparamagnetic state* of a single particle, it is simply necessary to measure the particle's magnetization as a function of time. We call

*At zero applied field, a single-domain magnetic particle has two equivalent ground states of opposite magnetization separated by an energy barrier. When the thermal energy $k_B T$ is sufficiently high, the total magnetic moment of the particle can fluctuate thermally, like a single spin in a paramagnetic material. Such magnetic behavior of an assembly of independent single-domain particles is called superparamagnetism [8, 84, 85].

this telegraph noise measurement as stochastic fluctuations between two states are expected. According to the Néel–Brown model, the mean time τ spent in one state of magnetization is given by an Arrhenius law of the form of Eq. (4.7). As τ increases exponentially with decreasing temperature, it is very unlikely that an escape process will be observed at low temperature. However, applying a constant field in direction of a hard axis (hard plane) of magnetization reduces the height of the energy barrier (Fig. 25). When the energy barrier is sufficiently small, the particle's magnetization can fluctuate between two orientations which are close to a hard axis (hard plane) of magnetization. The time spent in each state follows an exponential switching probability law as given by Eqs. (4.6) and (4.7) with $a = 2$ [Eq. (3.8)].*

C. Experimental Evidence for the Néel–Brown Model

The Néel–Brown model is widely used in magnetism, particularly in order to describe the time dependence of the magnetization of collections of particles, thin films, and bulk materials. However until recently, all the reported measurements, performed on individual particles, were not consistent with the Néel–Brown theory. This disagreement was attributed to the fact that real samples contain defects, ends, and surfaces that could play an important, if not dominant, role in the physics of magnetization reversal. It was suggested that the dynamics of reversal occurs via a complex path in configuration space, and that a new theoretical approach is required to provide a correct description of thermally activated magnetization reversal even in single-domain ferromagnetic particles [19, 59]. Similar conclusions were drawn from numerical simulations of the magnetization reversal [97–101].

A few years later, micro-SQUID measurements on individual Co nanoparticles showed for the first time a very good agreement with the Néel–Brown model by using waiting time, switching field, and telegraph noise measurements [36–39]. It was also found that sample defects, especially sample oxidation, play a crucial role in the physics of magnetization reversal.

In the following subsections, we review some typical results concerning nanoparticles (Section IV.C.1), clusters (Section IV.C.2), and wires (Section IV.C.3). In Section IV.C.4, we point out the main deviations from the Néel–Brown model which are due to defects.

1. Application to Nanoparticles

One of the important predictions of the Néel–Brown model concerns the exponential not-switching probability $P(t)$ [Eq. (4.6)] which can be measured directly via waiting time measurements (Section IV.B.1): At a given temperature, the

*Note that for a slightly asymmetric energy potential, one switching probability can be so long that two-level fluctuation becomes practically unobservable.

magnetic field is increased to a waiting field H_w which is close to the switching field. Then, the elapsed time is measured until the magnetization switches. This process is repeated several hundred times, in order to obtain a waiting time histogram. The integral of this histogram gives the not-switching probability $P(t)$ which is measured at several temperatures T and waiting fields H_w. The inset of Fig. 26 displays typical measurements of $P(t)$ performed on a Co nanoparticle. All measurements show that $P(t)$ is given by an exponential function described by a single relaxation time τ.

The validity of Eqs. (3.5) and (4.7) is tested by plotting the waiting field H_w as a function of $[T \ln(\tau/\tau_0)]^{2/3}$.* If the Néel–Brown model applies, all points should collapse onto one straight line (master curve) by choosing the proper values for τ_0. Figure 26 shows that the data set $\tau(H_w,T)$ falls on a master curve provided that $\tau_0 \approx 3 \times 10^{-9}$ s. The slope and intercept yield the values $E_0 = 214{,}000$ K and $H_{sw}^0 = 143.05$ mT. The energy barrier E_0 can be approximately converted to a

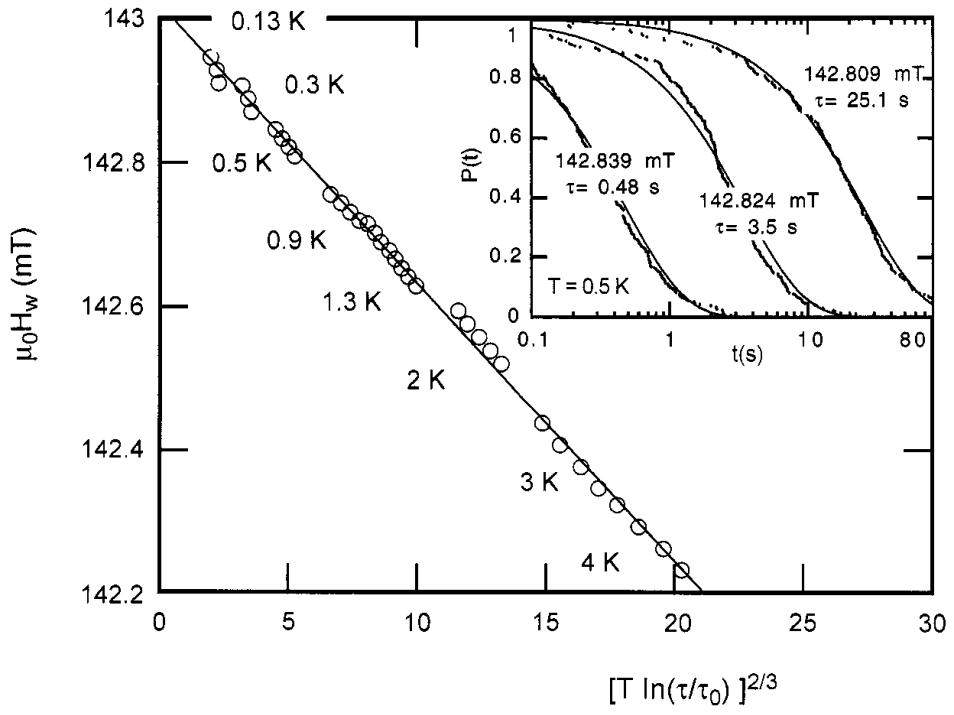

Figure 26. Scaling plot of the mean switching time $\tau(H_w,T)$ for several waiting fields H_w and temperatures (0.1 s $< \tau(H_w,T) <$ 60 s) for a Co nanoparticle. The scaling yields $\tau_0 \approx 3 \times 10^{-9}$ s. *Inset*: Examples of the probability of not-switching of magnetization as a function of time for different applied fields and at 0.5 K. *Full lines* are data fits with an exponential function: $P(t) = e^{-t/\tau}$.

*$a = 3/2$ because the field was applied at about 20° from the easy axis of magnetization [Eq. (3.5)].

thermally "activated volume" by using $V = E_0/(\mu_0 M_S H_{sw}^0) \approx (25\,\text{nm})^3$ which is very close to the particle volume estimated by SEM. This agreement is another confirmation of a magnetization reversal by uniform rotation. The result of the waiting time measurements are confirmed by switching field and telegraph noise measurements [36, 37]. The field and temperature dependence of the exponential prefactor τ_0 is taken into account in Ref. 90.

2. *Application to Co Clusters*

Figure 27 presents the angular dependence of the switching field of a 3-nm Co cluster measured at different temperatures. At 0.03 K, the measurement is very close to the standard Stoner–Wohlfarth astroid (Fig. 10). For higher temperatures the switching field becomes smaller and smaller. It reaches the origin at about 14 K, yielding the blocking temperature $T_B = 14\,\text{K}$ of the cluster

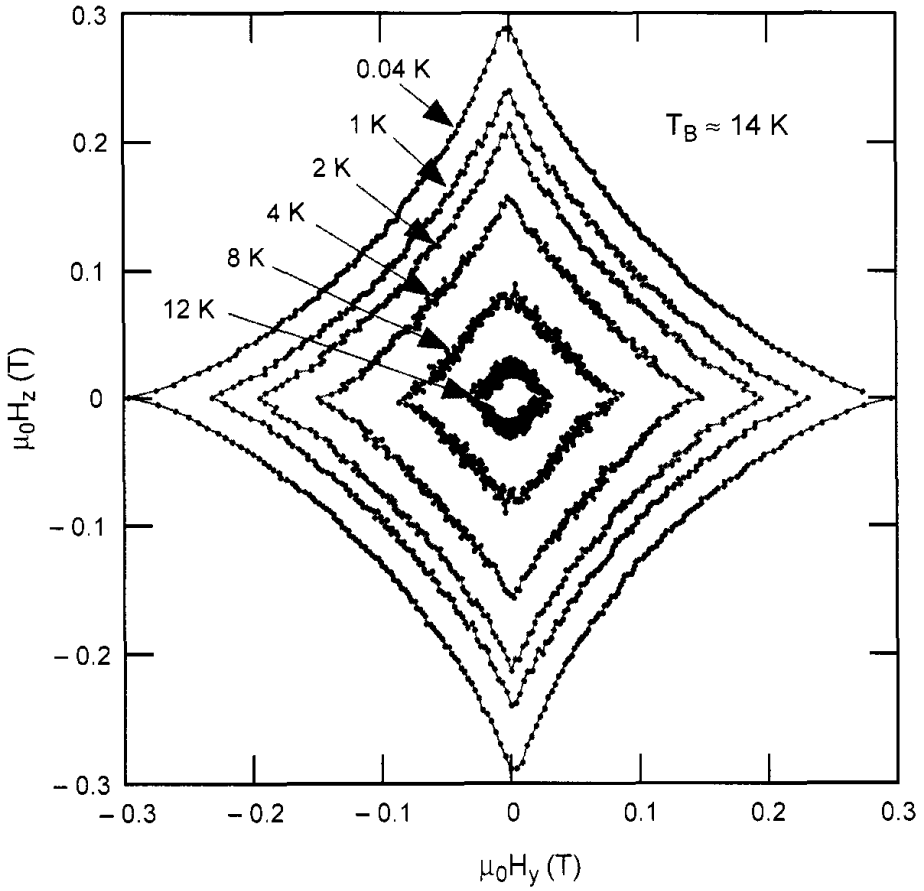

Figure 27. Temperature dependence of the switching field of a 3-nm Co cluster, measured in the plane defined by the easy and medium hard axes (H_y–H_z plane in Fig. 15). The data were recorded using the blind mode method (Section II.B.6) with a waiting time of the applied field of $\Delta t = 0.1$ s. The scattering of the data is due to stochastic and in good agreement with Eq. (4.10).

magnetization. T_B is defined as the temperature for which the waiting time Δt becomes equal to the relaxation time τ of the particle's magnetization at $\vec{H} = \vec{0}$. T_B can be used to estimate the total number N_{tot} of magnetic Co atoms in the cluster. Using an Arrhenius-like law [Eq. (4.7)] which can be written as $\Delta t = \tau = \tau_0 \exp(K_{at} N_{tot}/k_B T_B)$, where τ_0^{-1} is the attempt frequency typically between 10^{10} to 10^{11} Hz [102], K_{at} is an effective anisotropy energy per atom and k_B is the Boltzmann constant. Using the expression of the switching field at $T = 0$ K and for $\theta = 0$: $\mu_0 H_{sw} = 2K_{at}/\mu_{at} = 0.3\,T$ (Fig. 27), the atomic moment $\mu_{at} = 1.7\,\mu_B$, $\Delta t = 0.01$ s, $\tau_0 = 10^{-10}$ s, and $T_B = 14$ K, we deduce $N_{tot} \approx 1500$, which corresponds very well to a 3-nm Co cluster (Fig. 13).

Figure 28 presents a detailed measurement of the temperature dependence of the switching field at 0° and 45° and for three waiting times Δt. This measurement allows us to check the predictions of the field dependence of the barrier height. Equation (4.9) predicts that the mean switching field should be proportional to $T^{1/a}$ where a depends on the direction of the applied field [Eqs. (3.5) to (3.10)]: $a = 2$ for $\theta = 0°$ and 90°, and $a = 3/2$ for all other angles which are not too close to $\theta = 0°$ and 90°. We found a good agreement with this model (Fig. 29).

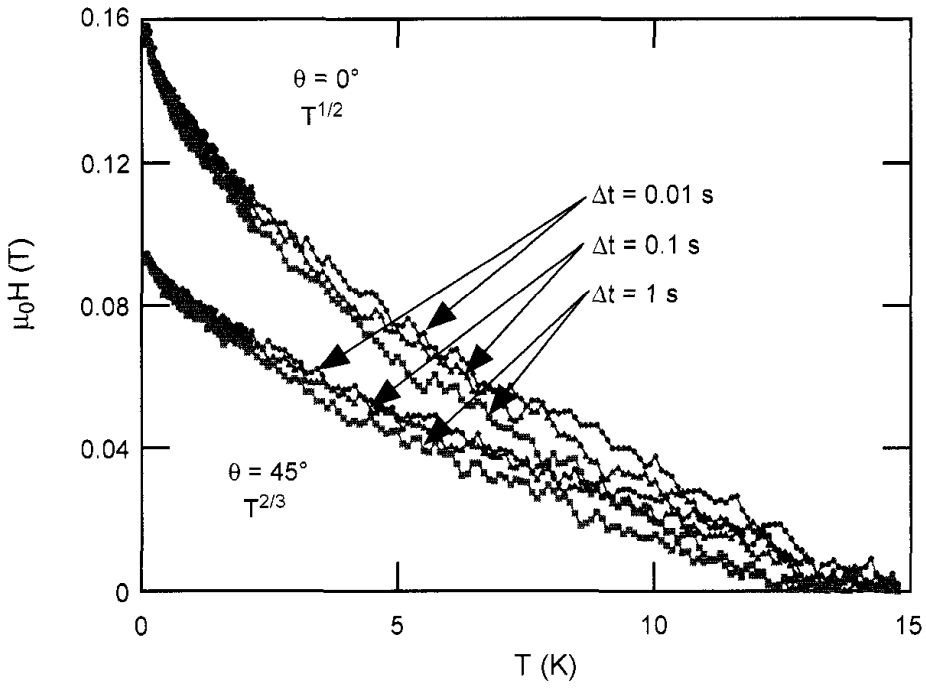

Figure 28. Temperature dependence of the switching field of a 3-nm Co cluster, measured at 0° and 45°. The data were recorded using the blind mode method (Section II.B.6) with different waiting time Δt of the applied field. The scattering of the data is due to stochastics and is in good agreement with Eq. (4.10).

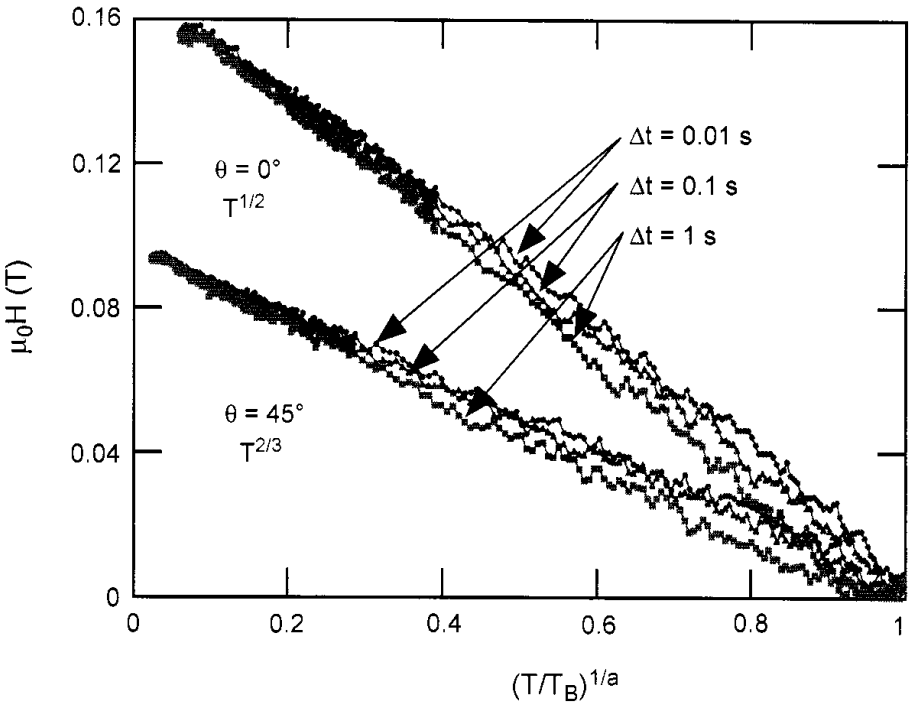

Figure 29. Temperature dependence of the switching field of a 3-nm Co cluster as in Fig. 28 but plotted as a function of $(T/T_B)^{1/a}$ with $T_B = 14$ K and $a = 2$ or 3/2 for $\theta = 0°$ and 45°, respectively, and for three waiting times Δt.

3. *Application to Ni Wires*

Electrodeposited wires (with diameters ranging from 40 to 100 nm and lengths up to 5000 nm; see Fig.1) were studied [35, 74] using the micro-SQUID technique (Section III.B.2). For diameter values under 50 nm, the switching probability as a function of time could be described by a single exponential function [Eq. (4.6)]. The mean waiting time τ followed an Arrhenius law [Eq. (4.7)] as proposed by the Néel–Brown model. Temperature and field sweeping rate dependence of the mean switching field could be described by the model of Kurkijärvi (Section IV.B.2) which is based on thermally assisted magnetization reversal over a simple potential barrier. These measurement allowed us to estimate an activation volume which was two orders of magnitude smaller than the wire volume. This confirmed the idea of the reversal of the magnetization caused by a nucleation of a reversed fraction of the cylinder, rapidly propagating along the whole sample. This result was also in good agreement with a micromagnetic model of Braun [77].

A pinning of the propagation of the magnetization reversal occurred for a few samples, where several jumps were observed in the hysteresis curves. The pinning of a domain wall was probably due to structure defects. The dynamic

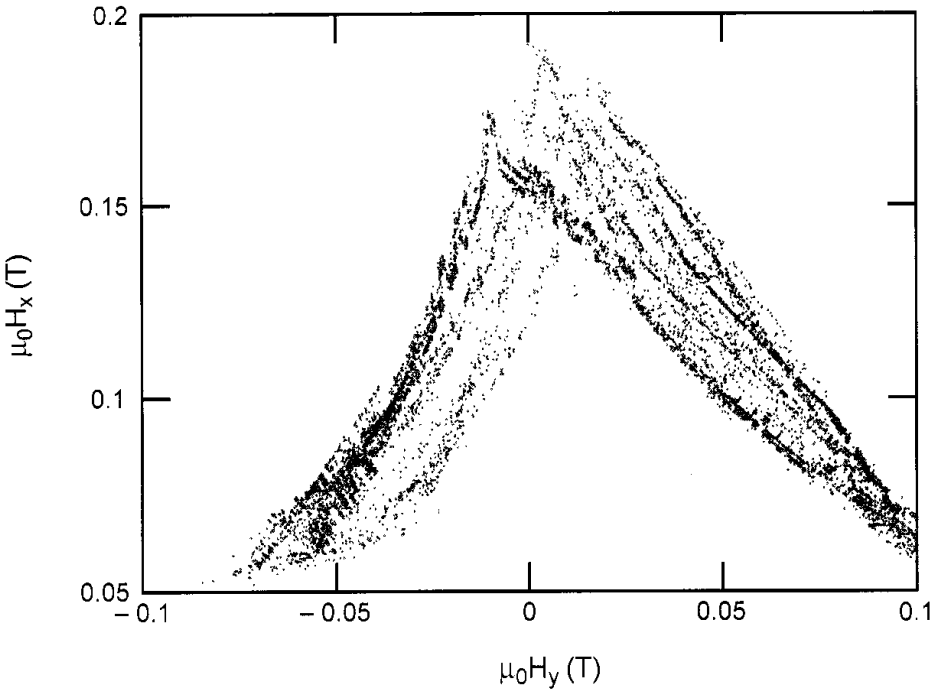

Figure 30. Angular dependence of switching fields of a 3-nm Fe cluster having (probably) a slightly oxidized surface. Each point corresponds to one of the 10,000 switching field measurements. The huge variations of the switching field might be due to exchange bias of frustrated spin configurations. However, quantum effects like those described in Section V are not completely excluded.

reversal properties of depinning were quite different from those of nucleation of a domain wall. For example, the probability of depinning as a function of time did not follow a single exponential law. A similar effect was also observed in single submicron Co particles having one domain wall [79], showing a domain wall annihilation process (Section III.B.3).

4. *Deviations From the Néel–Brown Model*

Anomalous magnetic properties of oxidized or ferrimagnetic nanoparticles have been reported previously by several authors [103, 104]. These properties are, for example, the lack of saturation in high fields and shifted hysteresis loops after cooling in the presence of a magnetic field. These behaviors have been attributed to uncompensated surface spins of the particles and surface spin disorder [105, 106].

Concerning our single-particle studies, we systematically observed aging effects which we attribute to an oxidation of the surface of the sample, forming antiferromagnetic CoO or NiO [59, 74]. We found that the antiferromagnetic coupling between the core of the particle or wire and its oxidized surface changed the dynamic reversal properties. For instance, we repeated the

measurements of the magnetization reversal of a Ni wire two days after fabrication, six weeks after, and finally after three months [74]. Between these measurements, the wire stayed in a dry box. The quasi-static micro-SQUID measurements did reveal only small changes. The saturation magnetization measured after six weeks was unchanged and was reduced by one to two percent after three months. The angular dependence of the switching field changed also only slightly. The dynamic measurements showed the aging effects more clearly, as evidenced by

- A nonexponential probability of not switching
- An increase of the width of the switching field distributions
- A decrease of the activation energy

We measured a similar behavior on lithographic fabricated Co particles with an oxidized border [59].

Figure 30 presents the angular dependence of switching fields of a 3-nm Fe cluster having a slightly oxidized surface. Huge variation of the switching fields can be observed which might be due to exchange bias of frustrated spin configurations at the surface of the cluster (Fig. 31).

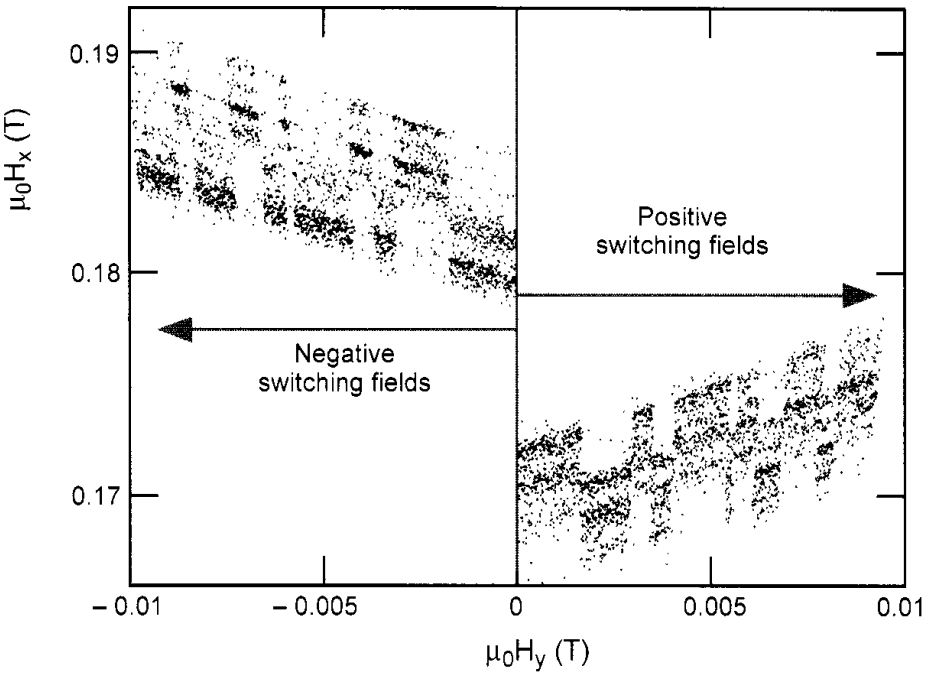

Figure 31. Details of the angular dependence of switching fields of a 3-nm Fe cluster having (probably) a slightly oxidized surface. Each point corresponds to one of the 3000 switching field measurements. Stochastic fluctuation between different switching field distributions are observed. The "mean" hysteresis loop is shifted to negative fields.

We propose that the magnetization reversal of a ferromagnetic particle with an antiferromagnetic surface layer is mainly governed by two mechanisms which are both due to spin frustration at the interface between the ferromagnetic core and the antiferromagnetic surface layer(s). The first mechanism may come from the spin frustration differing slightly from one cycle to another, thus producing a varying energy landscape. These energy variations are less important at high temperatures when the thermal energy ($k_B T$) is much larger. However, at lower temperature the magnetization reversal becomes sensitive to the energy variations. During the hysteresis loop the system chooses randomly a path through the energy landscape which leads to broad switching field distributions. A second mechanism may become dominant at high temperatures: the magnetization reversal may be governed by a relaxation of the spin frustration, hence by a relaxation of the energy barrier. This relaxation is thermally activated—that is, slower at lower temperatures.

V. MAGNETIZATION REVERSAL BY QUANTUM TUNNELING

Studying the boundary between classical and quantum physics has become a very attractive field of research which is known as "mesoscopic" physics (Fig. 1). New and fascinating mesoscopic effects can occur when characteristic system dimensions are smaller than the length over which the quantum wave function of a physical quantity remains sensitive to phase changes. Quantum interference effects in mesoscopic systems have, until now, involved phase interference between paths of particles moving in real space as in SQUIDs or mesoscopic rings. For magnetic systems, similar effects have been proposed for spins moving in spin space, such as magnetization tunneling out of a metastable potential well or coherent tunneling between classically degenerate directions of magnetization [107, 108].

We have seen in the previous sections that the intrinsic quantum character of the magnetic moment can be neglected for nanoparticles with dimensions of the order of the domain wall width δ and the exchange length λ—that is, particles with a collective spin of $S = 10^5$ or larger. However, recent measurements on molecular clusters with a collective spin of $S = 10$ suggest that quantum phenomena might be observed at larger system sizes with $S \gg 1$. Indeed, it has been predicted that macroscopic quantum tunneling of magnetization can be observed in magnetic systems with low dissipation. In this case, it is the tunneling of the magnetization vector of a single-domain particle through its anisotropy energy barrier or the tunneling of a domain wall through its pinning energy. These phenomena have been studied theoretically and experimentally [108].

The following sections review the most important results concerning the observed quantum phenomena in molecular clusters which are mesoscopic model systems to test quantum tunneling theories and the effects of the

environmental decoherence. Their understanding requires a knowledge of many physical phenomena, and they are therefore particularly interesting for fundamental studies. We then focus on magnetic quantum tunneling (MQT) studied in individual nanoparticles or nanowires. We concentrate on the necessary experimental conditions for MQT and review some experimental results which suggest that quantum effects might even be important in nanoparticles with $S = 10^5$ or larger.

A. Quantum Tunneling of Magnetization in Molecular Clusters

Magnetic molecular clusters are the final point in the series of smaller and smaller units from bulk matter to atoms. Up to now, they have been the most promising candidates for observing quantum phenomena because they have a well-defined structure with well-characterized spin ground state and magnetic anisotropy. These molecules can be regularly assembled in large crystals where all molecules often have the same orientation. Hence, macroscopic measurements can give direct access to single molecule properties. The most prominent examples are a dodecanuclear mixed-valence manganese-oxo cluster with acetate ligands, short Mn_{12} acetate [111], and an octanuclear iron(III) oxo-hydroxo cluster of formula $[Fe_8O_2(OH)_{12}(tacn)_6]^{8+}$ where tacn is a macrocyclic ligand, short Fe_8 (Fig. 32) [112]. Both systems have a spin ground state of $S = 10$ and an Ising-type magnetocrystalline anisotropy, which stabilizes the spin states with $m = \pm 10$ and generates an energy barrier for the reversal of the magnetization of about 67 K for Mn_{12} acetate and 25 K for Fe_8.

Thermally activated quantum tunneling of the magnetization has first been evidenced in both systems [113–116]. Theoretical discussion of this assumes that thermal processes (principally phonons) promote the molecules up to high levels with small quantum numbers $|m|$, not far below the top of the energy barrier, and the molecules then tunnel inelastically to the other side. Thus the transition is almost entirely accomplished via thermal transitions, and the characteristic relaxation time is strongly temperature-dependent. An alternative explication was also presented [117]. For Fe_8, however, the relaxation time becomes temperature-independent below 0.36 K [116, 118], showing that a pure tunneling mechanism between the only populated ground states $m = \pm S = \pm 10$ is responsible for the relaxation of the magnetization. On the other hand, in the Mn_{12} acetate system one sees temperature-independent relaxation only for strong applied fields and below about 0.6 K [119, 120]. During the last years, several new molecular magnets were presented (see, for instance, Refs. 121–124) which show also tunneling at low temperatures.

The following subsections review the most appealing results concerning the Fe_8 system which can be seen as an *ideal* "model molecule" to study quantum phenomena in magnetic nanostructures. We stress that the tunneling in large

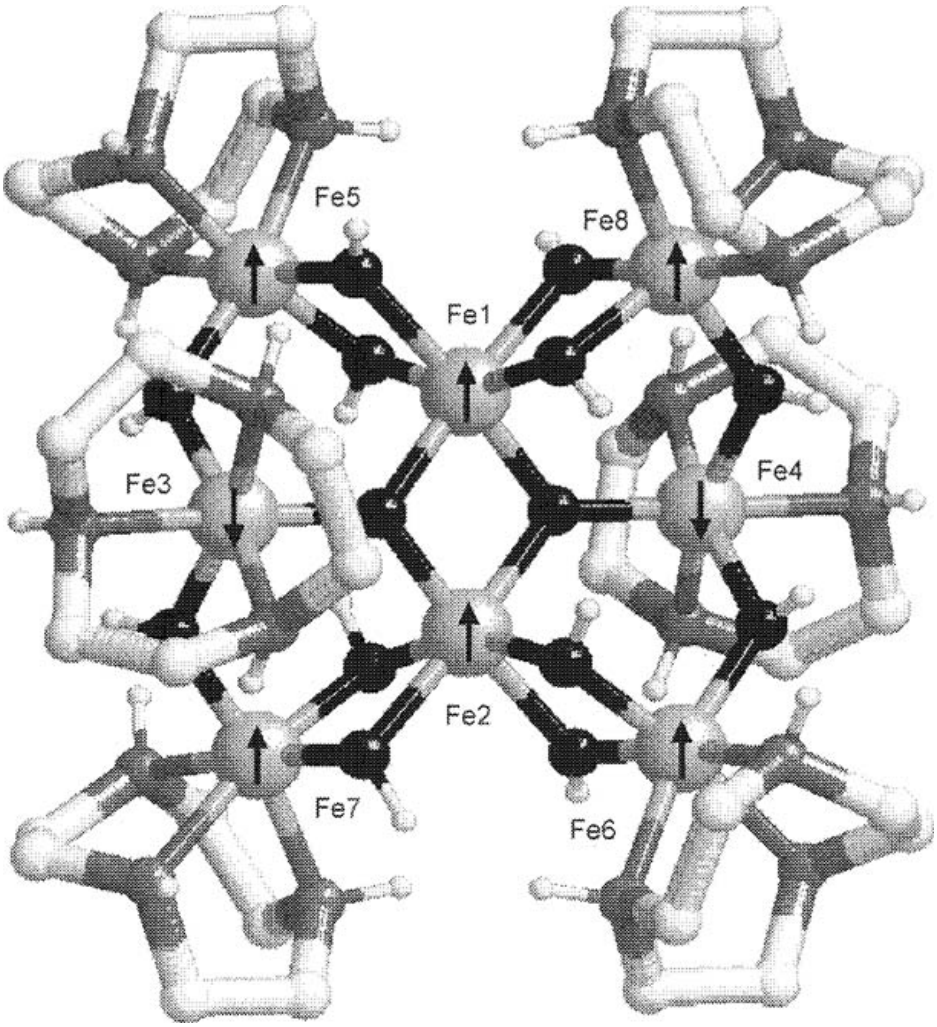

Figure 32. Schematic view of the magnetic core of the Fe_8 cluster. The oxygen atoms are black, the nitrogen atoms are gray, and carbon atoms are white. For the sake of clarity, only the hydrogen atoms that are exchanged with deuterium are shown as small spheres (Section V.B.4). The arrows represent the spin structure of the ground state $S = 10$ as experimentally determined through polarized neutron diffraction experiments [109]. The exact orientation of easy, medium, and hard axis of magnetization (Fig. 33) can be found in Ref. 110.

spins is remarkable because it does not show up at the lowest orders of perturbation theory.

All measurements on Fe_8 were performed using an array of micro-SQUIDs (Section II.B.7). The high sensitivity of this magnetometer allows us to study single Fe_8 crystals [125] of sizes of the order of 10 to 500 μm. For ac-susceptibility measurements and magnetization measurements at $T > 6$ K, we used a home-built Hall probe magnetometer [26, 126]. It works in the temperature range between 0.03 K and 100 K, for frequencies between 1 Hz and 100 kHz.

After discussing the magnetic anisotropy of Fe_8, we present the observed quantum phenomena. The discussions of the following sections neglect environmental decoherence effects for the sake of simplicity. In Section V.2, we focus on effects of the environment (dipolar coupling, nuclear spins, and temperature) onto the tunneling. This review should help to set up a complete theory which describes *real* magnetic quantum systems.

1. Magnetic Anisotropy in Fe_8

The octanuclear iron(III) oxo-hydroxo cluster of formula $[Fe_8O_2(OH)_{12}(tacn)_6]^{8+}$ where tacn is a macrocyclic ligand, short Fe_8 (Fig. 32), was first synthesized by Wieghardt et al. in 1984 [125]. Four central iron (III) ions with $S = 5/2$ are bridged by two oxo groups. The other four iron (III) ions are bridged by hydroxo groups to the central iron ions in an almost planar arrangement, as shown in Fig. 32. The clusters have approximate D_2 symmetry but crystallize in the triclinic system [110].

Fe_8 has an $S = 10$ ground state that originates from antiferromagnetic interactions that do not give complete compensation of the magnetic moment [127]. Spin–orbital moments can be neglected because the magnetic ions are in an "orbital singlet" as a result of Hund's rules. The spin structure of the ground state schematized by the arrows in Fig. 32 has been recently confirmed by a single-crystal polarized neutron investigation that provided a magnetization density map of the cluster [109].

The simplest model describing the spin system of Fe_8 molecular clusters (called the giant spin model) has the following Hamiltonian [112]:

$$H = -DS_z^2 + E(S_x^2 - S_y^2) + g\mu_B\mu_0\vec{S}\cdot\vec{H} \tag{5.1}$$

S_x, S_y, and S_z are the three components of the spin operator, D and E are the anisotropy constants which were determined via HF-EPR ($D/k_B \approx 0.275\,K$ and $E/k_B \approx 0.046\,K$ [112]), and the last term of the Hamiltonian describes the Zeeman energy associated with an applied field $\vec{H}$. This Hamiltonian defines hard, medium, and easy axes of magnetization in x, y, and z directions, respectively (Fig. 33). It has an energy level spectrum with $(2S+1) = 21$ values which, to a first approximation, can be labeled by the quantum numbers $m = -10, -9, \ldots, 10$ choosing the z-axis as quantization axis. The energy spectrum, shown in Fig. 34, can be obtained by using standard diagonalisation techniques of the $[21 \times 21]$ matrix describing the spin Hamiltonian $S = 10$. At $\vec{H} = 0$, the levels $m = \pm 10$ have the lowest energy. When a field H_z is applied, the energy levels with $m < -2$ increase, while those with $m > 2$ decrease (Fig. 34). Therefore, energy levels of positive and negative quantum numbers cross at certain fields H_z. It turns out that for Fe_8 the levels cross at fields given by $\mu_0 H_z \approx$

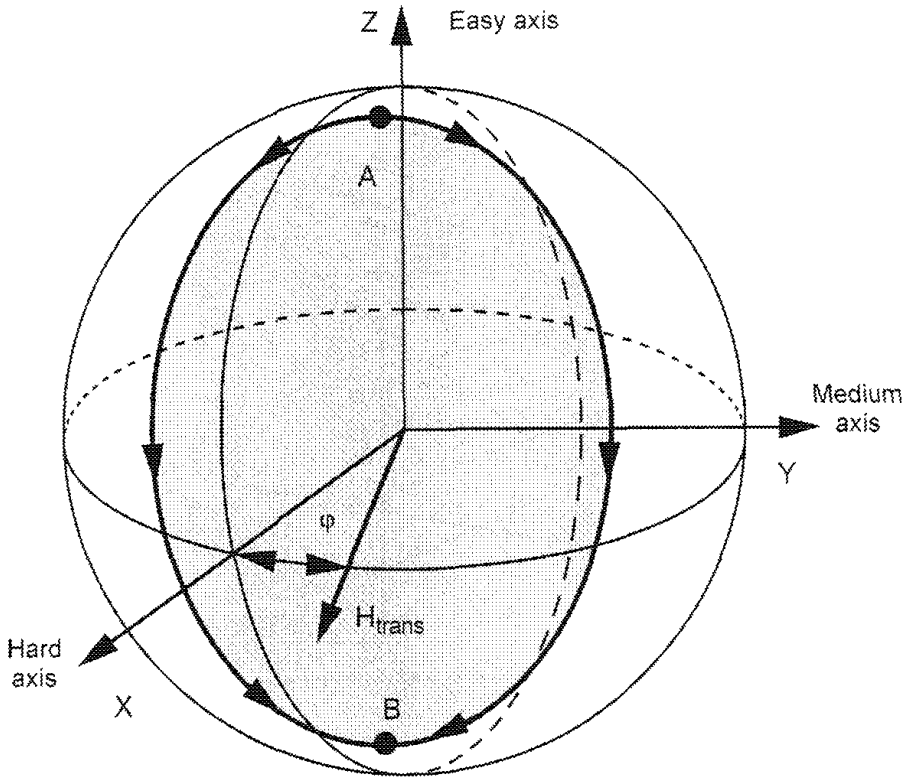

Figure 33. Unit sphere showing degenerate minima **A** and **B** which are joined by two tunnel paths (heavy lines). The hard, medium, and easy axes are taken in x-, y-, and z-direction, respectively. The constant transverse field H_{trans} for tunnel splitting measurements is applied in the xy-plane at an azimuth angle φ. At zero applied field $\vec{H} = 0$, the giant spin reversal results from the interference of two quantum spin paths of opposite direction in the easy anisotropy yz-plane. For transverse fields in direction of the hard axis, the two quantum spin paths are in a plane which is parallel to the yz-plane, as indicated in the figure. By using Stokes' theorem it has been shown [128] that the path integrals can be converted in an area integral, yielding–that destructive interference—that is, a quench of the tunneling rate—occurs whenever the shaded area is $k\,\pi/S$, where k is an odd integer. The interference effects disappear quickly when the transverse field has a component in the y-direction because the tunneling is then dominated by only one quantum spin path.

$n \times 0.22\,\mathrm{T}$, with $n = 1, 2, 3\ldots$. The inset of Fig. 34 displays the details at a level crossing where transverse terms containing S_x or S_y spin operators turn the crossing into an "avoided level crossing." The spin S is "in resonance" between two states when the local longitudinal field is close to an avoided level crossing. The energy gap, the so-called "tunnel spitting" Δ, can be tuned by an applied field in the xy-plane (Fig. 33) via the S_xH_x and S_yH_y Zeeman terms (Section V.A.3).

The effect of these avoided level crossings can be seen in hysteresis loop measurements (Fig. 35). When the applied field is near an avoided level crossing, the magnetization relaxes faster, yielding steps separated by plateaus. As the

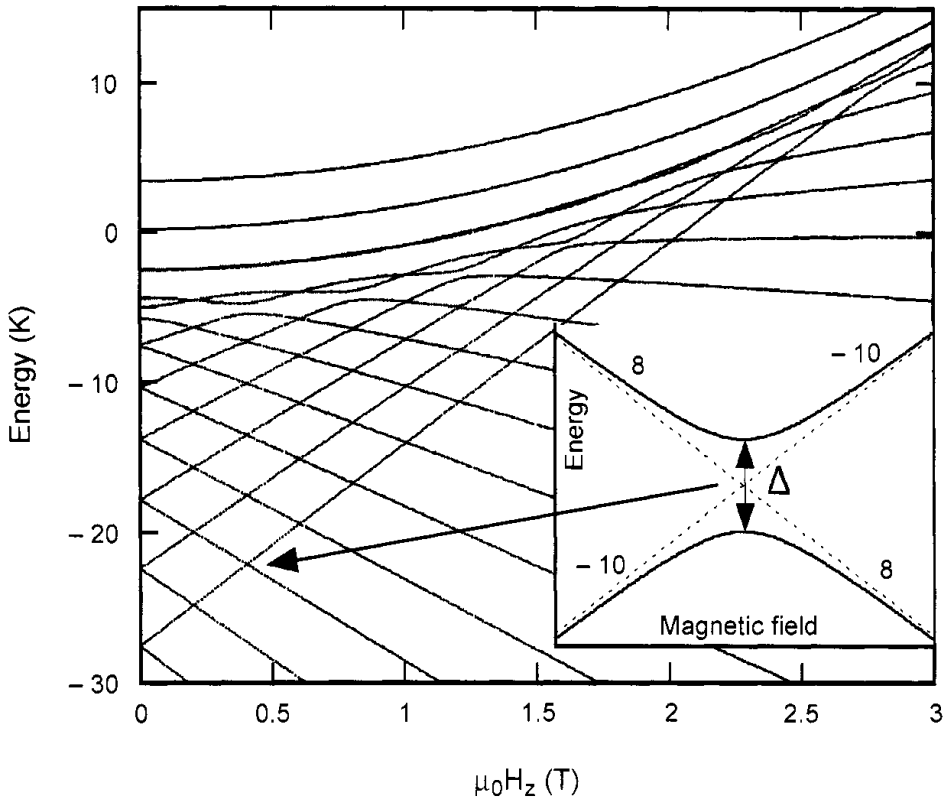

Figure 34. Zeeman diagram of the 21 levels of the $S = 10$ manifold of Fe_8 as a function of the field applied along the easy axis [Eq. (5.1)]. From bottom to top, the levels are labeled with quantum numbers $m = \pm 10, \pm 9, \ldots, 0$. The levels cross at fields given by $\mu_0 H_z \approx n \times 0.22\,\mathrm{T}$, with $n = 1, 2, 3, \ldots$. The *inset* displays the detail at a level crossing where the transverse terms (terms containing S_x or/and S_y spin operators) turn the crossing into an avoided level crossing. The greater the tunnel splitting Δ, the higher the tunnel rate.

temperature is lowered, there is a decrease in the transition rate due to reduced thermal-assisted tunneling. A similar behavior was observed in Mn_{12} acetate clusters [113–115] where equally separated steps were observed at $H_z \approx n \times 0.45\,\mathrm{T}$. The main difference between both clusters is that the hysteresis loops of Fe_8 become temperature-independent below 0.36 K whereas measurements on Mn_{12} acetate indicate a temperature independence only for strong applied fields and below 0.6 K [119–120].

Another important difference is that the step heights (i.e., the relaxation rates) change periodically when a constant transverse field is applied (Fig. 36). It is the purpose of the next subsections to present a detailed study of this behavior.

2. *Landau–Zener Tunneling in Fe_8*

The nonadiabatic transition between the two states in a two-level system has first been discussed by Landau, Zener, and Stückelberg [130–132]. The original work

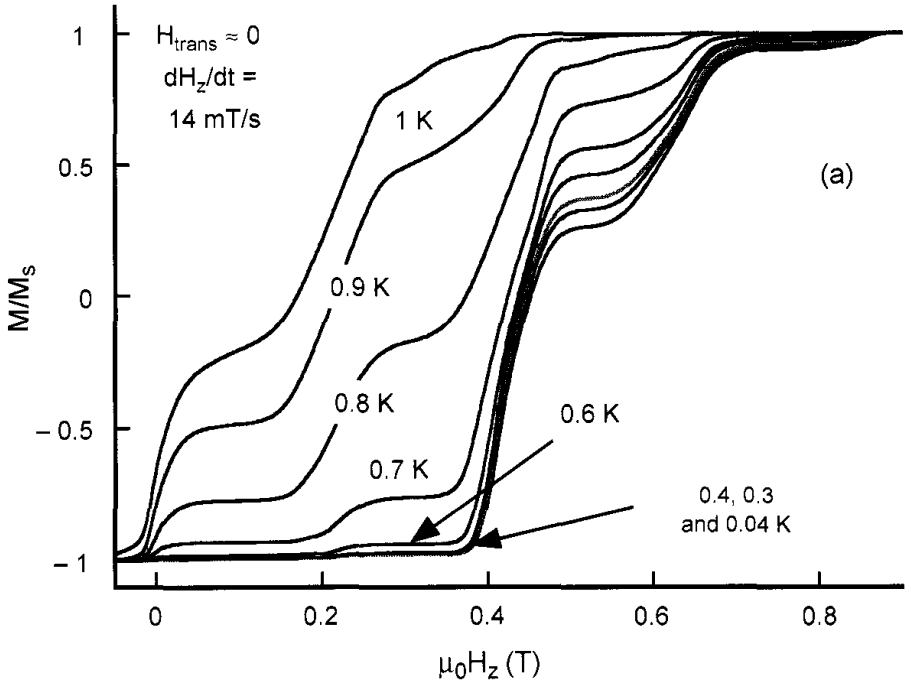

Figure 35. Hysteresis loops of a single crystal of Fe_8 molecular clusters: (a) at different temperatures and a constant sweeping rate $dH_z/dt = 0.014$ T/s and (b) at 0.04 K and different field sweeping rates. The loops display a series of steps, separated by plateaus. As the temperature is lowered, there is a decrease in the transition rate due to reduced thermal assisted tunneling. The hysteresis loops become temperature-independent below 0.35 K, demonstrating quantum tunneling at the lowest energy levels. The resonance widths at small fields H_z of about 0.05 T are mainly due to dipolar fields between the molecular clusters [118, 129].

by Zener concentrates on the electronic states of a biatomic molecule, while Landau and Stückelberg considered two atoms that undergo a scattering process. Their solution of the time-dependent Schrödinger equation of a two-level system could be applied to many physical systems and it became an important tool for studying tunneling transitions. The Landau–Zener model has also been applied to spin tunneling in nanoparticles and clusters [133–138]. The tunneling probability P when sweeping the longitudinal field H_z at a constant rate over an avoided energy level crossing (Fig. 37) is given by

$$P_{m,m'} = 1 - \exp\left[-\frac{\pi \Delta_{m,m'}^2}{2\hbar g \mu_B |m - m'| \mu_0 dH_z/dt} \right] \tag{5.2}$$

Here, m and m' are the quantum numbers of the avoided level crossing, dH_z/dt is the constant field sweeping rates, $g \approx 2$, μ_B the Bohr magneton, and $\hbar$ is Planck's constant.

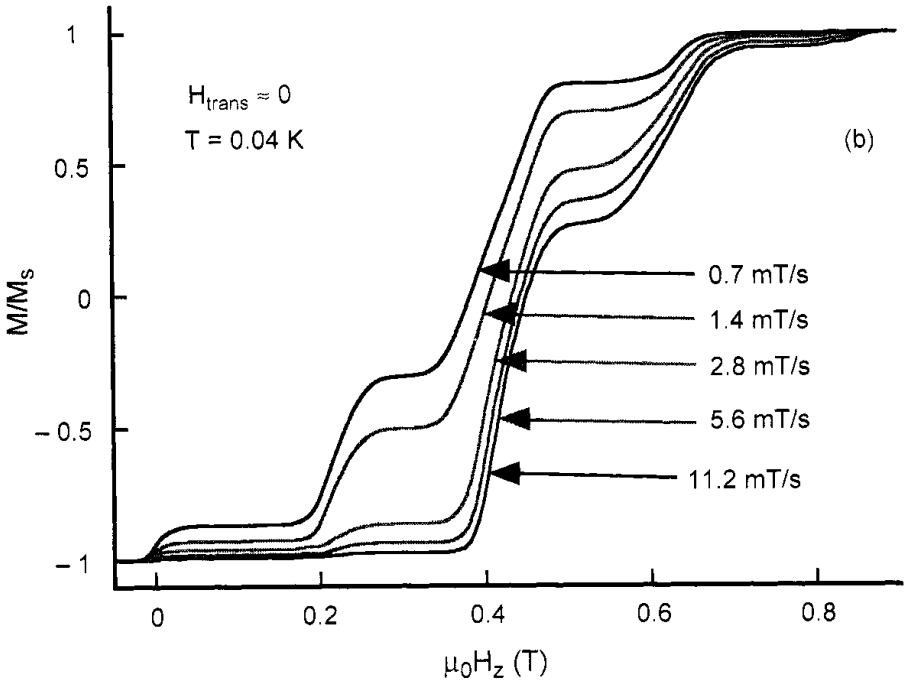

Figure 35. *(Continued).*

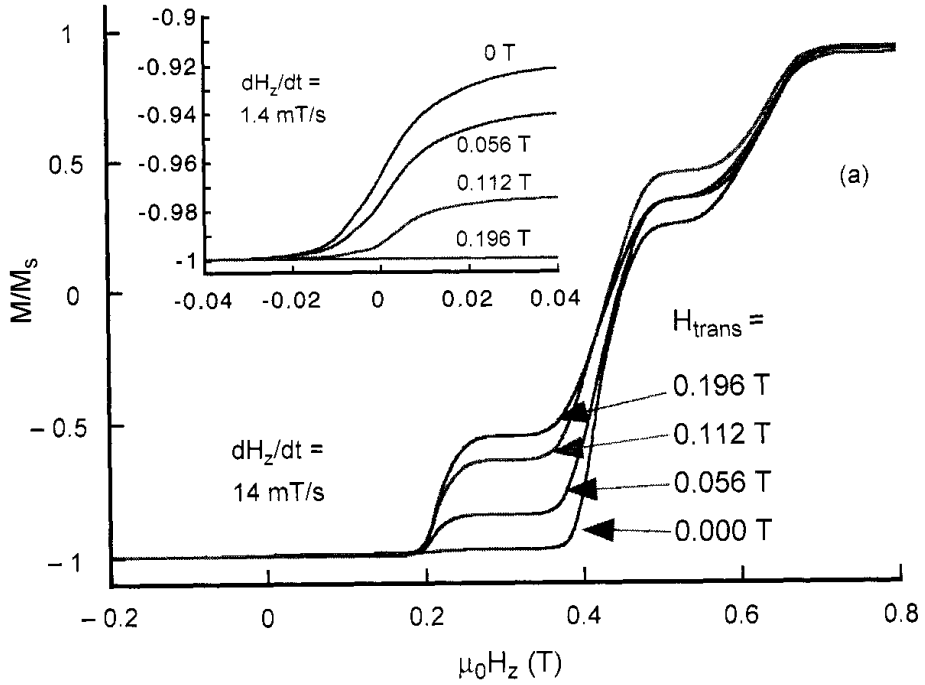

Figure 36. Hysteresis loops measured along H_z in the presence of a constant transverse field at 0.04 K. *Insets*: Enlargement around the field $H_z = 0$. Notice that the sweeping rate is ten times slower for the measurements in the insets than that of the main figures.

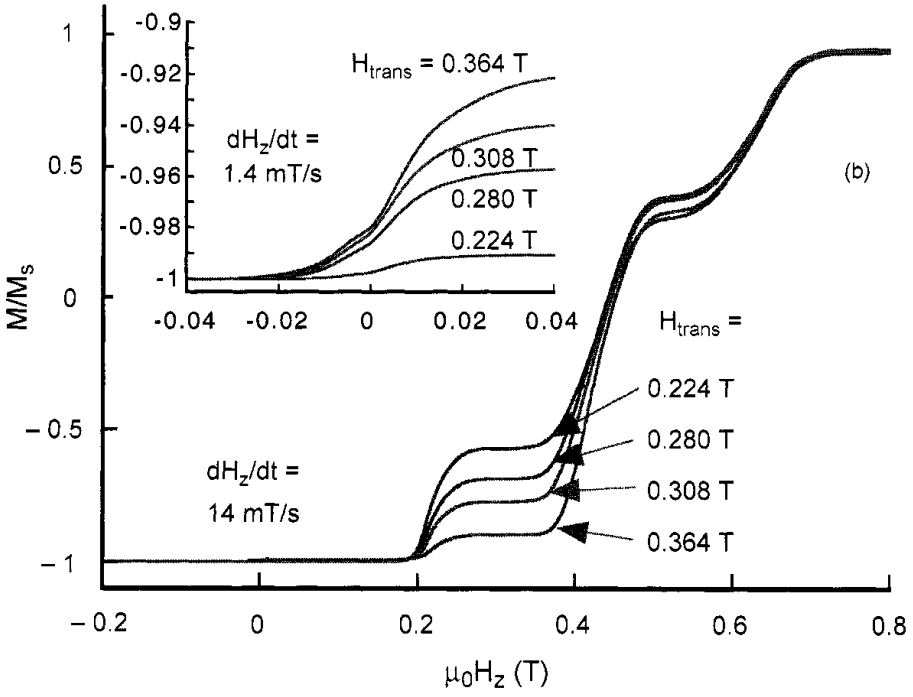

Figure 36. *(Continued).*

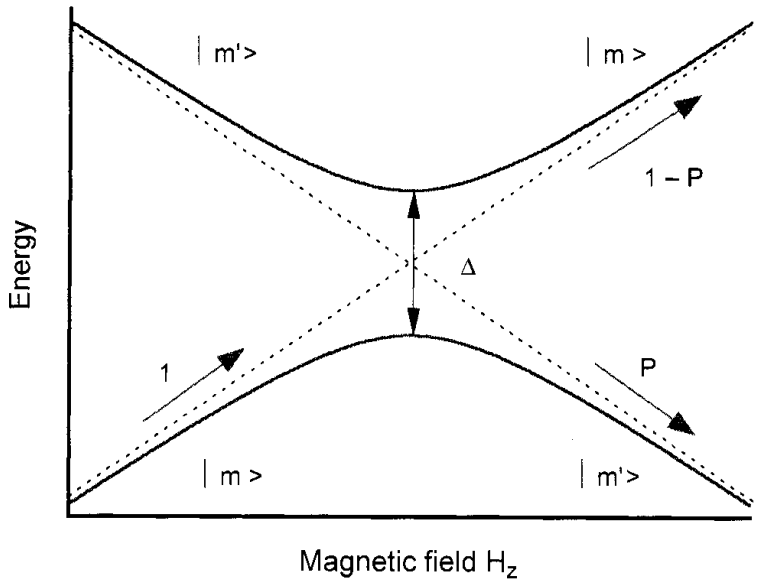

Figure 37. Detail of the energy level diagram near an avoided level crosssing. m and m' are the quantum numbers of the energy level. $P_{m,m'}$ is the Landau–Zener tunnel probability when sweeping the applied field from the left to the right over the anticrossing. The greater the gap Δ and the slower the sweeping rate, the higher is the tunnel rate [Eq. (5.2)].

With the Landau–Zener model in mind, we can now start to understand qualitatively the hysteresis loops (Fig. 35). Let us start at a large negative magnetic field H_z. At very low temperature, all molecules are in the $m=-10$ ground state. When the applied field H_z is ramped down to zero, all molecules will stay in the $m=-10$ ground state. When ramping the field over the $\Delta_{-10,10}$-region at $H_z \approx 0$, there is a Landau–Zener tunnel probability $P_{-10,10}$ to tunnel from the $m=-10$ to the $m=10$ state. $P_{-10,10}$ depends on the sweeping rate [Eq. (5.2)]; that is, the slower the sweeping rate, the larger the value of $P_{-10,10}$. This is clearly demonstrated in the hysteresis loop measurements showing larger steps for slower sweeping rates (Fig. 35). When the field H_z is now further increased, there is a remaining fraction of molecules in the $m=-10$ state which became a metastable state. The next chance to escape from this state is when the field reaches the $\Delta_{-10,9}$ region. There is a Landau–Zener tunnel probability $P_{-10,9}$ to tunnel from the $m=-10$ to the $m=9$ state. As $m=9$ is an excited state, the molecules in this state desexcite quickly to the $m=10$ state by emitting a phonon. An analogous procedure happens when the applied field reaches the $\Delta_{-10,10-n}$-regions ($n=2, 3, \ldots$) until all molecules are in the $m=10$ ground state; that is, the magnetization of all molecules is reversed. As phonon emission can only change the molecule state by $\Delta m = 1$ or 2, there is a phonon cascade for higher applied fields.*

In order to apply quantitatively the Landau–Zener formula [Eq. (5.2)], we first saturated the crystal of Fe_8 clusters in a field of $H_z=-1.4\,T$, yielding an initial magnetization $M_{in}=-M_s$.† Then, we swept the applied field at a constant rate over one of the resonance transitions and measured the fraction of molecules which reversed their spin. This procedure yields the tunneling rate $P_{-10,10-n}$ and thus the tunnel splitting $\Delta_{-10,10-n}$ [Eq. (5.2)] with $n=0, 1, 2, \ldots$.

For very small tunneling probabilities $P_{-10,10-n}$, we did multiple sweeps over the resonance transition. The magnetization M after N sweeps is given by

$$M(N) \approx M_{eq} + (M_{in} - M_{eq})e^{-kP_{-10,10-n}N} = M_{eq} + (M_{in} - M_{eq})e^{-\Gamma t} \qquad (5.3)$$

Here M_{in} is the initial magnetization, $M_{eq}(H_z)$ is the equilibrium magnetization, $N=(1/A)(dH_z/dt)t$ is the number of sweeps over the level crossing, $\Gamma = kP_{-10,10-n}\ (1/A)(dH_z/dt)$ is the overall Landau–Zener transition rate, $k=2$ for $n=0$ and $k=1$ for $n=1, 2, \ldots$, and A is the amplitude of the ramp-field.‡ We have therefore a simple tool to obtain the tunnel splitting by measuring $P_{-10,10-n}$,

*Phonon-induced transitions with $|\Delta m|>2$ are very small [139–141].

†In order to avoid heating problems for measurements of Δ for $n>1$, we started in a thermally annealed sample with $M_{in}=0.95\,M_s$ instead of $M_{in}=-M_s$ or $M_{in}=0$.

‡We supposed here that the forth and back sweeps give the same tunnel probability. This is a good approximation for $P \ll 1$ where next-nearest-neighbor (molecule) effects can be neglected.

or $M(N)$ for $P_{-10,10-n} \ll 1$. We first checked the predicted Landau–Zener sweeping field dependence of the tunneling rate. This can be done, for example, by plotting the relaxation of magnetization as a function of $t = N\ (A/dH_z/dt)$. The Landau–Zener model predicts that all measurements should fall on one curve which was indeed the case for sweeping rates between 1 and 0.001 T/s (Fig. 38) for the $m = \pm 10$ transition. The deviations at lower sweeping rates are mainly due to the *hole-digging mechanism* [129] which slows down the relaxation (see Section V.B.2).* In the ideal case, we should find an exponential curve [Eq. (5.3)]. However, we found clear deviations from the exponential curve (Fig. 39), which might be due to molecules with different amounts of nuclear spins. For example, two percent of natural iron has a nuclear spin; that is, about 10 percent of Fe_8 has at least one nuclear spin on the iron. This interpretation is supported by measurements on isotopically substituted Fe_8 samples (Fig. 39).

Another way of checking the Landau–Zener sweeping field dependence of the tunneling rate is presented in Fig. 40 showing a sweeping rate independent

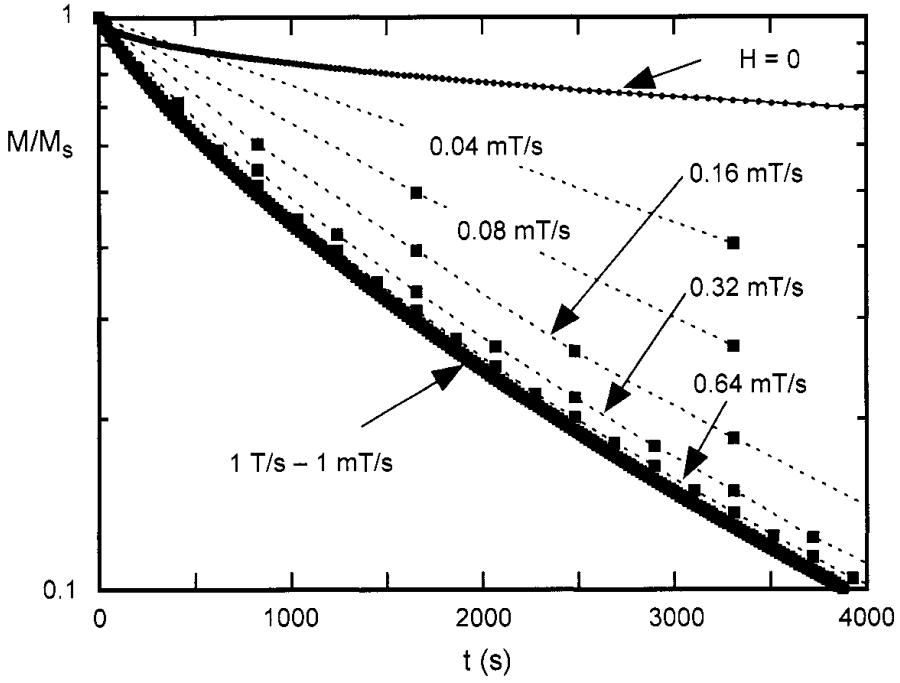

Figure 38. Scaling plot for the Landau–Zener method showing the predicted field sweeping rate dependence for 1 T/s to 1 mT/s. Each point indicates the magnetization after a field sweep over the $m = \pm 10$ resonance. The dotted lines are guides for the eyes. For comparison, the figure displays also a relaxation curve at a constant field $\vec{H} = 0$ (Fig. 36) which shows much slower relaxation [129].

*Roughly speaking, at very low field sweeping rates internal fields change faster than the external field.

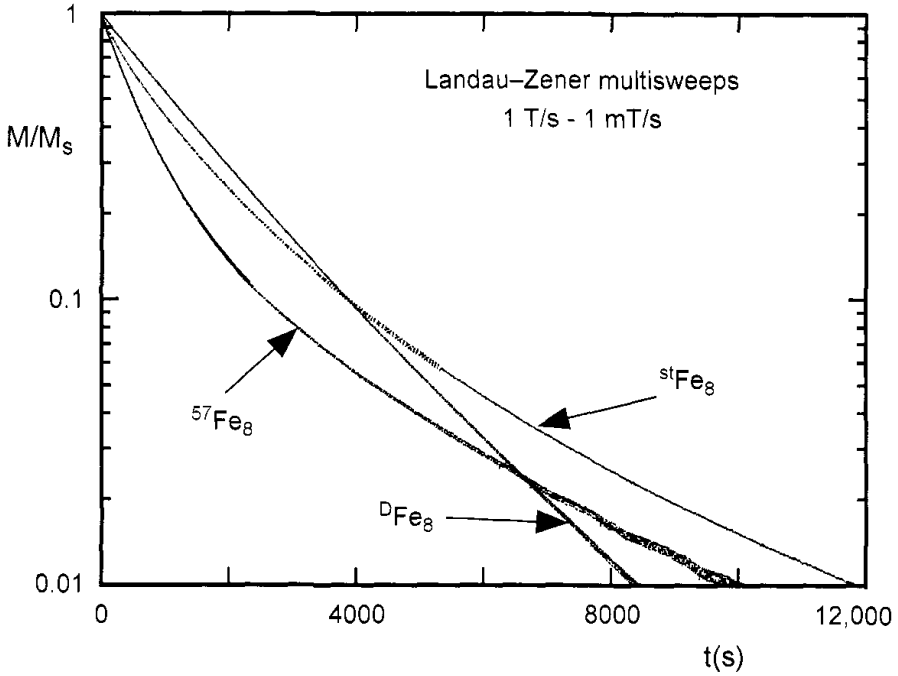

Figure 39. Scaling plot for the Landau–Zener method showing the predicted field sweeping rate dependence for 1 T/s to 1 mT/s similar to Fig. 38 but for three isotopically substituted Fe_8 samples. Further details are presented in Section V.B.4.

$\Delta_{-10,10}$ between 1 and 0.001 T/s.* The measurements on isotopically substituted Fe_8 samples show a small dependence of $\Delta_{m,m'}$ on the hyperfine coupling (Fig. 40). Such an effect has been predicted for a constant applied field by Tupitsyn et al. [142], and for a ramped field by Rose [136]. Further details are presented in Section V.B.4.

We also compared the tunneling rates found by the Landau–Zener method with those found using a square-root decay method that was proposed by Prokof'ev and Stamp [143], and we found a good agreement [129, 144] (Section V. B.1).

Our measurements showed for the first time that the Landau–Zener method is particularly adapted for molecular clusters because it works even in the presence of dipolar fields that spread the resonance transition provided that the field sweeping rate is not too small. Furthermore, our measurements show a small but clear influence of the hyperfine coupling which should be included in a generalized Landau–Zener model [136].

3. *Oscillations of Tunnel Splitting*

An applied field in the xy-plane can tune the tunnel splittings $\Delta_{m,m'}$ via the S_x and S_y spin operators of the Zeeman terms that do not commute with the spin

*Recent measurements confirmed the good agreement up to 30 T/s.

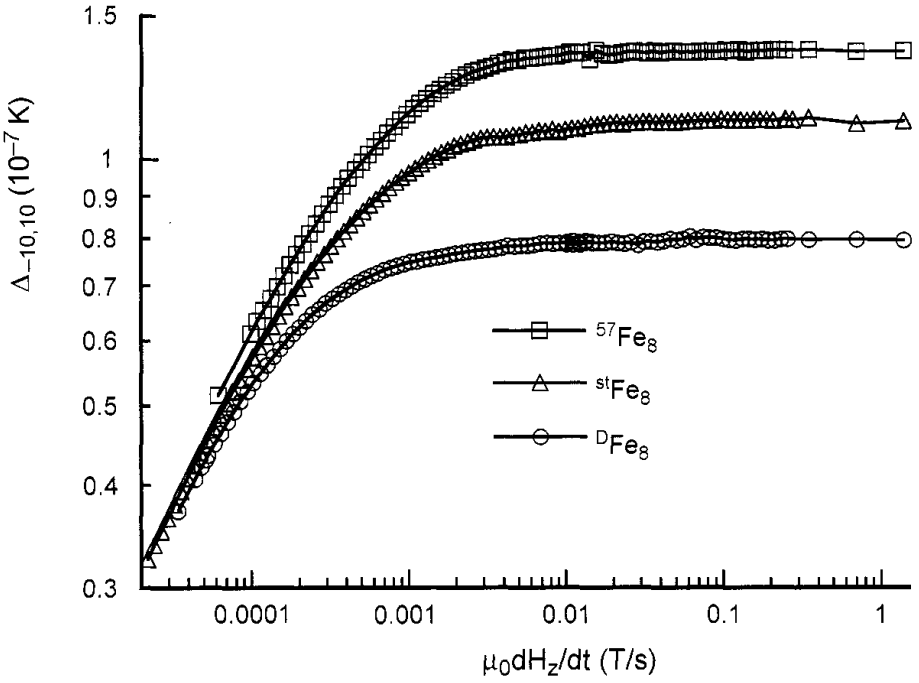

Figure 40. Field sweeping rate dependence of the tunnel splitting $\Delta_{-10,10}$ measured by a Landau–Zener method for three Fe_8 samples, for $H_x = 0$. The Landau–Zener method works in the region of high sweeping rates where $\Delta_{-10,10}$ is sweeping rate independent. Note that the differences of $\Delta_{-10,10}$ between the three isotopically substituted samples are rather small in comparison to the oscillations in Fig. 41.

Hamiltonian. This effect can be demonstrated by using the Landau–Zener method (Section V.A.2). Figure 41 presents a detailed study of the tunnel splitting $\Delta_{\pm 10}$ at the tunnel transition between $m = \pm 10$, as a function of transverse fields applied at different angles φ, defined as the azimuth angle between the anisotropy hard axis and the transverse field (Fig. 42). For small angles φ the tunneling rate oscillates with a period of ~ 0.4 T, whereas no oscillations showed up for large angles φ [47]. In the latter case, a much stronger increase of $\Delta_{\pm 10}$ with transverse field is observed. The transverse field dependence of the tunneling rate for different resonance conditions between the state $m = -10$ and $(10-n)$ can be observed by sweeping the longitudinal field around $\mu_0 H_z = n \times 0.22$ T with $n = 0, 1, 2, \ldots$. The corresponding tunnel splittings $\Delta_{-10,10-n}$ oscillate with almost the same period of ~ 0.4 T (Fig. 41). In addition, comparing quantum transitions between $m = -10$ and $(10-n)$, with n even or odd, revealed a parity (or symmetry) effect that is analogous to the Kramers' suppression of tunneling predicted for half-integer spins [145, 146]. This behavior has been observed for $n = 0$ to 4.* A similar strong dependence on the azimuth angle φ was observed for all the resonances.

*The tunneling rate were too fast for $n>4$.

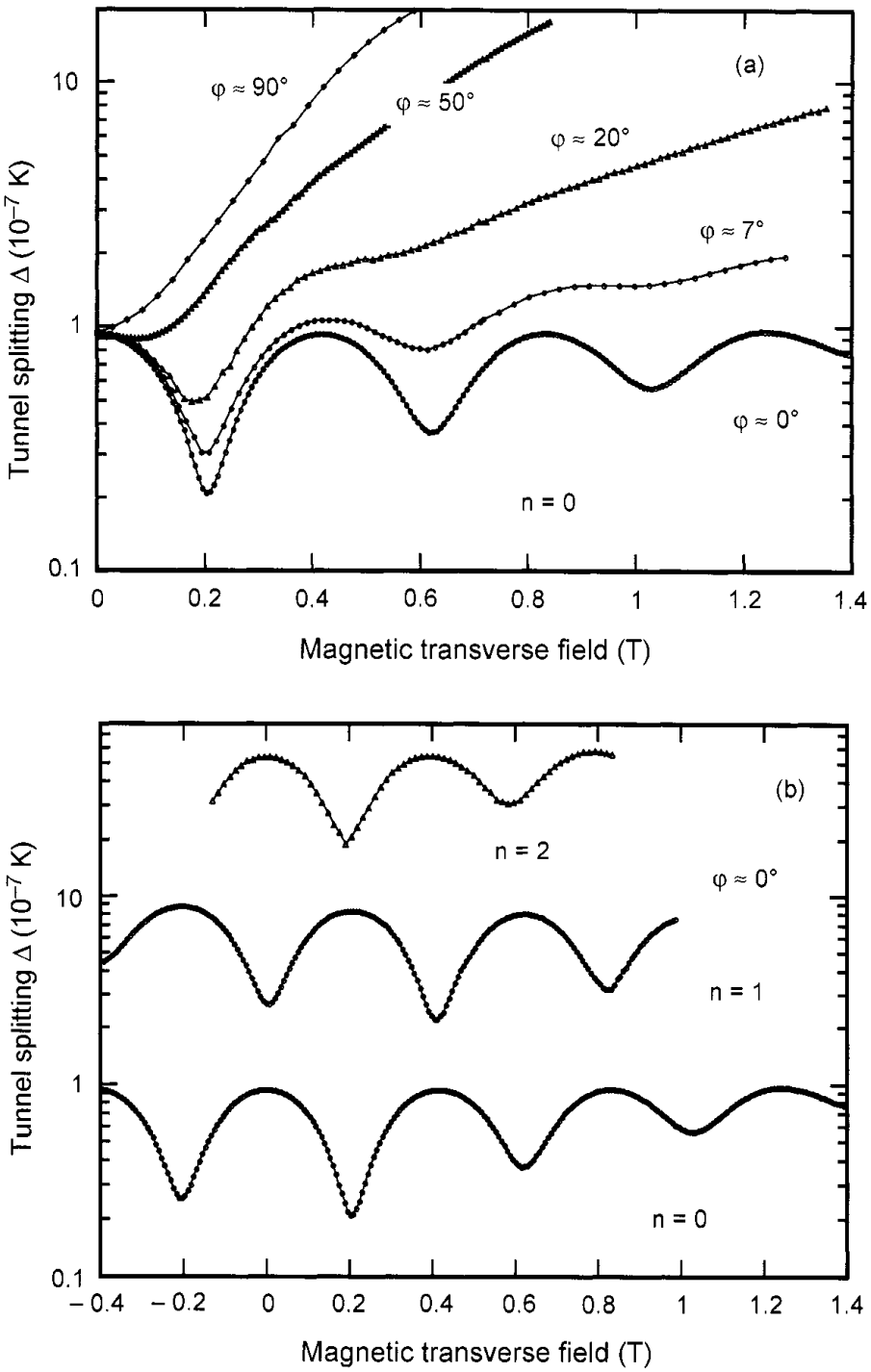

Figure 41. Measured tunnel splitting Δ as a function of transverse field for (a) several azimuth angles φ at $m = \pm 10$ and (b) $\varphi \approx 0°$, as well as for quantum transition between $m = -10$ and $(10-n)$. Note the parity effect that is analogous to the suppression of tunneling predicted for half-integer spins. It should also be mentioned that internal dipolar and hyperfine fields hinder a quench of Δ which is predicted for an isolated spin (Figs. 42 and 45).

a. Semiclassical Descriptions. Before showing that the above results can be derived by an exact numerical calculation using the quantum operator formalism, it is useful to discuss semiclassical models. The original prediction of oscillation of the tunnel splitting was done by using the path integral formalism [147]. Here [128], the oscillations are explained by constructive or destructive interference of quantum spin phases (Berry phases) of two tunnel paths (instanton trajectories) (Fig. 33). Since our experiments were reported, the Wentzel–Kramers–Brillouin theory has been used independently by Garg [148] and Villain and Fort [149]. The surprise is that although these models [128, 148, 149] are derived semiclassically, and should have higher-order corrections in $1/S$, they appear to be exact as written! This has first been noted in Refs. 148 and 149 and then proven in Ref. 150. Some extensions or alternative explications of Garg's result can be found in Refs. 151–154.
The period of oscillation is given by [128]

$$\Delta H = \frac{2k_B}{g\mu_B}\sqrt{2E(E+D)} \tag{5.4}$$

where D and E are defined in Eq. (5.1). We find a period of oscillation of $\Delta H = 0.26\,\mathrm{T}$ for $D = 0.275\,\mathrm{K}$ and $E = 0.046\,\mathrm{K}$ as in Ref. 112. This is somewhat smaller than the experimental value of $\sim 0.4\,\mathrm{T}$. We believe that this is due to higher-order terms of the spin Hamiltonian which are neglected in Garg's calculation. These terms can easily be included in the operator formalism as shown in the next subsection.

b. Exact Numerical Diagonalization. In order to quantitatively reproduce the observed periodicity we included fourth-order terms in the spin Hamiltonian [Eq. (5.1)] as recently employed in the simulation of inelastic neutron scattering measurements [155, 156] and performed a diagonalization of the [21 × 21] matrix describing the $S = 10$ system. For the calculation of the tunnel splitting we used $D = 0.289\,\mathrm{K}$, $E = 0.055\,\mathrm{K}$ [Eq. (5.1)] and the fourth-order terms as defined in [155] with $B_4^0 = 0.72 \times 10^{-6}\,\mathrm{K}$, $B_4^2 = 1.01 \times 10^{-5}\,\mathrm{K}$, $B_4^4 = -0.43 \times 10^{-4}\,\mathrm{K}$, which are close to the values obtained by EPR measurements [110] and neutron scattering measurements [156]. The calculated tunnel splittings for the states involved in the tunneling process at the resonances $n = 0$, 1, and 2 are reported in Figure 42, showing the oscillations as well as the parity effect for odd resonances. The calculated tunneling splitting is, however, ~1.5 times smaller than the observed one. This small discrepancy could be reduced by introducing higher-order terms. We believe that this is not relevant because the above model neglects, for example, the influence of nuclear spins which seems to increase the measured (effective) tunnel splittings (Fig. 40 and Section V.B.4). Our choice of the fourth-order terms suppresses the oscillations of large

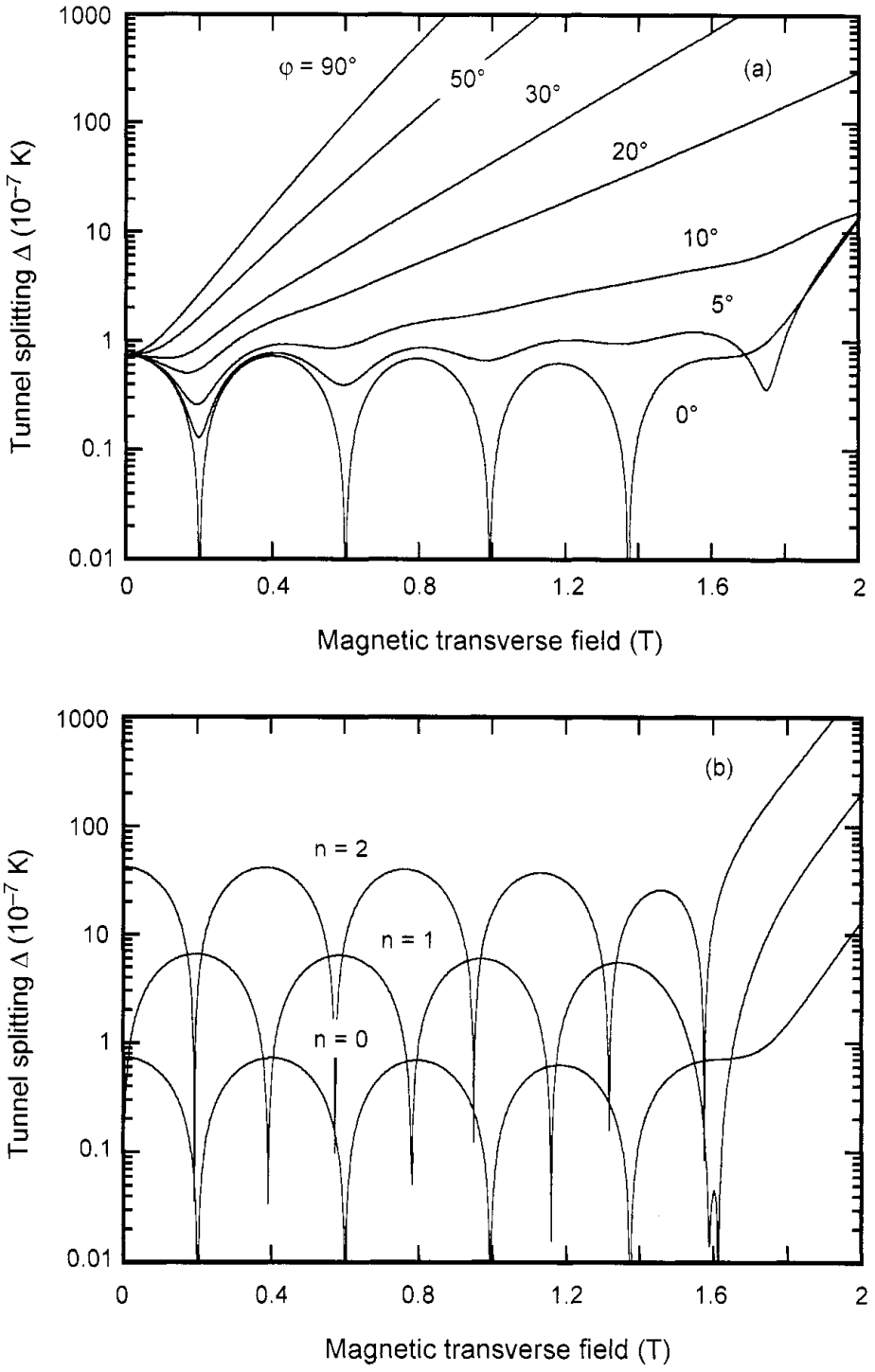

Figure 42. Calculated tunnel splitting Δ as a function of transverse field for (a) quantum transition between $m = \pm 10$ at several azimuth angles φ and (b) quantum transition between $m = -10$ and $(10-n)$ at $\varphi = 0°$ (Section V.A.3.b). The fourth-order terms suppress the oscillations of Δ for large transverse fields $|H_x|$.

transverse fields (Fig. 42). This region could not be studied in the current setup. Future measurements should focus on the higher-field region in order to find a better effective Hamiltonian.

B. Environmental Decoherence Effects in Molecular Clusters

At temperatures below 0.36 K, Fe_8 molecular clusters display a clear crossover from thermally activated relaxation to a temperature-independent quantum regime, with a pronounced resonance structure of the relaxation time as a function of the external field (Section V.A.1). It was surprising, however, that the observed relaxation of the magnetization in the quantum regime was found to be nonexponential and the resonance width orders of magnitude too large [116, 118]. The key to understand this seemingly anomalous behavior involves the hyperfine fields as well as the evolving distribution of the weak dipole fields of the nanomagnets themselves [143]. Both effects were shown to be the main source of decoherence at very low temperature. At higher temperatures, phonons are another source of decoherence.

In the following sections, we focus on the low temperature and low field limits, where phonon-mediated relaxation is astronomically long and can be neglected. In this limit, the $m = \pm S$ spin states are coupled due to the tunneling splitting $\Delta_{\pm S}$ which is about 10^{-7} K for Fe_8 (Section V.A.3) and 10^{-11} K for Mn_{12} [157] with $S = 10$. In order to tunnel between these states, the longitudinal magnetic energy bias $\xi = g\mu_B S H_{\text{local}}$ due to the local magnetic field H_{local} on a molecule must be smaller than $\Delta_{\pm S}$, implying a local field smaller than 10^{-8} T for Fe_8 clusters. Since the typical intermolecular dipole fields are of the order of 0.05 T, it seems at first that almost all molecules should be blocked from tunneling by a very large energy bias. Prokof'ev and Stamp have proposed a solution to this dilemma by proposing that fast dynamic nuclear fluctuations broaden the resonance, and the gradual adjustment of the dipole fields in the sample caused by the tunneling brings other molecules into resonance and allows continuous relaxation [143]. Some interesting predictions are briefly reviewed in the following section.

1. Prokof'ev–Stamp Theory

Prokof'ev and Stamp were the first who realized that there are localized couplings of environmental modes with mesoscopic systems which cannot be modeled with an "oscillator bath" model [158] describing delocalized environmental modes such as electrons, phonons, photons, and so on. They found that these localized modes such as nuclear and paramagnetic spins are often strong and described them with a spin bath model [159]. We do not review this theory* but focus on one

*For a review, see Ref. 160.

particular application which is interesting for molecular clusters [143]. Prokof'ev and Stamp showed that at a given longitudinal applied field H_z, the magnetization of a crystal of molecular clusters should relax at short times with a square-root time dependence which is due to a gradual modification of the dipole fields in the sample caused by the tunneling:

$$M(H_z,t) = M_{\text{in}} + (M_{\text{eq}}(H_z) - M_{\text{in}})\sqrt{\Gamma_{\text{sqrt}}(H_z)t} \tag{5.5}$$

Here M_{in} is the initial magnetization at time $t = 0$ (after a rapid field change), and $M_{\text{eq}}(H_z)$ is the equilibrium magnetization at H_z. The rate function $\Gamma_{\text{sqrt}}(H_z)$ is proportional to the normalized distribution $P(H_z)$ of molecules which are in resonance at H_z:

$$\Gamma_{\text{sqrt}}(H_z) = c\frac{\xi_0}{E_D}\frac{\Delta^2_{\pm S}}{4\hbar}P(H_z) \tag{5.6}$$

where ξ_0 is the line width coming from the nuclear spins, E_D is the Gaussian half-width of $P(H_z)$, and c is a constant of the order of unity which depends on the sample shape. If these simple relations are exact, then measurements of the short time relaxation as a function of the applied field H_z give directly the distribution $P(H_z)$, and they allows one to measure the tunnel splitting $\Delta_{\pm S}$ which is described in the next section.

2. *Hole Digging Method to Study Dipolar Distributions and Hyperfine Couplings*

Motivated by the Prokof'ev–Stamp theory [143], we developed a new technique—which we call the *hole digging method*—that can be used to observe the time evolution of molecular states in crystals of molecular clusters. It allowed us to measure the statistical distribution of magnetic bias fields in the Fe_8 system that arise from the weak dipole fields of the clusters themselves. A hole can be "dug" into the distribution by depleting the available spins at a given applied field. Our method is based on the simple idea that after a rapid field change, the resulting short time relaxation of the magnetization is directly related to the number of molecules which are in resonance at the given applied field. Prokof'ev and Stamp have suggested that the short time relaxation should follow a $\sqrt{t}$-relaxation law [Eq. (5.5)]. However, the hole digging method should work with any short time relaxation law—for example, a power law:

$$M(H_z,t) = M_{\text{in}} + (M_{\text{eq}}(H_z) - M_{\text{in}})(\Gamma_{\text{short}}(H_z)t)^{\alpha} \tag{5.7}$$

where Γ_{short} is a characteristic short time relaxation rate that is directly related to the number of molecules which are in resonance at the applied field H_z, and

$0<\alpha<1$ *in most cases.* $\alpha = 0.5$ *in the Prokof'ev–Stamp theory* [Eq. (5.5)] and Γ_{sqrt} is directly proportional to $P(H_z)$ [Eq. (4.6)]. The *hole digging method* can be divided into three steps (Fig. 43):

1. **Preparing the Initial State.** A well-defined initial magnetization state of the crystal of molecular clusters can be achieved by rapidly cooling the sample from high down to low temperatures in a constant applied field H_z^0. For zero applied field ($H_z = 0$) or rather large applied fields ($H_z > 1$ T), one yields the demagnetized or saturated magnetization state of the entire crystal, respectively. One can also quench the sample in a small field of

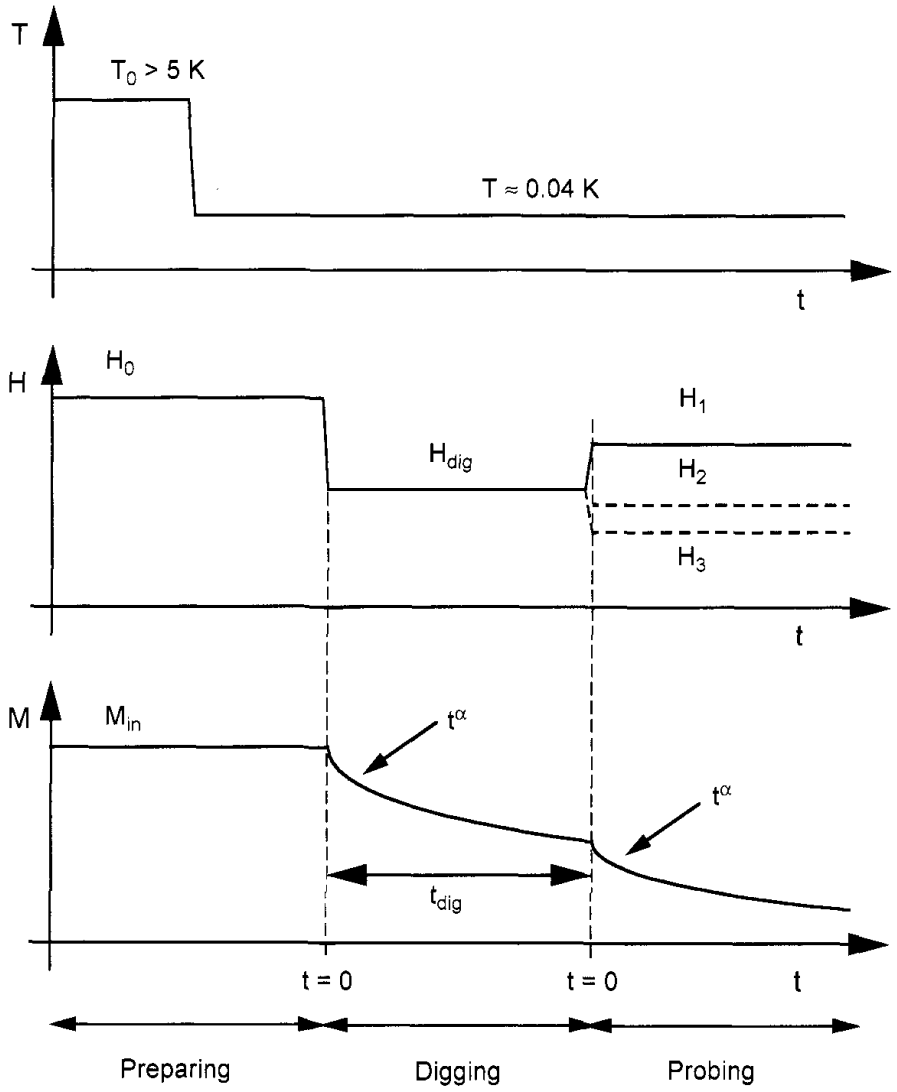

Figure 43. Schema of the hole digging method presenting the time dependence of temperature, applied field, and magnetization of the sample.

few milliteslas yielding any possible initial magnetization M_{in}. When the quench is fast (<1 s), the sample's magnetization does not have time to relax, either by thermal or by quantum transitions. This procedure yields a frozen thermal equilibrium distribution, whereas for slow cooling rates the molecule spin states in the crystal might tend to certain dipolar ordered ground state.

2. **Modifying the Initial State—Hole Digging.** After preparing the initial state, a field H_{dig} is applied during a time t_{dig}, called "digging field and digging time," respectively. During the digging time and depending on H_{dig}, a fraction of the molecular spins tunnel (back and/or forth); that is, they reverse the direction of magnetization.*
3. **Probing the Final State.** Finally, a field H_z^{probe} is applied (Fig. 43) to measure the short time relaxation from which one yields Γ_{short} [Eq. (5.7)] which is related to the number of spins that are still free for tunneling after step 2.

The entire procedure is then repeated many times but at other fields H_z^{probe} yielding $\Gamma_{short}(H_z, H_{dig}, t_{dig})$ which is related to the distribution of spins $P(H_z, H_{dig}, t_{dig})$ which are still free for tunneling after the hole digging. For $t_{dig} = 0$, this method maps out the initial distribution.

3. *Intermolecular Dipole Interaction in Fe_8*

We applied the hole digging method to several samples of molecular clusters and quantum spin glasses. The most detailed study has been done on the Fe_8 system. We found the predicted $\sqrt{t}$ relaxation [Eq. (5.5)] in experiments on fully saturated Fe_8 crystals [118, 161] and on nonsaturated samples [129]. Figure 44 displays a detailed study of the dipolar distributions revealing a remarkable structure that is due to next-nearest-neighbor effects [129].† These results are in good agreement with simulations [162, 163].

For a saturated initial state, the Prokof'ev–Stamp theory allows one to estimate the tunnel splitting $\Delta_{\pm S}$. Using Eqs. (3), (9), and (12) of Ref. 143, along with integration, we find $\int \Gamma_{sqrt} d\xi = c(\xi_0/E_D)(\Delta^2_{\pm S}/4\hbar)$, where c is a constant of the order of unity which depends on the sample shape. With $E_D = 15$ mT, $\xi_0 = 0.8$ mT, $c = 1$, and Γ_{sqrt} [129, 144], we find $\Delta_{\pm 10} = 1.2 \times 10^{-7}$ K which is

*The field sweeping rate to apply H_{dig} should be fast enough to minimize the change of the initial state during the field sweep.

†The peak at 0.04 T as well as the shoulder at 0.02 T and 0.04 T are originated by the clusters which have one nearest-neighbor cluster with reversed magnetization: The peak at 0.04 T corresponds to the reversal of the neighboring cluster along the **a** crystallographic axis, which almost coincides with the easy axis of magnetization, while the shoulder at 0.02 T and 0.04 T are due to the clusters along **b** and **c**.

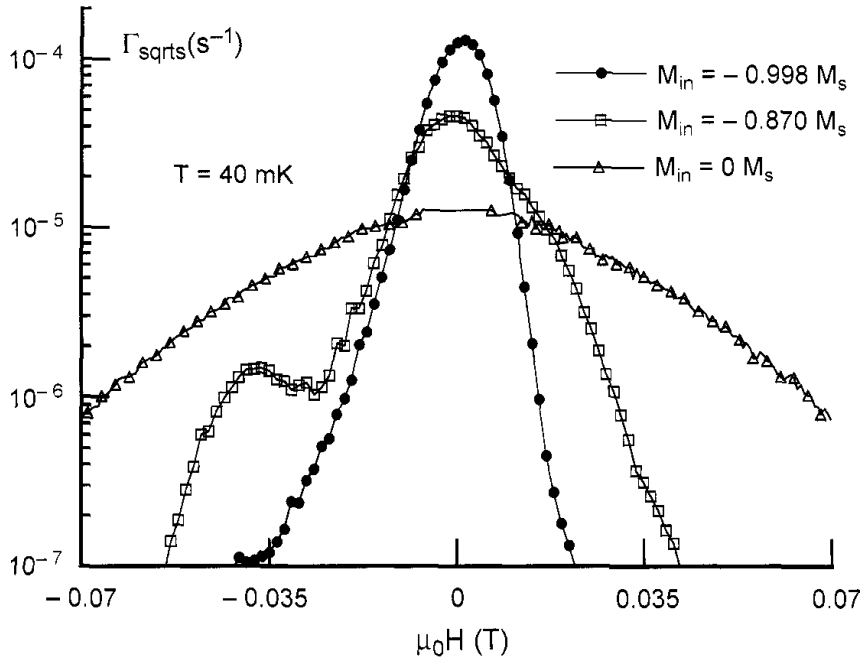

Figure 44. Field dependence of the short time square-root relaxation rates $\Gamma_{sqrt}(H_z)$ for three different values of the initial magnetization M_{in}. According to Eq. (5.6), the curves are proportional to the distribution $P(H_z)$ of magnetic energy bias due to local dipole field distributions in the sample. Note the logarithmic scale for Γ_{sqrt}. The peaked distribution labeled $M_{in} = -0.998\,M_s$ was obtained by saturating the sample, whereas the other distributions were obtained by thermal annealing. $M_{in} = -0.870\,M_s$ is distorted by nearest-neighbor lattice effects.

close to the result of $\Delta_{\pm 10} = 1.0 \times 10^{-7}$ K obtained by using a Landau–Zener method (Section V.A.2) [47]. Whereas the hole digging method probes the longitudinal dipolar distribution (H_z direction), the Landau–Zener method can be used to probe the transverse dipolar distribution by measuring the tunnel splittings Δ around a topological quench. Figure 45 displays such a study for the quantum transition between $m = \pm 10$, and $m = -10$ and 9. Particular efforts were made to align well the transverse field in direction of the hard axis. The initial magnetizations $0 \leq M_{in} \leq M_s$ were prepared by rapidly quenching the sample from 2 K in the present of a longitudinal applied field H_z. The quench takes approximately one second and thus the sample does not have time to relax, either by thermal activation or by quantum transitions, so that the high-temperature "thermal equilibrium" spin distribution is effectively frozen in. For $H_z > 1$ T, one gets an almost saturated magnetization state.

The measurements of $\Delta(M_{in})$ show a strong dependence of the minimal tunnel splittings on the initial magnetization (Fig. 45). They demonstrate that the transverse dipolar interaction between Fe_8 molecular clusters is largest of $M_{in} = 0$ — that is, similar to the longitudinal dipolar interaction (Fig. 44).

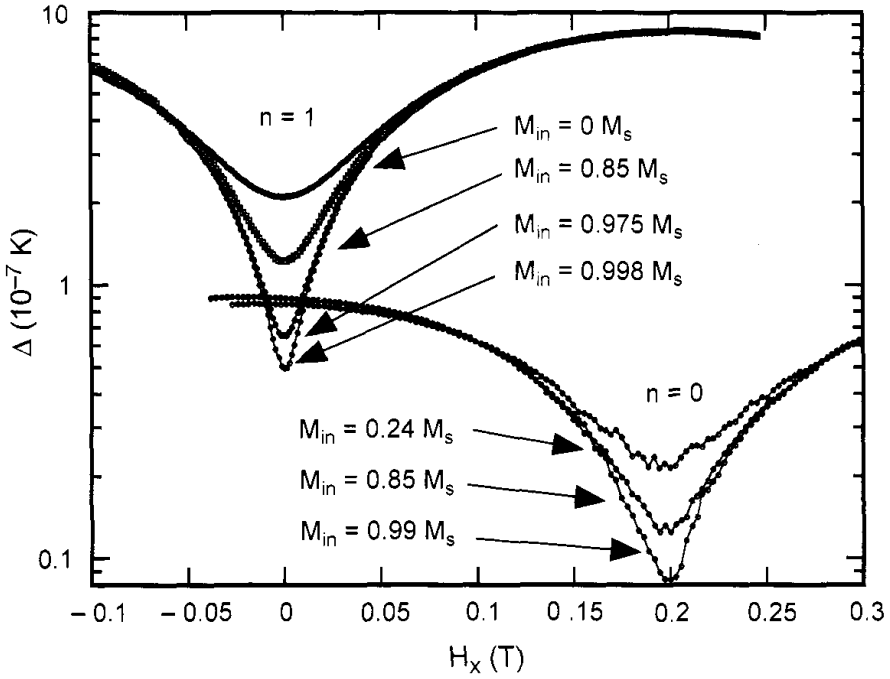

Figure 45. Detailed measurement of the tunnel splitting Δ around a topological quench for the quantum transition between $m = -10$ and $(10-n)$ at $\varphi = 0°$. Note the strong dependence on the initial magnetization M_{in} which demonstrates the transverse dipolar interaction between Fe_8 molecular clusters [129].

4. *Hyperfine Interaction in Fe_8 and Mn_{12}*

The strong influence of nuclear spins on resonant quantum tunneling in the molecular cluster Fe_8 was demonstrated for the first time [144] by comparing the relaxation rate of the standard Fe_8 sample with two isotopic modified samples: (i) ^{56}Fe is replaced by ^{57}Fe, and (ii) a fraction of ^{1}H is replaced by ^{2}H. By using the hole digging method, we measured an intrinsic broadening which is driven by the hyperfine fields. Our measurements are in good agreement with numerical hyperfine calculations [136, 144]. For $T > 1.5\,K$, the influence of nuclear spins on the relaxation rate is less important, suggesting that spin–phonon coupling dominates the relaxation rate.

Concerning Mn_{12} we did *not* find that the relaxation follows the $\sqrt{t}$-relaxation law at low temperatures [164]. It is well known that the situation in this sample is more complicated due to the fact that there are several coexisting species of Mn_{12} in any crystal, each with different relaxation times. In Ref. 164 we were able to isolate one faster relaxing species. The relaxation could be *approximately* fit to the $\sqrt{t}$-relaxation law, but in fact is better fit to a power law t^{α} with $0.3<\alpha<0.5$ (depending on the applied field). We applied the hole digging method to this species, and we found evidence for intrinsic line broadening

below 0.3 K which we suggest comes from nuclear spins in analogy with Fe_8. We also measured the relaxation of Mn_{12} at higher temperature (0.04–5 K) and small fields (< 0.1 T), and we found no evidence for a short time $\sqrt{t}$ relaxation.

5. Temperature Dependence of the Landau–Zener Tunneling Probability

In this section we present studies of the temperature dependence of the Landau–Zener tunneling probability P yielding a deeper insight into the spin dynamics of the Fe_8 cluster. By comparing the three isotopic samples (Section V.B.4.) we demonstrate the influence of nuclear spins on the tunneling mechanism and in particular on the lifetime of the first excited states. Our measurements show the need of a generalized Landau–Zener transition rate theory taking into account environmental effects such as hyperfine and spin–phonon coupling.*

All measurement so far were done in the pure quantum regime ($T < 0.36$ K) where transition via excited spin levels can be neglected. We discuss now the temperature region of small thermal activation ($T < 1$ K) where we should consider transition via excited spin levels as well [138, 140].

In order to measure the temperature dependence of the tunneling probability, we used the Landau–Zener method as described in Section V.A.2 with a phenomenological modification of the tunneling probability P (for a negative saturated magnetization):

$$P = n_{-10}P_{-10,10} + P_{th} \tag{5.8}$$

where $P_{-10,10}$ is given by (Eq. 5.2), n_{-10} is the Boltzmann population of the $m = -10$ spin level, and P_{th} is the overall tunneling probability via excited spin levels. $n_{-10} \approx 1$ for the considered temperature $T < 1$ K and a negative saturated magnetization of the sample.

Figure 46 displays the measured tunneling probability P for $^{st}Fe_8$ as a function of a transverse field H_x and for several temperatures. The oscillation of P are seen for all temperatures, but the periods of oscillations decrease for increasing temperature (Fig. 47). This behavior can be explained by the giant spin model [Eq. (5.1)] with fourth-order transverse terms (Section V.A.3.b). Indeed, the tunnel splittings of excited spin levels oscillate as a function of H_x with decreasing periods (Fig. 48).

Figure 49 presents the tunneling probability via excited spin levels $P_{th} = P - n_{-10}P_{-10,10}$. Surprisingly, the periods of P_{th} are temperature-independent in the

*Spin–phonon interactions mainly originate from the perturbation of the crystal field by lattice vibration, which produce both a fluctuating local strain and a fluctuating local rotation [140, 141, 165]. It is sufficient to retain the lowest-order terms which are quadratic with respect to spin operators. The resulting spin–phonon Hamiltonian contains (i) terms that commute with S_z and do not contribute to the relaxation, (ii) terms proportional to S_zS_- and S_zS_-, and (iii) terms proportional to S_+^2 and S_-^2. Thus, the spin–phonon interaction has matrix elements between states with quantum numbers m and m' if $|m-m'| = 1$ or 2 [140].

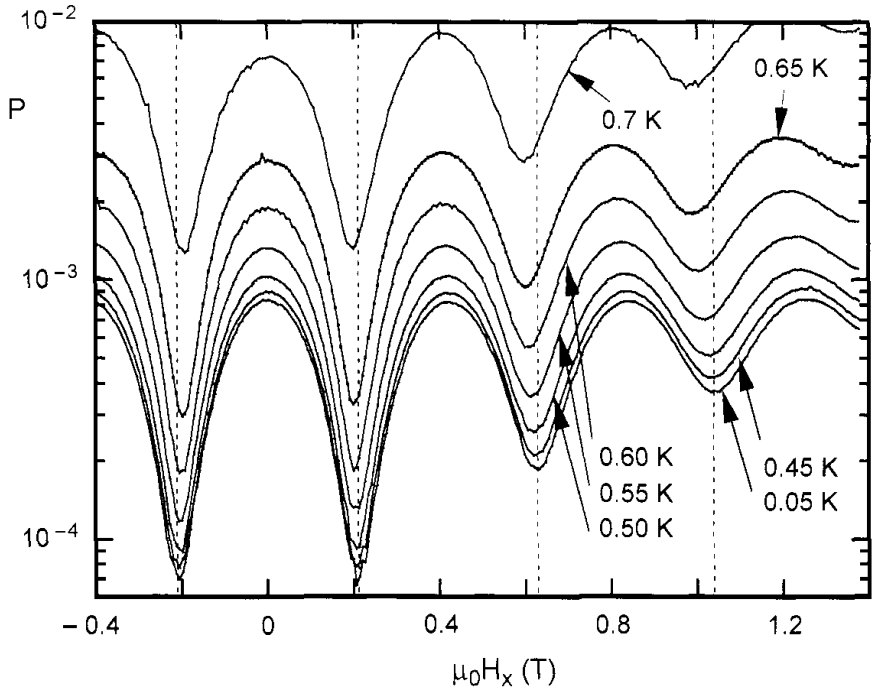

Figure 46. Transverse field dependence of the tunneling probability P at several temperatures, and the ground-state tunneling probability $P_{-10,10}$ measured at $T = 0.05$ K and for $^{57}Fe_8$. The field sweeping rate was 0.14 T/s. The dotted lines indicate the minima of $P_{-10,10}$.

region $T < 0.7$ K. This suggests that only transitions via excited levels $m = \pm 9$ are important in this temperature regime. This statement is confirmed by the following estimation [166].

Using Eq. (5.2), typical field sweeping rates of 0.1 T/s, and tunnel splittings from Fig. 48, one easily finds that the Landau–Zener tunneling probability of excited levels are $P_{-m,m} \approx 1$ for $m < 10$ and $\vec{H} \approx 0$. This means that the relaxation rates via excited levels are mainly governed by the lifetime of the excited levels and the time $\tau_{res,m}$ during which these levels are in resonance. The latter can be estimated by

$$\tau_{res,m} = \frac{\Delta_{-m,m}}{g\mu_B m \mu_0 dH_z/dt} \tag{5.9}$$

The probability for a spin to pass into the excited level m can be estimated by $\tau_m^{-1} e^{-E_{10,m}/k_B T}$, where $E_{10,m}$ is the energy gap between the levels 10 and m, and τ_m is the lifetime of the excited level m. One gets

$$P_{th} \approx \sum_{m=9,8} \frac{\tau_{res,m}}{\tau_m} e^{-E_{10,m}/k_B T} \approx \sum_{m=9,8} \frac{\Delta_{-m,m}}{\tau_m g\mu_B m \mu_0 dH_z/dt} e^{-E_{10,m}/k_B T} \tag{5.10}$$

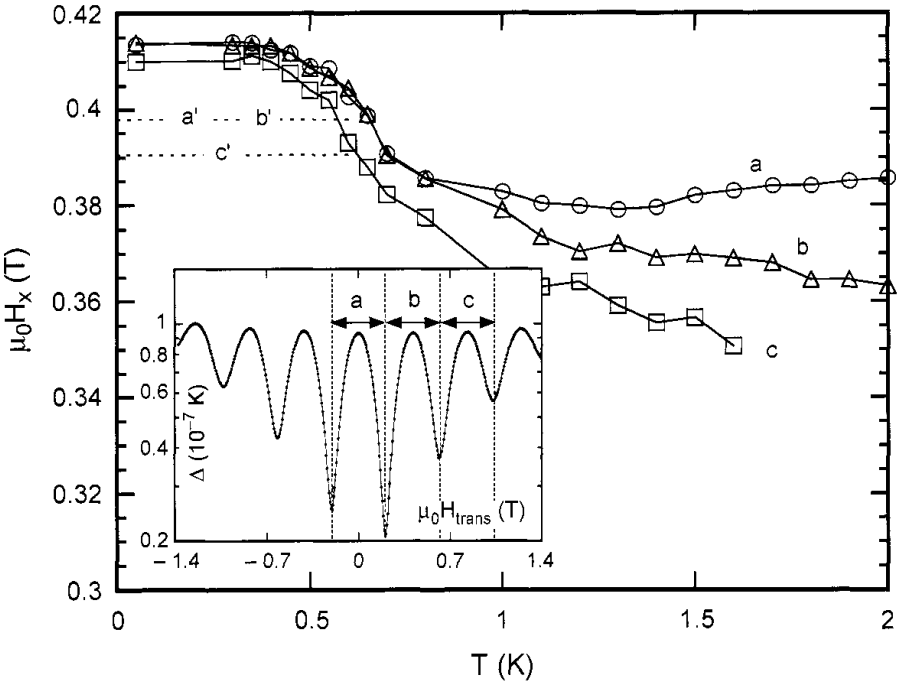

Figure 47. Temperature dependence of the field between minima of the tunneling probability P in Fig. 46. a, b, and c are defined in the inset. The dotted line labeled with a′, b′, and c′ were taken from P_{th} of Fig. 49; see also Ref. 126.

Note that this estimation neglects higher excited levels with $|m|<8$.* Figure 50 displays the measured P_{th} for the three isotopic Fe_8 samples. For $0.4\,K<T<1\,K$ we fitted Eq. (5.10) to the data, leaving *only* the level lifetimes τ_9 and τ_8 as adjustable parameters. All other parameters are calculated using the parameters in Section V.A.3.b. We obtain $\tau_9 = 1.0$, 0.5, and 0.3×10^{-6} s, and $\tau_8 = 0.7$, 0.5, and 0.4×10^{-7} s for $^{D}Fe_8$, $^{st}Fe_8$, and $^{57}Fe_8$, respectively. These results indicate that only the first excited level has to be considered for $0.4\,K<T<0.7\,K$. Indeed, the second term of the summation in Eq. (5.10) is negligible in this temperature interval. It is interesting to note that this finding is in contrast to hysteresis loop measurements on Mn_{12} [120, 167] which were interpreted to have an abrupt transition between thermal assisted and pure quantum tunneling [168]. Furthermore, our result shows clearly the influence of nuclear spins which seem to decrease the level lifetimes τ_m—that is, to increase dissipative effects.

The nuclear magnetic moment and not the mass of the nuclei seems to have the major effect on the dynamics of the magnetization. In fact the mass is increased in both isotopically modified samples whereas the effect on the relaxation rate is opposite. On the other hand, ac-susceptibility measurements

*The probability of phonon induced transitions with $|\Delta m|>2$ are very small [138–140]. Also the Boltzmann factor $e^{-E_{10,m}/k_B T}$ is very small for $m<8$ and $T<1$ K.

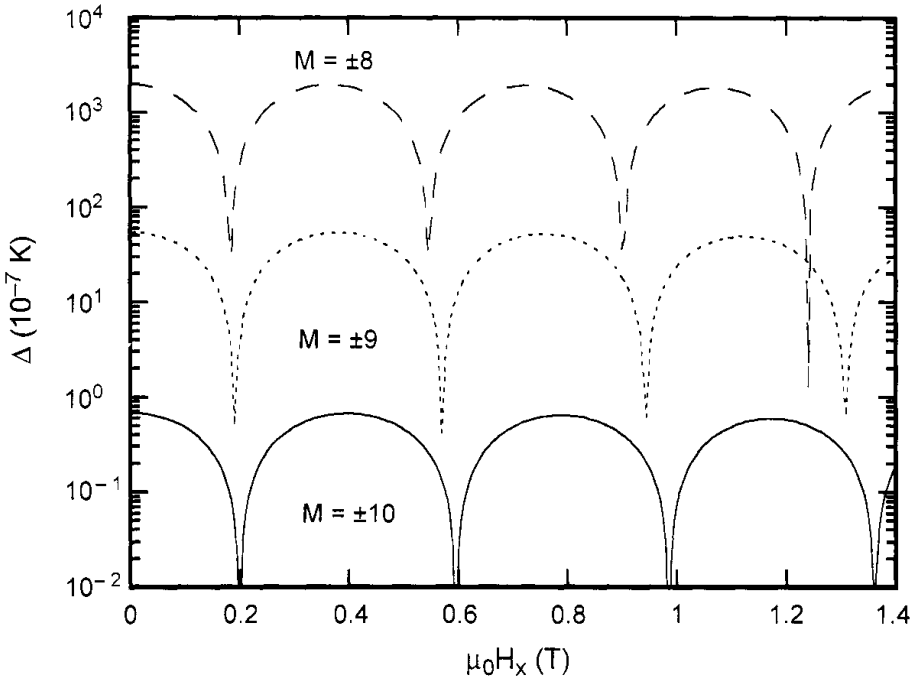

Figure 48. Calculated tunnel splitting $\Delta_{m,m'}$ as a function of the transverse field H_x for quantum transition between $m = \pm 10$, ± 9 and ± 8 (Section V.A.3.b).

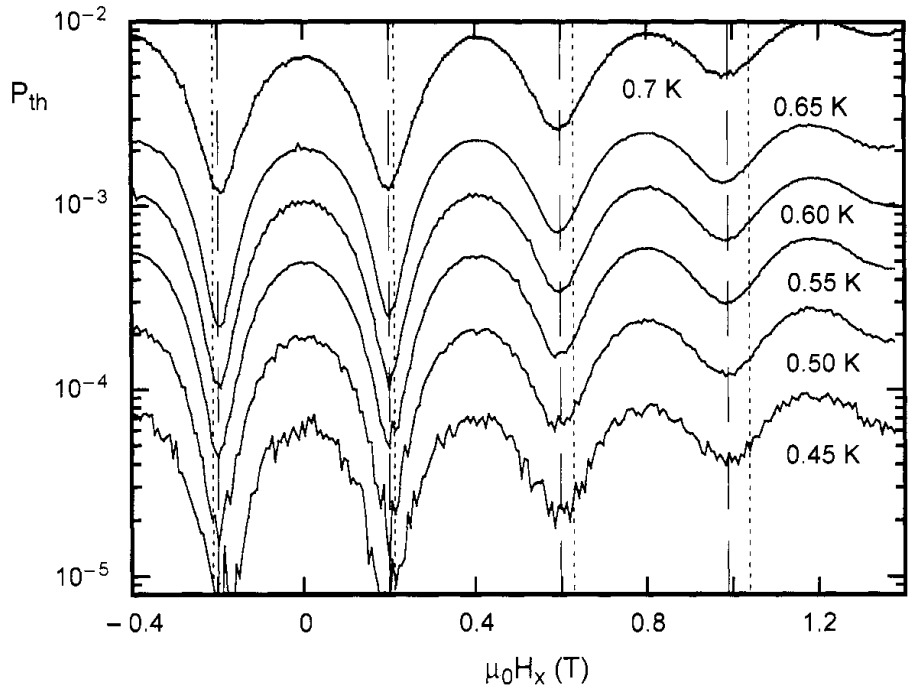

Figure 49. Transverse field dependence of P_{th} which is the difference between the measured tunnel probability P and the ground-state tunnel probability $n_{-10}P_{-10,10}$ measured at $T = 0.05$ K (see Fig. 46). The field sweeping rate was 0.14 T/s. The dotted lines indicate the minima of P_{th}, whereas the dashed lines indicate the minima of $P_{-10,10}$ (see Fig. 47).

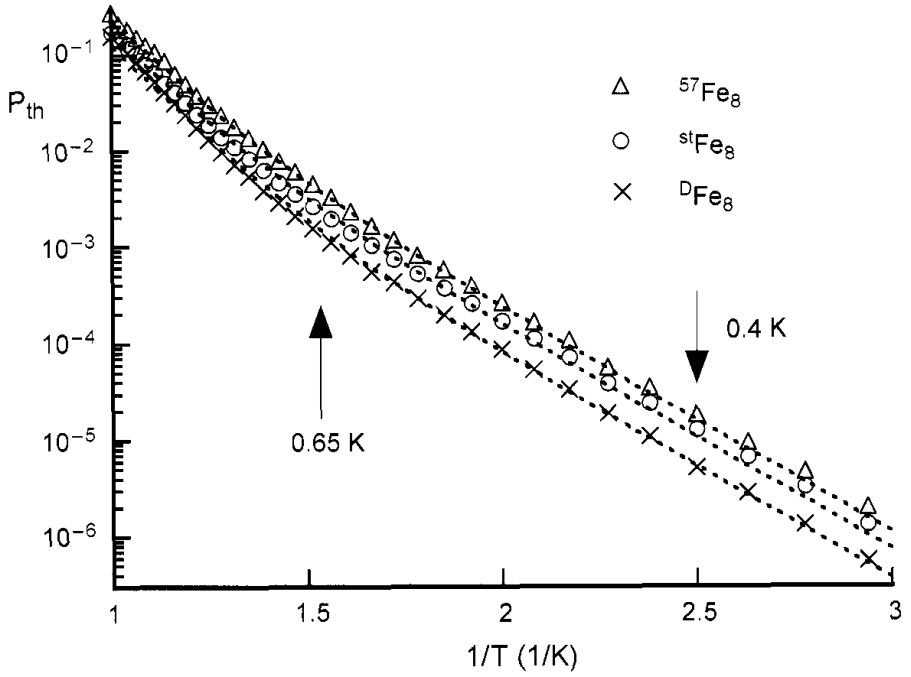

Figure 50. Temperature dependencies of P_{th} for $H_x = 0$ for three Fe_8 samples. The field sweeping rate was 0.14 T/s. The dotted lines are fits of the data using Eq. (5.10).

at $T > 1.5$ K showed no clear difference between the three samples; this suggested that above this temperature, where the relaxation is predominately due to spin–phonon coupling [140, 141], the role of the nuclear spins is less important. Although the increased mass of the isotopes changes the spin–phonon coupling, this effect seems to be small.

We can also exclude that the change of mass for the three isotopic samples has induced a significant change in the magnetic anisotropy of the clusters. In fact the measurements below $T < 0.35$ K, where spin–phonon coupling is negligible, have shown that (i) relative positions of the resonances as a function of the longitudinal field H_z are unchanged,* and (ii) all three samples have the same period of oscillation of Δ as a function of the transverse field H_x [47], a period which is very sensitive to any change of the anisotropy constants.

6. *Conclusion on Molecular Magnets*

In conclusion, we presented detailed measurements which demonstrated that molecular magnets offer a unique opportunity to explore the quantum dynamics

*We observed a small shift of the resonances of the order of magnitude of 1 mT, positive for $^{57}Fe_8$ and negative for $^{D}Fe_8$ ($M_{init} = -M_s$). This can also be attributed to the modified hyperfine fields. However, a quantitative measurement is complicated by the fact that it is impossible to have two crystals with exactly the same shape—that is, the same internal fields.

of a large but finite spin.* We focused our discussion on the Fe_8 molecular magnet because it is the first system where studies in the pure quantum regime were possible. The tunneling in this system is remarkable because it does not show up at the lowest order of perturbation theory.

What remains still debated is the possibility of observing quantum coherence between states of opposite magnetization. Dipole–dipole and hyperfine interactions are sources of decoherence. In other words, when a spin has tunneled through the barrier, it experiences a huge modification of its environment (hyperfine and dipolar) which prohibits the back tunneling. Prokof'ev and Stamp suggested three possible strategies to suppress the decoherence [172]. (i) Choose a system where the NMR frequencies far exceed the tunnel frequencies making any coupling impossible. (ii) Isotopically purify the sample to remove all nuclear spins. (iii) Apply a transverse field to increase the tunnel rate to frequencies much larger than hyperfine field fluctuations. All three strategies are difficult to realize. However, some authors tried to realize the last one by performing EPR experiments in the presence of a large transverse field [173]. Absorption of radio-frequency electromagnetic fields were observed which might be due to induced transitions near the tunnel splitting. However, no experiments showed the oscillatory behavior in the time domain which might be evidenced by a spin-echo type of experiment.

Concerning the perspectives of the field of single molecule magnets, we expect that chemistry is going to play a major role through the synthesis of novel larger spin clusters with strong anisotropy. We want to stress that there are already many other molecular magnets (see, for instance, Refs. 121–124) which are possible model systems. We believe that more sophisticated theories are needed which describe the dephasing effects of the environment onto the quantum system. These investigations are important for studying the quantum character of molecular clusters for applications like "quantum computers." The first implementation of Grover's algorithm with molecular magnets has been proposed [174].

C. Quantum Tunneling of Magnetization in Individual Single-Domain Nanoparticles

The following sections focuses on magnetic quantum tunneling (MQT) studied in individual nanoparticles or nanowires where the complications due to distributions of particle size, shape, and so on, are avoided. The experimental

*Molecules with small spin have also been studied. For example, time-resolved magnetization measurements were performed on a spin 1/2 molecular complex, so-called V_{15} [169]. Despite the absence of a barrier, magnetic hysteresis is observed over a time scale of several seconds. A detailed analysis in terms of a dissipative two-level model has been given, in which fluctuations and splittings are of the same energy. Spin–phonon coupling leads to long relaxation times and to a particular "butterfly" hysteresis loop [170, 171].

evidence for MQT in a single-domain particle or in assemblies of particles is still a controversial subject. We shall therefore concentrate on the necessary experimental conditions for MQT and review some experimental results which suggest that quantum effects might even be important in nanoparticles with $S = 10^5$ or larger. We start by reviewing some important predictions concerning MQT in a single-domain particle.

1. *Magnetic Quantum Tunneling in Nanoparticles*

On the theoretical side, it has been shown that in small magnetic particles, a large number of spins coupled by strong exchange interaction can tunnel through the energy barrier created by magnetic anisotropy. It has been proposed that there is a characteristic crossover temperature T_c below which the escape of the magnetization from a metastable state is dominated by quantum barrier transitions, rather than by thermal over barrier activation. Above T_c the escape rate is given by thermal over barrier activation (Section IV).

In order to compare experiment with theory, predictions of the crossover temperature T_c and the escape rate Γ_{QT} in the quantum regime are relevant. Both variables should be expressed as a function of parameters that can be changed experimentally. Typical parameters are the number of spins S, effective anisotropy constants, applied field strength and direction, coupling to the environment (dissipation), and so on. Many theoretical papers have been published during the last few years [108]. We discuss here a result specially adapted for single-particle measurements, which concerns the field dependence of the crossover temperature T_c.

The crossover temperature T_c can be defined as the temperature where the quantum switching rate equals the thermal one. The case of a magnetic particle, as a function of the applied field direction, has been considered by several authors [175–177]. We have chosen the result for a particle with biaxial anisotropy as the effective anisotropy of most particles can be approximately described by strong uniaxial and weak transverse anisotropy. The result due to Kim can be written in the following form [177]:

$$T_c(\theta) \sim \mu_0 H_{\parallel} \varepsilon^{1/4} \sqrt{1 + a(1 + |\cos\theta|^{2/3})}\, \frac{|\cos\theta|^{1/6}}{1 + |\cos\theta|^{2/3}} \tag{5.11}$$

where $\mu_0 H_{\parallel} = K_{\parallel}/M_S$ and $\mu_0 H_{\perp} = K_{\perp}/M_s$ are the parallel and transverse anisotropy fields given in Tesla, $K_{\parallel}$ and $K_{\perp}$ are the parallel and transverse anisotropy constants of the biaxial anisotropy, θ is the angle between the easy axis of magnetization and the direction of the applied field, and $\varepsilon = (1 - H/H_{sw}^0)$. Equation (5.11) is valid for any ratio $a = H_{\perp}/H_{\parallel}$. The proportionality coefficient of (5.11) is of the order of unity (T_c is in units of Kelvin) and depends on the

approach used for calculation [177]. Equation (5.11) is plotted in Fig. 51 for several values of the ratio a. It is valid in the range $\sqrt{\varepsilon} < \theta < \pi/2 - \sqrt{\varepsilon}$.

The most interesting feature which may be drawn from (5.11) is that the crossover temperature is tunable using the external field strength and direction (Fig. 51) because the tunneling probability is increased by the transverse component of the applied field. Although at high transverse fields, T_c decreases again due to a broadening of the anisotropy barrier. Therefore, quantum tunneling experiments should always include studies of angular dependencies. When the effective magnetic anisotropy of the particle is known, MQT theories give clear predictions with no fitting parameters. MQT could also be studied as a function of the effective magnetic anisotropy. In practice, it is well known for single-particle measurements that each particle is somewhat different. Therefore, the effective magnetic anisotropy has to be determined for each particle (Section III.A.1).

Finally, it is important to note that most of the MQT theories neglect damping mechanisms. In Section IV.A [90] we discussed the case of ohmic damping, which is the simplest form of damping. More complicated damping mechanisms might play an important role. We expect more theoretical work on this in future.

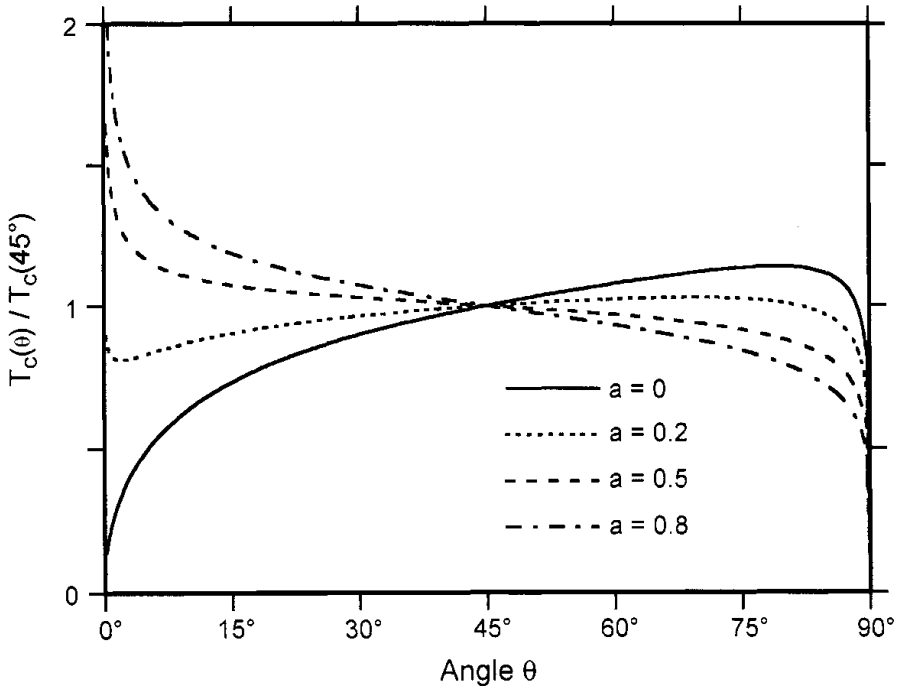

Figure 51. Normalized crossover temperature T_c as given by (5.11) and for several values of the ratio $a = H_\perp / H_\parallel$.

2. *Magnetization Reversal in Nanoparticles and Wires at Very Low Temperatures*

In order to avoid the complications due to distributions of particle size, shape, and so on, some groups have tried to study the temperature and field dependence of magnetization reversal of individual magnetic particles or wires. Most of the recent studies were done using magnetic force microscopy at room temperature. Low-temperature investigations were mainly performed via resistance measurements (Section II.A).

The first magnetization measurements of individual single-domain nanoparticles at low temperature ($0.1\,\mathrm{K}<T<6\,\mathrm{K}$) were presented by Wernsdorfer et al. [22]. The detector (a Nb microbridge-DC-SQUID; see Section II.B) and the particles studied (ellipses with axes between 50 and 1000 nm and thickness between 5 and 50 nm) were fabricated using electron beam lithography. Electrodeposited wires (with diameters ranging from 40 to 100 nm and lengths up to 5000 nm) were also studied [35, 74]. Waiting time and switching field measurements (Section IV.B) showed that the magnetization reversal of these particles and wires results from a single thermally activated domain wall nucleation, followed by a fast wall propagation reversing the particle's magnetization. For nanocrystalline Co particles of about 50 nm and below 1 K, a flattening of the temperature dependence of the mean switching field was observed which could not be explained by thermal activation. These results were discussed in the context of MQT. However, the width of the switching field distribution and the probability of switching are in disagreement with such a model because nucleation is very sensitive to factors like surface defects, surface oxidation, and perhaps nuclear spins. The fine structure of pre-reversal magnetization states is then governed by a multivalley energy landscape (in a few cases distinct magnetization reversal paths were effectively observed [59]) and the dynamics of reversal occurs via a complex path in configuration space.

Coppinger et al. [23] used telegraph noise spectroscopy to investigate two-level fluctuations (TLF) observed in the conductance of a sample containing self-assembled ErAs quantum wires and dots in a semi-insulating GaAs matrix. They showed that the TLF could be related to two possible magnetic states of a ErAs cluster and that the energy difference between the two states was a linear function of the magnetic field. They deduced that the ErAs cluster should contain a few tens of Er atoms. At temperatures between 0.35 K and 1 K, the associated switching rates of the TLF were thermally activated, whilst below 0.35 K the switching rate became temperature-independent. Tunneling of the magnetization was proposed in order to explain the observed behavior.

Some open questions remain: What is the object that is really probed by TLF? If this is a single ErAs particle, as assumed by the authors, the switching probability should be an exponential function of time. The preexponential factor

τ_0^{-1} (sometimes called attempt frequency) was found to lie between 10^3 and $10^6\,s^{-1}$ whereas expected values are between 10^9 and $10^{12}\,s^{-1}$. Why must one apply fields of about 2 T in order to measure two-level fluctuations which should be expected near zero field? What is the influence of the measurement technique on the sample?

By measuring the electrical resistance of isolated Ni wires with diameters between 20 and 40 nm, Hong and Giordano studied the motion of magnetic domain walls [24]. Because of surface roughness and oxidation, the domain walls of a single wire are trapped at pinning centers. The pinning barrier decreases with an increase in the magnetic field. When the barrier is sufficiently small, thermally activated escape of the wall occurs. This is a stochastic process that can be characterized by a switching (depinning) field distribution. A flattening of the temperature dependence of the mean switching field and a saturation of the width of the switching field distribution (rms. deviation σ) were observed below about 5 K. The authors proposed that a domain wall escapes from its pinning site by thermal activation at high temperatures and by quantum tunneling below $T_c \sim 5$ K.

These measurements pose several questions: What is the origin of the pinning center which may be related to surface roughness, impurities, oxidation, and so on? The sweeping rate dependence of the depinning field, as well as the depinning probability, could not be measured even in the thermally activated regime. Therefore, it was not possible to check the validity of the Néel–Brown model [9, 10, 86–88] or to compare measured and predicted rms. deviations σ. Finally, a crossover temperature T_c of about 5 K is three orders of magnitude higher than T_c predicted by current theories.

Later, Wernsdorfer et al. published results obtained on nanoparticles synthesized by arc discharge, with dimensions between 10 and 30 nm [36]. These particles were single crystalline, and the surface roughness was about two atomic layers. Their measurements showed for the first time that the magnetization reversal of a ferromagnetic nanoparticle of good quality can be described by thermal activation over a single-energy barrier as proposed by Néel and Brown [9, 10, 86–88] (see Section IV.C). The activation volume, which is the volume of magnetization overcoming the barrier, was very close to the particle volume, predicted for magnetization reversal by uniform rotation. No quantum effects were found down to 0.2 K. This was not surprising because the predicted crossover temperature is $T_c \sim 0.02$ K. The results of Wernsdorfer et al. constitute the preconditions for the experimental observation of MQT of magnetization on a single particle.

Just as the results obtained with Co nanoparticles [36], a quantitative agreement with the Néel–Brown model of magnetization reversal was found on $BaFe_{12-2x}Co_xTi_xO_{19}$ nanoparticles ($0<x<1$) [37], which we will call BaFeO, in the size range of 10–20 nm. However, strong deviations from this model were

evidenced for the smallest particles containing about 10^5 μ_B and for temperatures below 0.4 K. These deviations are in good agreement with the theory of macroscopic quantum tunneling of magnetization. Indeed, the measured angular dependence of $T_c(\theta)$ is in excellent agreement with the prediction given by (4.11) (Fig. 52). The normalization value $T_c(45°) = 0.31$ K compares well with the theoretical value of about 0.2 K.

Although the above measurements are in good agreement with MQT theory, we should not forget that MQT is based on several strong assumptions. Among them, there is the assumption of a giant spin; that is, all magnetic moments in the particle are rigidly coupled together by strong exchange interaction. This approximation might be good in the temperature range where thermal activation is dominant, but is it not yet clear if this can be made for very low energy barriers (see, for example, Section IV.C.4). Future measurements might give us the answer.

3. *Quantization of the Magnetization*

In order to give a definite proof that MQT can occur in a magnetic nanoparticle we propose to surge for the energy level quantization of its collective spin state. This was recently evidenced in molecular cluster like Fe_8 having a collective spin state $S = 10$ (Section V.A). In the case of the BaFeO particles with $S \approx 10^5$

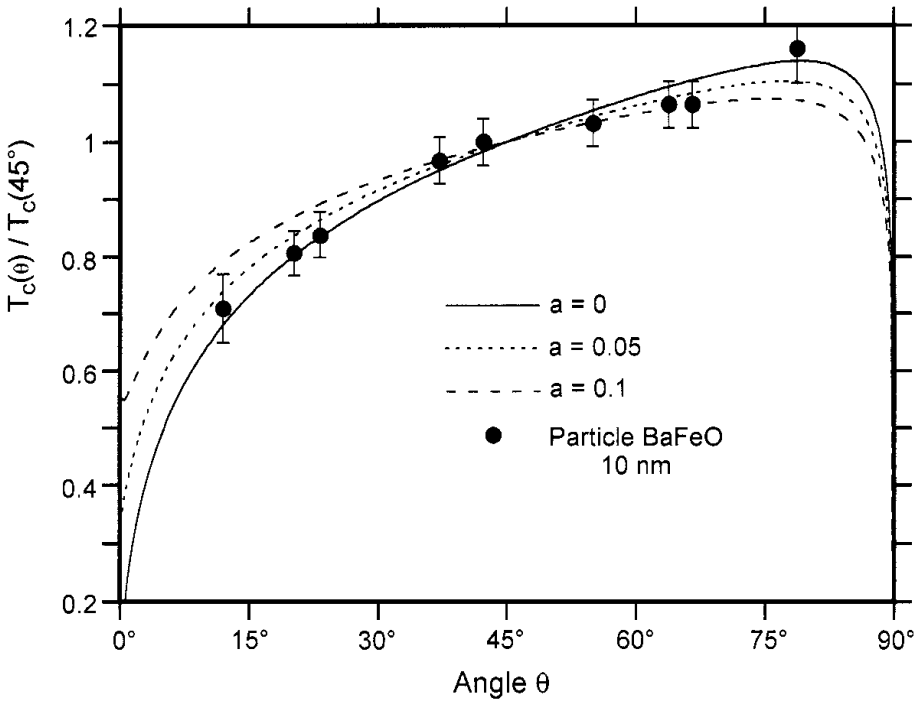

Figure 52. Angular dependence of the crossover temperature T_c for a 10-nm $BaFe_{10.4}Co_{0.8}Ti_{0.8}O_{19}$ particle with $S \approx 10^5$. The lines are given by (5.11) for different values of the ratio $a = H_\perp / H_\parallel$. The experimental data are normalized by $T_c(45°) = 0.31$ K.

[37], the field separation associated with level quantization is rather small: $\Delta H \approx H_a/2S \approx 0.002\,\text{mT}$ where H_a is the anisotropy field. However, for a 3-nm Co cluster with $S \approx 10^3$ the field separation $\Delta H = H_a/2S \sim 0.2\,\text{mT}$ might be large enough to be measurable.

Figure 53 displays schematically the field values of resonances between quantum states of S. When the applied field is ramped in a certain direction, the resonance might occur for fields $H_{res} \approx n \times (H_a/2S)(1/\cos\theta)$, with $n = 1, 2, 3, \ldots$. θ is the angle between the applied field and the easy axis of magnetization. For large spins S, tunneling might be observable only for fields which are close to the classical switching field (Fig. 53). The resonance fields could be evidenced by measuring switching field distributions (inset of Fig. 53) as a function of the angle θ.

Such a study is presented in Fig. 54 for a 3-nm Fe cluster with $S \approx 800$. The estimated field separation $\Delta H = H_a/2S$ is about 0.1 mT whereas the width of the switching field distribution is about ten times larger. We observed sometimes a small periodic fine structure which is close to the expected ΔH. However, this fine structure always disappeared when averaging over more measurements. A possible origin might be hyperfine couplings that broaden the energy levels (Section V.B.4) leading to a complete overlap of adjacent energy levels. It is

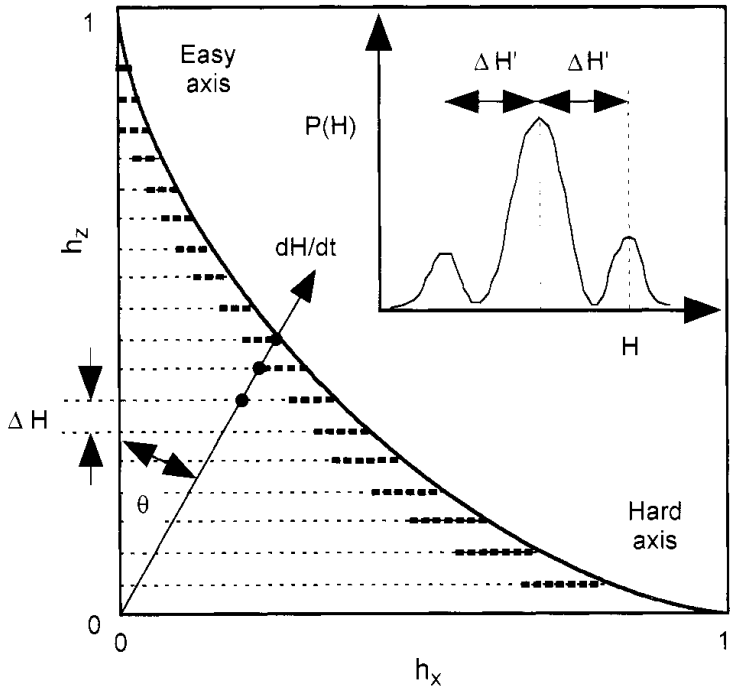

Figure 53. Schematic view of the resonance fields of a giant spin S. The continuous line is the classical switching fields of Stoner–Wohlfarth (Section III.A). The inset presents schematically a switching field histogram with $\Delta H' \approx (H_a/2S)(1/\cos\theta)$.

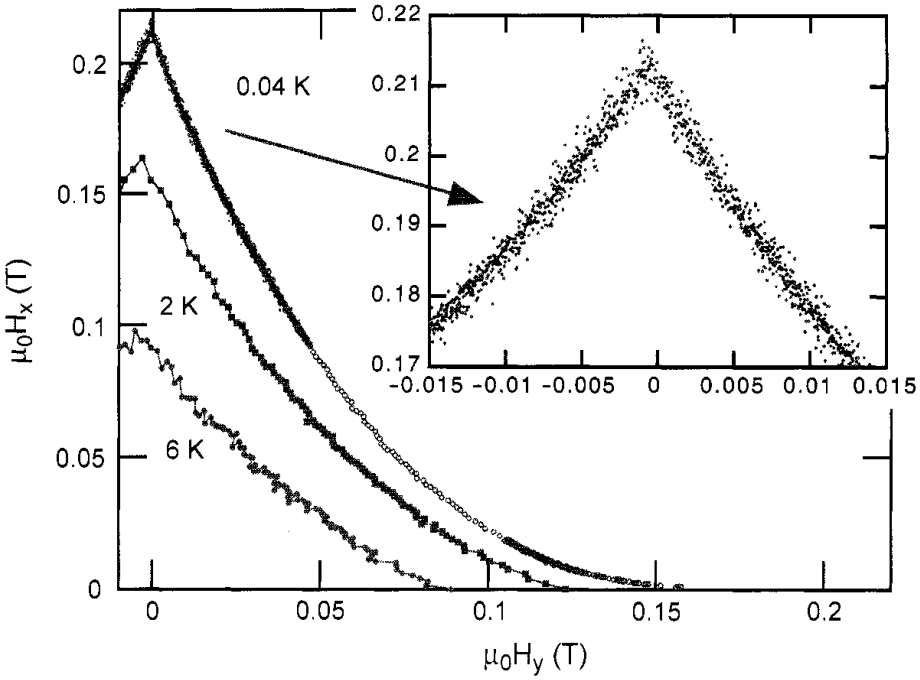

Figure 54. Angular dependence of the switching field of a 3-nm Fe cluster with $S \approx 800$. The inset presents detailed measurements near the easy axis of magnetization.

also important to mention that the switching field distributions were temperature-independent for $0.04\,\mathrm{K} < T < 0.2\,\mathrm{K}$.

In some cases, we observed huge variations of the switching field (Figs. 30 and 31) which might be due to exchange bias of frustrated spin configurations. However, quantum effects are not completely excluded.

Future measurements should focus on the level quantization of collective spin states of $S = 10^2$.

VI. SUMMARY AND CONCLUSION

Nanometer-sized magnetic particles have generated continuous interest as the study of their properties has proved to be scientifically and technologically very challenging. In the last few years, new fabrication techniques have led to the possibility of making small objects with the required structural and chemical qualities. In order to study these objects, new local measuring techniques were developed such as magnetic force microscopy, magnetometry based on micro-Hall probes, or micro-SQUIDs. This led to a new understanding of the magnetic behavior of nanoparticles.

In this chapter we reviewed the most important theories and experimental results concerning the magnetization reversal of single-domain particles and

clusters. Special emphasis is laid on single-particle measurements avoiding complications due to distributions of particle size, shape, and so on. Measurements on particle assemblies have been reviewed in Ref. 8. We mainly discuss the low-temperature regime in order to avoid spin excitations.

Section II reviews briefly the commonly used measuring techniques. Among them, electrical transport measurements, Hall probes, and micro-SQUID techniques seem to be the most convenient techniques for low-temperature measurements.

Section III discusses the mechanisms of magnetization reversal in single-domain particles at zero kelvin. For extremely small particles, the magnetization should reverse by uniform rotation of magnetization (Section III.A). For somewhat larger particles, a nonuniform reversal mode occurs like the curling mode (Section III.B). For even larger particles, magnetization reversal occurs via a domain wall nucleation process starting in a rather small volume of the particle (Section III.B.3).

The influence of temperature on the magnetization reversal is reported in Section IV. We discuss in detail the Néel, Brown, and Coffey's theory of magnetization reversal by thermal activation (Section IV).

Finally, Section V shows that for very small systems or very low temperature, magnetization can reverse via quantum tunneling. The boundary between classical and quantum physics has become a very attractive field of research. This section discusses detailed measurements which demonstrated that molecular magnets offer an unique opportunity to explore the quantum dynamics of a large but finite spin. The discussion is focused on the Fe_8 molecular magnet with $S = 10$ because it is the first system where studies in the pure quantum regime were possible. We showed that the understanding of the environmental decoherence is one of the most important issues, in particular for future applications of quantum devices. We then discussed tunneling in nanoparticles and showed how one might give a definite proof of their quantum character at low temperature.

In conclusion, the understanding of the magnetization reversal in nanostructures requires the knowledge of many physical phenomena, and nanostructures are therefore particularly interesting for the development of new fundamental theories of magnetism and in modeling new magnetic materials for permanent magnets or high density recording. Using the quantum character of nanostructures for applications like "quantum computers" will be one of the major concerns of the next decades.

Acknowledgments

The author is indebted to A. Benoit, E. Bonet Orozco, V. Bouchiat, I. Chiorescu, M. Faucher, K. Hasselbach, M. Jamet, D. Mailly, B. Pannetier, and C. Thirion for their experimental contributions and the development of the micro-SQUID technology. The author acknowledges the collaborations with J.-Ph. Ansermet,

B. Barbara, A. Caneschi, A. Cornia, N. Demoncy, B. Doudin, V. Dupuis, O. Fruchart, D. Gatteschi, O. Kubo, J.-P. Nozieres, H. Pascard, C. Paulsen, A. Perez, C. Sangregorio, and R. Sessoli. He is also indebted to W. T. Coffey, A. Garg, J. Miltat, N. Prokof'ev, P. Stamp, A. Thiaville, I. Tupitsyn, and J. Villain for many fruitful and motivating discussions. Finally, O. Fruchart is specially acknowledged for his critical review of the manuscript. This work has been supported by CNRS, DRET, MASSDOTS, and Rhône-Alpes.

References

1. A. Hubert and R. Schäfer, *Magnetic Domains: The Analysis of Magnetic Microstructures*, Springer-Verlag, New York, 1998.
2. Aharoni, *An Introduction to the Theory of Ferromagnetism*, Oxford University Press, London, 1996.
3. A. J. Freemann and R. Wu, *J. Magn. Magn. Mat.* **100**, 497 (1991).
4. G. M. Pastor, J. Dorantes-Dèvila, S. Pick, and H. Dreyssé, *Phys. Rev. Lett.* **75**, 326 (1995).
5. C. Kohl and G. F. Bertsch, *Phys. Rev. B* **60**, 4205 (1999).
6. I. M. L. Billas, A. Châtelain, and W. A. de Heer, *J. Magn. Magn. Mat.* **168**, 64 (1997).
7. S. E. Apsel, J. W. Emmert, J. Deng, and L. A. Bloomfield, *Phys. Rev. Lett.* **76**, 1441 (1996).
8. J. L. Dormann, D. Fiorani, and E. Tronc, *Adv. Chem. Phys.* **98**, 283 (1997).
9. L. Néel, *Ann. Geophys.* **5**, 99 (1949).
10. L. Néel, *C. R. Acad. Sci.* **228**, 664 (1949).
11. A. H. Morrish and S. P. Yu, *Phys. Rev.* **102**, 670 (1956).
12. J. E. Knowles, *IEEE Trans. Mag.* **MAG-14**, 858 (1978).
13. A. Tonomura, T. Matsuda, J. Endo, T. Arii, and K. Mihama, *Phys. Rev. B* **34**, 3397 (1986).
14. H. J. Richter, *J. Appl. Phys.* **65**, 9 (1989).
15. S. J. Hefferman, J. N. Chapman, and S. McVitie, *J. Magn. Magn. Mat.* **95**, 76 (1991).
16. C. Salling, S. Schultz, I. McFadyen, and M. Ozaki, *IEEE Trans. Mag.* **27**, 5185 (1991).
17. N. Bardou, B. Bartenlian, C. Chappert, R. Megy, P. Veillet, J. P. Renard, F. Rousseaux, M. F. Ravet, J. P. Jamet, and P. Meyer, *J. Appl. Phys.* **79**, 5848 (1996).
18. T. Chang and J. G. Chu, *J. Appl. Phys.* **75**, 5553 (1994).
19. M. Ledermann, S. Schultz, and M. Ozaki, *Phys. Rev. Lett.* **73**, 1986 (1994).
20. J. Bansmann, V. Senz, L. Lu, A. Bettac, and K. H. Meiweis-Broer, *J. Electron Spectrosc. Relat. Phenom.* **106**, 221 (2000).
21. K. H. Meiweis-Broer, *Phys. Bl.* **55**, 21 (1999).
22. W. Wernsdorfer, K. Hasselbach, D. Mailly, B. Barbara, A. Benoit, L. Thomas, and G. Suran, *J. Magn. Magn. Mat.* **145**, 33 (1995).
23. F. Coppinger, J. Genoe, D. K. Maude, U. Genner, J. C. Portal, K. E. Singer, P. Rutter, T. Taskin, A. R. Peaker, and A. C. Wright, *Phys. Rev. Lett.* **75**, 3513 (1995).
24. K. Hong and N. Giordano, *J. Magn. Magn. Mat.* **151**, 396 (1995).
25. J. E. Wegrowe, S. E. Gilbert, D. Kelly, B. Doudin, and J.-Ph. Ansermet, *IEEE Trans. Magn.* **34**, 903 (1998).

26. A. D. Kent, S. von Molnar, S. Gider, and D. D. Awschalom, *J. Appl. Phys.* **76**, 6656 (1994).
27. J. G. S. Lok, A. K. Geim, J. C. Maan, S. V. Dubonos, L. Theil Kuhn, and P. E. Lindelof, *Phys. Rev. B* **58**, 12201 (1998).
28. T. Schweinböck, D. Weiss, M. Lipinski, and K. Eberl, *J. Appl. Phys.* **87**, 6496 (2000).
29. V. Gros, Shan-Fab Lee, G. Faini, A. Cornette, A. Hamzic, and A. Fert, *J. Magn. Magn. Mat.* **165**, 512 (1997).
30. W. J. Gallagher, S. S. P. Parkin, Yu Lu, X. P. Bian, A. Marley, K. P. Roche, R. A. Altman, S. A. Rishton, C. Jahnes, T. M. Shaw, and Gang Xiao, *J. Appl. Phys.* **81**, 3741 (1997).
31. J.-E. Wegrowe, D. Kelly, A. Franck, S. E. Gilbert, and J.-Ph. Ansermet, *Phys. Rev. Lett.* **82**, 3681 (1999).
32. L. F. Schelp, A. Fert, F. Fettar, P. Holody, S. F. Lee, J. L. Maurice, F. Petroff, and A. Vaures, *Phys. Rev. B* **56**, R5747 (1997).
33. S. Guéron, M. M. Deshmukh, E. B. Myers, and D. C. Ralph, *Phys. Rev. Lett.* **83**, 4148 (1999).
34. W. Wernsdorfer, K. Hasselbach, A. Benoit, B. Barbara, D. Mailly, J. Tuaillon, J. P. Perez, V. Dupuis, J. P. Dupin, G. Guiraud, and A. Perez, *J. Appl. Phys.* **78**, 7192 (1995).
35. W. Wernsdorfer, B. Doudin, D. Mailly, K. Hasselbach, A. Benoit, J. Meier, J.-Ph. Ansermet, and B. Barbara, *Phys. Rev. Lett.* **77**, 1873 (1996).
36. W. Wernsdorfer, E. Bonet Orozco, K. Hasselbach, A. Benoit, B. Barbara, N. Demoncy, A. Loiseau, D. Boivin, H. Pascard, and D. Mailly, *Phys. Rev. Lett.* **78**, 1791 (1997).
37. W. Wernsdorfer, E. Bonet Orozco, K. Hasselbach, A. Benoit, D. Mailly, O. Kubo, H. Nakano, and B. Barbara, *Phys. Rev. Lett.* **79**, 4014 (1997).
38. E. Bonet, W. Wernsdorfer, B. Barbara, A. Benoit, D. Mailly, and A. Thiaville, *Phys. Rev. Lett.* **83**, 4188 (1999).
39. M. Jamet, W. Wernsdorfer, C. Thirion, D. Mailly, V. Dupuis, P. Mélinon, and A. Pérez, *Phys. Rev. Lett.* **86**, 4586 (2001); cond-mat/0012029.
40. J. Clarke, A. N. Cleland, M. H. Devoret, D. Esteve, and J. M. Martinis, *Science* **239**, 992 (1988).
41. M. Ketchen, D. J. Pearson, K. Stawiaasz, C-H. Hu, A. W. Kleinsasser, T. Brunner, C. Cabral, V. Chandrashekhar, M. Jaso, M. Manny, K. Stein, and M. Bhushan, *IEEE Appl. Supercond.* **3**, 1795 (1993).
42. P. W. Anderson and A. H. Dayem, *Phys. Rev. Lett.* **13**, 195 (1964).
43. C. Chapelier, M. El Khatib, P. Perrier, A. Benoit, and D. Mailly, in *Superconducting Devices and Their Applications*, *SQUID 91*, H. Koch and H. Lbbig, eds., Springer, Berlin, 1991, p. 286.
44. D. Mailly, C. Chapelier, and A. Benoit, *Phys. Rev. Lett.* **70**, 2020 (1993).
45. W. Wernsdorfer, Ph.D. thesis, Joseph Fourier University, Grenoble, 1996.
46. V. Bouchiat, M. Faucher, C. Thirion, W. Wernsdorfer, T. Fournier, and B. Pannetier, *Appl. Phys. Lett.* **78**, 0 (2001).
47. W. Wernsdorfer and R. Sessoli, *Science* **284**, 133 (1999).
48. S. Mangin, G. Marchal, W. Wernsdorfer, A. Sulpice, K. Hasselbach, D. Mailly, and B. Barbara, *Eur. Phys. Lett.* **39**, 675 (1997).
49. O. Fruchart, J.-P. Nozieres, W. Wernsdorfer, and D. Givord, *Phys. Rev. Lett.* **82**, 1305 (1999).
50. K. Hasselbach, C. Veauvy, and D. Mailly, *Physica C* **332**, 140 (2000).
51. G. Cernicchiaro, K. Hasselbach, D. Mailly, W. Wernsdorfer, and A. Benoit, in *Quantum Transport in Semiconductor Submicron Structures*, Vol. 326 of *NATO ASI Series E: Applied Sciences*, edited by Bernard Kramer, ed., Kluwer Academic Publishers, London, 1996.

52. E. C. Stoner and E. P. Wohlfarth, *Philos. Trans. London Ser. A* **240**, 599 (1948), reprinted in *IEEE Trans. Magn.* **MAG-27**, 3475 (1991).
53. L. Néel, *C. R. Acad. Sci.* **224**, 1550 (1947).
54. A. Thiaville, *J. Magn. Magn. Mat.* **182**, 5 (1998).
55. A. Thiaville, *Phys. Rev. B* **61**, 12221 (2000).
56. R. H. Victora, *Phys. Rev. Lett.* **63**, 457 (1989).
57. H. Pfeiffer, *Phys. Status Solidi* **118**, 295 (1990).
58. H. Pfeiffer, *Phys. Status Solidi* **122**, 377 (1990).
59. W. Wernsdorfer, K. Hasselbach, A. Benoit, G. Cernicchiaro, D. Mailly, B. Barbara, and L. Thomas, *J. Magn. Magn. Mater.* **151**, 38 (1995).
60. A. Perez, P. Melinon, V. Depuis, P. Jensen, B. Prevel, J. Tuaillon, L. Bardotti, C. Martet, M. Treilleux, M. Pellarin, J. L. Vaille, B. Palpant, and J. Lerme, *J. Phys. D* **30**, 709 (1997).
61. M. Jamet, V. Dupuis, P. Mélinon, G. Guiraud, A. Pérez, W. Wernsdorfer, A. Traverse, and B. Baguenard, *Phys. Rev. B* **62**, 493 (2000).
62. C. H. Lee, Hui He, F. J. Lamelas, W. Vavrn, C. Uher, and Roy Clarke, *Phys. Rev. B* **42**, 1066 (1990).
63. D. S. Chuang, C. A. Ballentine, and R. C. O'Handley, *Phys. Rev. B* **49**, 15084 (1994).
64. Ching-Ray Chang, *J. Appl. Phys.* **69**, 2431 (1991).
65. E. Bonet, W. Wernsdorfer, B. Barbara, K. Hasselbach, A. Benoit, and D. Mailly, *IEEE Trans. Mag.* **34**, 979 (1998).
66. H. Frei, S. Shtrikman, and D. Treves, *Phys. Rev.* **106**, 446 (1957).
67. A. Aharoni, *J. Appl. Phys.* **86**, 1042 (1999).
68. A. Aharoni, *J. Appl. Phys.* **82**, 1281 (1997).
69. A. Aharoni, *IEEE Trans. Magn.* **22**, 478 (1986).
70. A. Aharoni, *Phys. Status Solidi* **16**, 3 (1966).
71. Y. Ishii, *J. Appl. Phys.* **70**, 3765 (1991).
72. A. Aharoni, *J. Appl. Phys.* **87**, 5526 (2000).
73. R. Ferré, K. Ounadjela, J. M. George, L. Piraux, and S. Dubois, *Phys. Rev. B* **56**, 14066 (1997).
74. W. Wernsdorfer, K. Hasselbach, A. Benoit, B. Barbara, B. Doudin, J. Meier, J.-Ph. Ansermet, and D. Mailly, *Phys. Rev. B* **55**, 1155 (1997).
75. B. Doudin and J.-Ph. Ansermet, *Nanostructured Mater.* **6**, 521 (1995).
76. J. Meier, B. Doudin, and J.-Ph. Ansermet, *J. Appl. Phys.* **79**, 6010 (1996).
77. Hans-Benjamin Braun, *J. Appl. Phys.* **85**, 6172 (1999).
78. M. Ledermann, R. O'Barr, and S. Schultz, *IEEE Trans. Mag.* **31**, 3793 (1995).
79. W. Wernsdorfer, K. Hasselbach, A. Sulpice, A. Benoit, J.-E. Wegrowe, L. Thomas, B. Barbara, and D. Mailly, *Phys. Rev. B* **53**, 3341 (1996).
80. H. A. M. van den Berg, *J. Appl. Phys.* **61**, 4194 (1987).
81. P. Bryant and H. Suhl, *Appl. Phys. Lett.* **54**, 78 (1989).
82. M. Rührig, W. Bartsch, M. Vieth, and A. Hubert, *IEEE Trans. Mag.* **MAG-26**, 2807 (1990).
83. A. Fernandez, M. R. Gibbons, M. A. Wall, and C. J. Cerjan, *J. Magn. Magn. Mater.* **190**, 71 (1998).
84. C. P. Bean, *J. Appl. Phys.* **26**, 1381 (1955).

85. C. P. Bean and J. D. Livingstone, *J. Appl. Phys.* **30**, 120S (1959).
86. W. F. Brown, *J. Appl. Phys.* **30**, 130S (1959).
87. W. F. Brown, *J. Appl. Phys.* **34**, 1319 (1963).
88. W. F. Brown, *Phys. Rev.* **130**, 1677 (1963).
89. W. T. Coffey, D. S. F. Crothers, J. L. Dormann, Yu. P. Kalmykov, and J. T. Waldron, *Phys. Rev. B* **52**, 15951 (1995).
90. W. T. Coffey, D. S. F. Crothers, J. L. Dormann, Yu. P. Kalmykov, E. C. Kennedy, and W. Wernsdorfer, *Phys. Rev. Lett.* **80**, 5655 (1998).
91. W. T. Coffey, D. S. F. Crothers, J. L. Dormann, Yu. P. Kalmykov, E. C. Kennedy, and W. Wernsdorfer, *J. Phys. Cond. Mater.* **10**, 9093 (1998).
92. I. Klik and L. Gunther, *J. Stat. Phys.* **60**, 473 (1990).
93. I. Klik and L. Gunther, *J. Appl. Phys.* **67**, 4505 (1990).
94. W. T. Coffey, *Adv. Chem. Phys.* **103**, 259 (1998).
95. A. Garg, *Phys. Rev. B* **51**, 15592 (1995).
96. J. Kurkijärvi, *Phys. Rev. B* **6**, 832 (1972).
97. H. L. Richards, S. W. Sides, M. A. Novotny, and P. A. Rikvold, *J. Appl. Phys.* **79**, 5749 (1996).
98. J. M. Gonzalez, R. Ramirez, R. Smirnov-Rueda, and J. Gonzalez, *J. Appl. Phys.* **79**, 6479 (1996).
99. D. Garcia-Pablos, P. Garcia-Mochales, and N. Garcia, *J. Appl. Phys.* **79**, 6021 (1996).
100. D. Hinzke and U. Nowak, *Phys. Rev. B* **58**, 265 (1998).
101. E. D. Boerner and H. Neal Bertram, *IEEE Trans. Mag.* **33**, 3052 (1997).
102. M. Respaud, J. M. Broto, H. Rakoto, A. R. Fert, L. Thomas, and B. Barbara, *Phys. Rev. B* **57**, 2925 (1998).
103. A. E. Berkowitz, J. A. Lahut, I. S. Jacobs, L. M. Levinson, and D. W. Forester, *Phys. Rev. Lett.* **34**, 594 (1975).
104. J. T. Richardson, D. I. Yiagas, B. Turk, J. Forster, and M. V. Twigg, *J. Appl. Phys.* **70**, 6977 (1991).
105. R. H. Kodama, A. E. Berkowitz, E. J. McNiff, Jr., and S. Foner, *Phys. Rev. Lett.* **77**, 394 (1996).
106. R. H. Kodama, *J. Magn. Magn. Mater.* **200**, 359 (1999).
107. A. J. Leggett, S. Chakravarty, A. T. Dorsey, M. P. A. Fisher, A. Garg, and W. Zwerger, *Rev. Mod. Phys.* **59**, 1 (1987).
108. *Quantum Tunneling of Magnetization-QTM'94*, Vol. 301 of *NATO ASI Series E: Applied Sciences*, by L. Gunther and B. Barbara, eds., Kluwer Academic Publishers, London, 1995.
109. Y. Pontillon, A. Caneschi, D. Gatteschi, R. Sessoli, E. Ressouche, J. Schweizer, and E. Lelievte-Berna, *J. Am. Chem. Soc.* **121**, 5342 (1999).
110. A. L. Barra, D. Gatteschi, and R. Sessoli, *Chem. Eur. J.* **6**, 1608 (2000).
111. R. Sessoli, D. Gatteschi, A. Caneschi, and M. A. Novak, *Nature* **365**, 141 (1993).
112. A.-L. Barra, P. Debrunner, D. Gatteschi, Ch. E. Schulz, and R. Sessoli, *Euro. Phys. Lett.* **35**, 133 (1996).
113. M. A. Novak and R. Sessoli, in *Quantum Tunneling of Magnetization-QTM'94*, Vol. 301 of *NATO ASI Series E: Applied Sciences*, L. Gunther and B. Barbara, eds., Kluwer Academic Publishers, London, 1995, pp. 171–188.
114. J. R. Friedman, M. P. Sarachik, J. Tejada, and R. Ziolo, *Phys. Rev. Lett.* **76**, 3830 (1996).

115. L. Thomas, F. Lionti, R. Ballou, D. Gatteschi, R. Sessoli, and B. Barbara, *Nature (London)* **383**, 145 (1996).

116. C. Sangregorio, T. Ohm, C. Paulsen, R. Sessoli, and D. Gatteschi, *Phys. Rev. Lett.* **78**, 4645 (1997).

117. A. Garg, *Phys. Rev. B* **81**, 1513 (1998).

118. T. Ohm, C. Sangregorio, and C. Paulsen, *Eur. Phys. J. B* **6**, 195 (1998).

119. J. A. A. J. Perenboom, J. S. Brooks, S. Hill, T. Hathaway, and N. S. Dalal, *Phys. Rev. B* **58**, 330 (1998).

120. A. D. Kent, Y. Zhong, L. Bokacheva, D. Ruiz, D. N. Hendrickson, and M. P. Sarachik, *Eur. Phys. Lett.* **49**, 521 (2000).

121. A. Caneschi, D. Gatteschi, C. Sangregorio, R. Sessoli, L. Sorace, A. Cornia, M. A. Novak, C. Paulsen, and W. Wernsdorfer, *J. Magn. Magn. Mater.* **200**, 182 (1999).

122. S. M. J. Aubin, N. R. Dilley, M. B. Wemple, G. Christou, and D. N. Hendrickson, *J. Am. Chem. Soc.* **120**, 839 (1998).

123. D. J. Price, F. Lionti, R. Ballou, P. T. Wood, and A. K. Powell, *Phil. Trans. R. Soc. Lond. A* **357**, 3099 (1999).

124. J. Yoo, E. K. Brechin, A. Yamaguchi, M. Nakano, J. C. Huffman, A. L. Maniero, L.-C. Brunel, K. Awaga, H. Ishimoto, G. Christou, and D. N. Hendrickson, *Inorg. Chem.* **39**, 3615 (2000).

125. K. Wieghardt, K. Pohl, I. Jibril, and G. Huttner, *Angew. Chem. Int. Ed. Engl.* **23**, 77 (1984).

126. W. Wernsdorfer, I. Chiorescu, R. Sessoli, D. Gatteschi, and D. Mailly, *Phys. B* **284–288**, 1231 (2000).

127. C. Delfs, D. Gatteschi, L. Pardi, R. Sessoli, K. Wieghardt, and D. Hanke, *Inorg. Chem.* **32**, 3099 (1993).

128. A. Garg, *Eur. Phys. Lett.* **22**, 205 (1993).

129. W. Wernsdorfer, T. Ohm, C. Sangregorio, R. Roberta, D. Mailly, and C. Paulsen, *Phys. Rev. Lett.* **82**, 3903 (1999).

130. L. Landau, *Phys. Z. Sowjetunion* **2**, 46 (1932).

131. C. Zener, *Proc. R. Soc. London, Ser. A* **137**, 696 (1932).

132. E. C. G. Stückelberg, *Helv. Phys. Acta* **5**, 369 (1932).

133. S. Miyashita, *J. Phys. Soc. Jpn.* **64**, 3207 (1995).

134. S. Miyashita, *J. Phys. Soc. Jpn.* **65**, 2734 (1996).

135. G. Rose and P. C. E. Stamp, *Low Temp. Phys.* **113**, 1153 (1998).

136. G. Rose, Ph.D. thesis, The University of British Columbia, Vancouver, 1999.

137. M. Thorwart, M. Grifoni, and P. Hänggi, *Phys. Rev. Lett.* **85**, 860 (2000).

138. M. N. Leuenberger and D. Loss, *Phys. Rev. B* **61**, 12200 (2000).

139. J. Villain, A. Wurger, A. Fort, and A. Rettori, *J. Phys. I* **7**, 1583 (1997).

140. A. Fort, A. Rettori, J. Villain, D. Gatteschi, and R. Sessoli, *Phys. Rev. Lett.* **80**, 612 (1998).

141. M. N. Leuenberger and D. Loss, *Phys. Rev. B* **61**, 1286 (2000).

142. I. Tupitsyn, N. V. Prokof'ev, and P. C. E. Stamp, *Int. J. Mod. Phys. B* **11**, 2901 (1997).

143. N. V. Prokof'ev and P. C. E. Stamp, *Phys. Rev. Lett.* **80**, 5794 (1998).

144. W. Wernsdorfer, A. Caneschi, R. Sessoli, D. Gatteschi, A. Cornia, V. Villar, and C. Paulsen, *Phys. Rev. Lett.* **84**, 2965 (2000).

145. D. Loss, D. P. DiVincenzo, and G. Grinstein, *Phys. Rev. Lett.* **69**, 3232 (1992).

146. J. von Delft and C. L. Hendey, *Phys. Rev. Lett.* **69**, 3236 (1992).
147. R. P. Feynman, R. B. Leighton, and M. Sand, *The Feynman Lectures on Physics*, Vol. 3, Addison-Wesley, London, 1970.
148. A. Garg, *Phys. Rev. Lett.* **83**, 4385 (1999).
149. J. Villain and A. Fort, *Eur. Phys. J. B* **17**, 69 (2000).
150. E. Kececioglu and A. Garg, *Phys. Rev. B* **63**, 064422 (2001).
151. S. E. Barnes, cond-mat/9907257.
152. J.-Q. Liang, H. J. W. Mueller-Kirsten, D. K. Park, and F.-C. Pu, *Phys. Rev. B* **61**, 8856 (2000).
153. S. Yoo and S. Lee, *Phys. Rev. B* **62**, 5713 (2000).
154. R. Lü, H. Hu, J. Zhu, X. Wang, L. Chang, and B. Gu, *Phys. Rev. B* **61**, 14581 (2000).
155. R. Caciuffo, G. Amoretti, A. Murani, R. Sessoli, A. Caneschi, and D. Gatteschi, *Phys. Rev. Lett.* **81**, 4744 (1998).
156. G. Amoretti, R. Caciuffo, J. Combet, A. Murani, and A. Caneschi, *Phys. Rev. B* **62**, 3022 (2000).
157. M. Al-Saqer, V. V. Dobrovitski, B. N. Harmon, and M. I. Katsnelson, *J. Appl. Phys.* **87**, 6268 (2000).
158. R. P. Feynman and F. L. Vernon, *Ann. Phys.* **24**, 118 (1963).
159. N. V. Prokof'ev and P. C. E. Stamp, *J. Low Temp. Phys.* **104**, 143 (1996).
160. N. V. Prokof'ev and P. C. E. Stamp, *Rep. Prog. Phys.* **63**, 669 (2000).
161. T. Ohm, C. Sangregorio, and C. Paulsen, *J. Low Temp. Phys.* **113**, 1141 (1998).
162. T. Ohm, Ph.D. thesis, Joseph Fourier University, Grenoble, 1998.
163. A. Cuccoli, A. Fort, A. Rettori, E. Adam, and J. Villain, *Eur. Phys. J. B* **12**, 39 (1999).
164. W. Wernsdorfer, R. Sessoli, and D. Gatteschi, *Eur. Phys. Lett.* **47**, 254 (1999).
165. A. Abragam and B. Bleaney, *Electron Paramagnetic Resonance of Transition Ions*, Clarendon Press, Oxford, 1970.
166. W. Wernsdorfer, A. Caneschi, R. Sessoli, D. Gatteschi, A. Cornia, V. Villar, and C. Paulsen, *Eur. Phys. Lett.* **50**, 552 (2000).
167. L. Bokacheva, A. D. Kent, and M. A. Walters, *Phys. Rev. Lett.* **85**, 4803 (2000).
168. D. A. Garanin and E. M. Chudnovsky, *Phys. Rev. B* **59**, 3671 (1999).
169. I. Chiorescu, W. Wernsdorfer, B. Barbara, A. Müller, and H. Bögge, *J. Appl. Phys.* **87**, 5496 (2000).
170. W. Wernsdorfer, A. Caneschi, R. Sessoli, D. Gatteschi, A. Cornia, V. Villar, and C. Paulsen, *Phys. Rev. Lett.* **84**, 3454 (2000).
171. V. V. Dobrovitski, M. I. Katsnelson, and B. N. Harmon, *Phys. Rev. Lett.* **84**, 3458 (2000).
172. N. V. Prokof'ev and P. C. E. Stamp, in *Quantum Tunneling of Magnetization—QTM'94*, Vol. 301 of *NATO ASI Series E: Applied Sciences*, L. Gunther and B. Barbara, eds., (Kluwer Academic Publishers, London, 1995), p. 369.
173. E. Del Barco, J. M. Hernandez, J. Tejada, N. Biskup, R. Achey, I. Rutel, N. Dalal, and J. Brooks, *Phys. Rev. B* **62**, 3018 (2000).
174. M. N. Leuenberger and D. Loss, cond-mat/0011415.
175. O. B. Zaslavskii, *Phys. Rev. B* **42**, 992 (1990).
176. M. C. Miguel and E. M. Chudnovsky, *Phys. Rev. B* **54**, 388 (1996).
177. Gwang-Hee Kim and Dae Sung Hwang, *Phys. Rev. B* **55**, 8918 (1997).